

1N-02
167889
p-162

NASA Contractor Report 4513

The Ground Vortex Flow Field
Associated With a Jet in a Cross
Flow Impinging on a Ground
Plane for Uniform and Annular
Turbulent Axisymmetric Jets

William M. Cavage and John M. Kuhlman

GRANT NAG1-1245
MAY 1993

(NASA-CR-4513) THE GROUND VORTEX
FLOW FIELD ASSOCIATED WITH A JET IN
A CROSS FLOW IMPINGING ON A GROUND
PLANE FOR UNIFORM AND ANNULAR
TURBULENT AXISYMMETRIC JETS M.S.
Thesis (West Virginia Univ.)
162 p

N93-28449

Unclas

H1/02 0167889





NASA Contractor Report 4513

The Ground Vortex Flow Field
Associated With a Jet in a Cross
Flow Impinging on a Ground
Plane for Uniform and Annular
Turbulent Axisymmetric Jets

William M. Cavage and John M. Kuhlman
West Virginia University
Morgantown, West Virginia

Prepared for
Langley Research Center
under Grant NAG1-1245

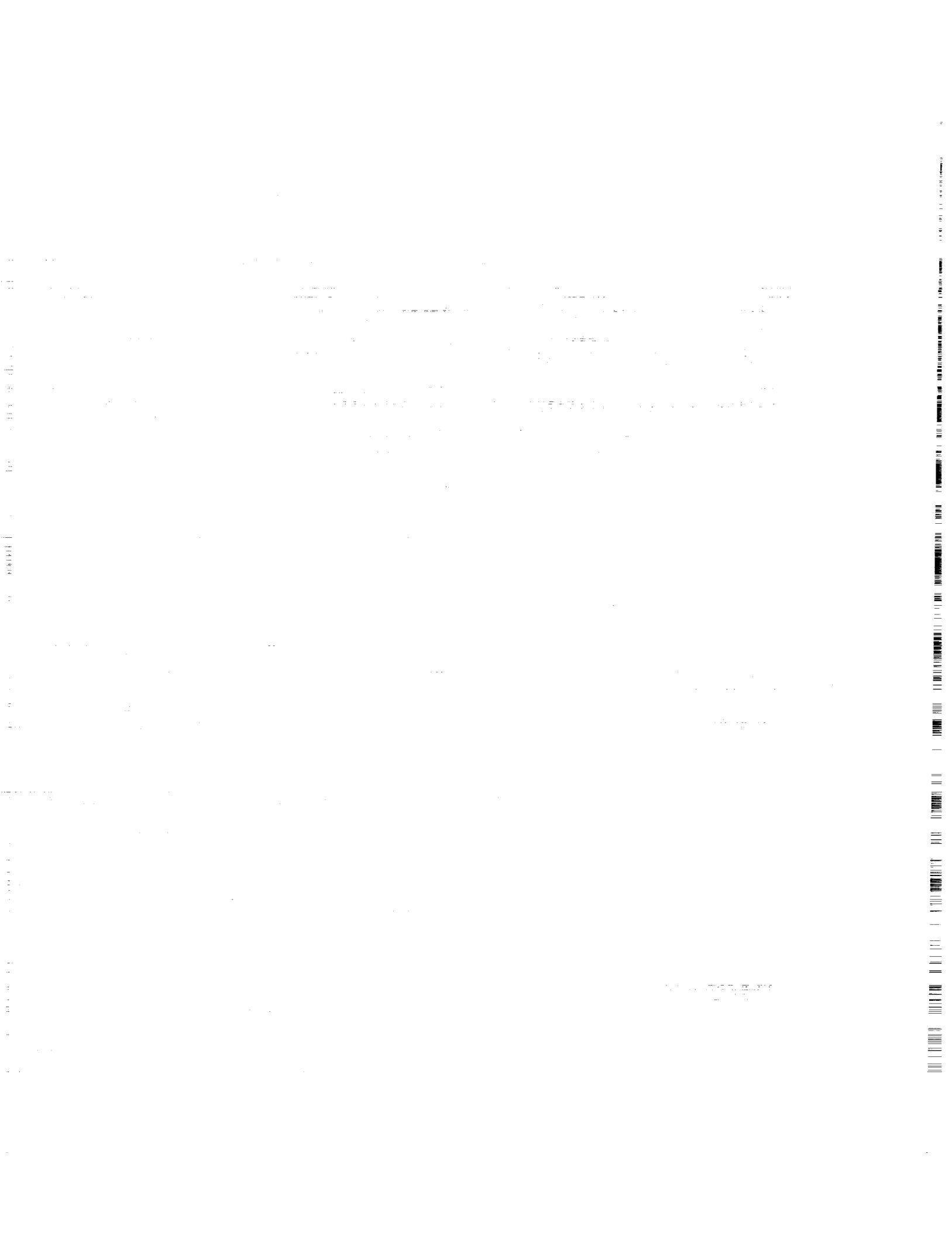


National Aeronautics and
Space Administration

Office of Management

Scientific and Technical
Information Program

1993

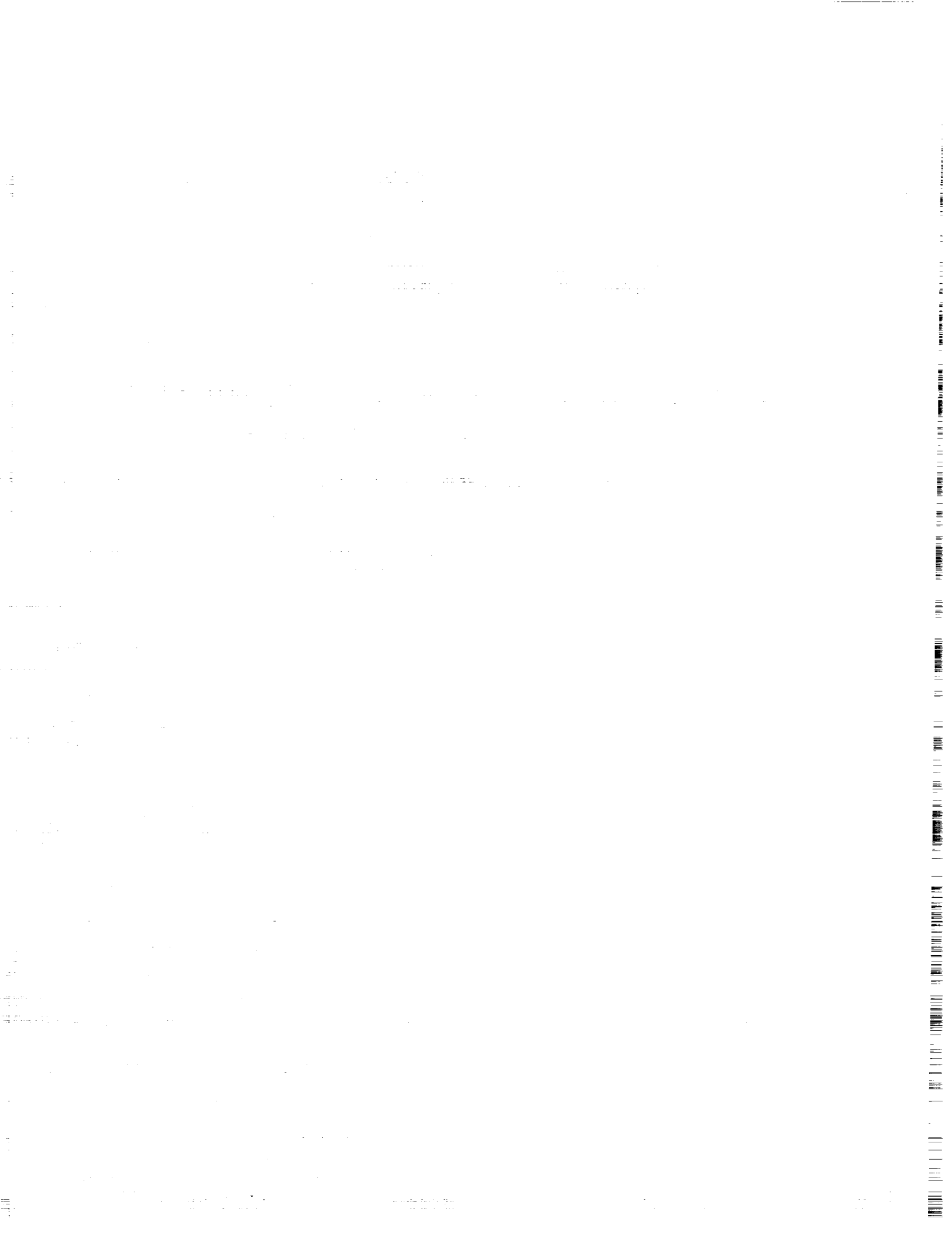


**The Ground Vortex Flow Field Associated with a Jet
in a Cross Flow Impinging On A Ground Plane for Uniform
and Annular Turbulent Axisymmetric Jets**

The following final report has been prepared under the sponsorship of the NASA Langley Research Center under Grant NAG-1-1245, Mr. Guy T. Kemmerly and Mr. John W. Paulson, Jr., technical monitors. This report essentially consists of the Master's thesis prepared by the first author, under the direction of the second author.

PRECEDING PAGE BLANK NOT FILMED

~~FOR INTENTIONALLY BLANK~~



ABSTRACT

An experimental study has been conducted of the impingement of a single circular jet on a ground plane in a cross flow. This geometry is a simplified model of the interaction of propulsive jet exhaust from a V/STOL aircraft with the ground in forward flight. Jets have been oriented normal to the cross flow and ground plane. Jet size, cross flow-to-jet velocity ratio, ground plane-to-jet board spacing, and jet exit turbulence level and mean velocity profile shape have all been varied to determine their effects on the size of the ground vortex interaction region which forms on the ground plane, using smoke injection into the jet. Three component laser Doppler velocimeter measurements were made with a commercial three color system for the case of a uniform jet with exit spacing equal to 5.5 diameters and cross flow-to-jet velocity ratio equal to 0.11.

The flow visualization data compared well for equivalent runs of the same nondimensional jet exit spacing and the same velocity ratio for different diameter nozzles, except at very low velocity ratios and for the larger nozzle, where tunnel blockage became significant. Variation of observed ground vortex size with cross flow-to-jet velocity ratio was consistent with previous studies. Observed effects of jet size and ground plane-to-jet board spacing were relatively small. Jet exit turbulence level effects were also small. However, an annular jet with a low velocity central core was found to have a significantly smaller ground vortex than an equivalent uniform jet at the same values of cross flow-to-jet velocity ratio and jet exit-to-ground plane spacing. This may suggest a means of altering ground vortex behavior somewhat, and points out the importance of proper simulation of jet exit velocity conditions. LV data indicated unsteady turbulence levels in the ground vortex in excess of 70 percent.

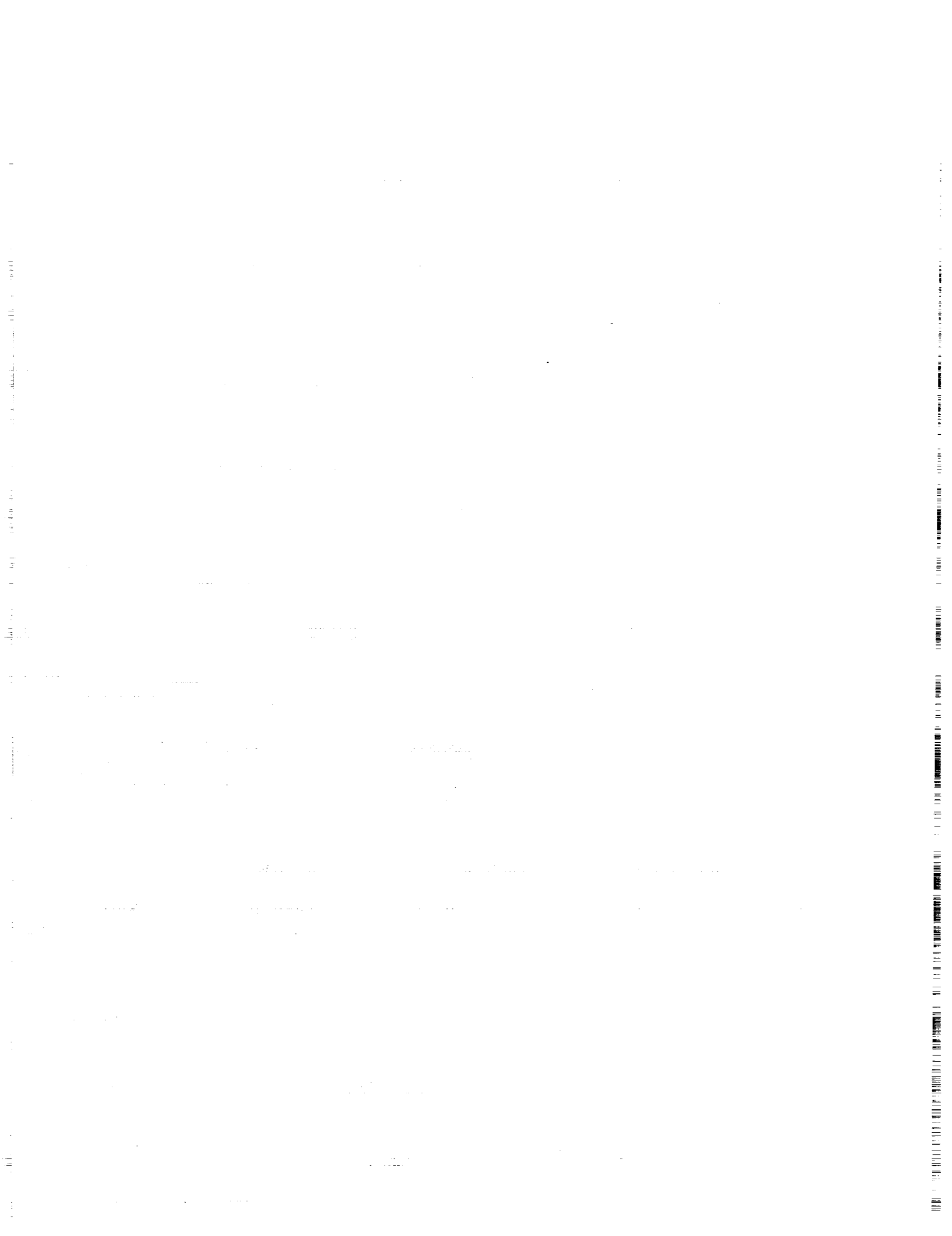


TABLE OF CONTENTS

Abstract	v
Table of Contents	vii
Nomenclature	ix
List of Figures	xiii
List of Tables	xvii
Chapter 1: Introduction	
Background	1
Motivation for Study	3
Statement of Research	4
Chapter 2: Literature Review	
Turbulent Jets	8
Annular Jets	9
Impinging Jets	10
Ground Vortex Formation	11
Laser Doppler Velocimetry	12
Chapter 3: Apparatus and Procedure	
Apparatus	15
Procedure	18
Chapter 4: Theoretical Background	
Description of Jet Behavior	27
Effective Diameter Calculation	29
Nozzle Calibration Data Reduction Program	31

2002 Ji INTENTIONALLY BLANK

Analysis of Ground Vortex Formation	33
Chapter 5: Results	
Nozzle Calibration	42
Flow Visualization of Ground Vortex	43
LV Measurements	52
Chapter 6: Conclusions and Recommendations	
Conclusions	97
Recommendations	98
References	100
Appendices	
A: Calculation of Critical Distances for Nozzle Geometries	103
B: LV Theory and Methods	108
C: Derivation of Effective Diameter and Velocity	111
D: Listing of Program to Calculate Jet Nozzle Characteristics	114
E: LV Data Plotted in Linear Coordinates	130

NOMENCLATURE

A	jet exit area
A_{eff}	effective area of jet exit
b	jet width
D	jet nozzle diameter; beam spacing
D_{eff}	effective diameter of jet exit
d_b	beam diameter
d_f	diameter of the focused beam
d_x	length of major axis of probe volume
d_y	length of minor axis of probe volume
E	beam expansion factor
f_d	Doppler frequency
f_0	middle function value for modified Simpson's rule with varying Δx
f_1	first function value for modified Simpson's rule with varying Δx
f_2	last function value for modified Simpson's rule with varying Δx
g	gravitational acceleration constant
h	distance from jet exit to ground plane
l_1	distance from plenum entrance to end of first arc
l_2	distance from jet exit to end of first arc
m	mass flow rate of jet
M	Mach number

MF	momentum flux of jet nozzle
N_f	number of fringes
P_{atm}	atmospheric pressure
P_e	exit static pressure
P_i	maximum ground plane impingment pressure
P_o	total pressure
P_{noz}	static pressure in jet plenum
Q	volumetric flow rate of jet nozzle at exit
q	dynamic pressure; source strength
q_{max}	maximum jet exit dynamic pressure
R	gas constant; jet radius
Re	Reynolds number
R_1	radius of large arc forming the plenum
R_2	radius of small arc completing the jet flow contraction
r	radial coordinate
S_1	first Δx step in modified Simpson's rule
S_2	second Δx step in modified Simpson's rule
T_{atm}	atmospheric temperature
T_o	total temperature
T_λ	Taylor microscale
t_1	distance from begining of jet nozzle to end of first arc
t_2	distance from nozzle centerline to end of first arc

U	jet exit velocity
u	x component of velocity vector
v	y component of velocity vector
V_{eff}	effective jet exit velocity
V_j	average jet exit velocity
V_{max}	maximum jet exit velocity
V_{∞}	cross flow velocity
w	z component of velocity vector
x	coordinate direction along cross flow direction
X_{cv}	ground vortex centerline upstream penetration of vortex center
X_i	ground vortex impingement point location
X_{Pmax}	ground vortex centerline upstream penetration (maximum)
X_{Smax}	ground vortex centerline upstream separation distance (maximum)
y	spanwise coordinate direction
z	coordinate direction along jet flow direction
Z_b	distance from jet board to ground plane
β_1	angle of large radial arc (R_1) that forms the plenum
β_2	angle of small radial arc (R_2) that completes jet flow contraction
γ	ratio of specific heats
λ	wave length of coherent laser light
λ^*	square root of dynamic pressure ratio
ν	kinematic viscosity

ρ density of jet exit air

θ beam half angle

LIST OF FIGURES

- Figure 1.1: Schematic of ground vortex illustrating both a.) top view and b.) centerline side view.
- Figure 1.2: Schematic of flow field around F-15 SMTD with thrust reversers activated illustrating ground vortex formation. (from Blake and Laughrey, 1987)
- Figure 3.1: Top view of jet-ground interaction facility.
- Figure 3.2: Jet-ground interaction facility jet board.
- Figure 3.3: Cross Section of plenum and three different size jet nozzles.
- Figure 3.4: Cross section of special annular nozzle.
- Figure 3.5: Top view of LV system positioned with jet-ground interaction facility.
- Figure 4.1: Illustration of virtual origin for a.) poor and b.) good near field mixing
- Figure 4.2: Illustration of equation (10) defining the significant dimensions for modified Simpson's Rule
- Figure 4.3: Example of a measured velocity profile with the velocity profile altered by the program for integration.
- Figure 4.4: Illustration of integrand for volume flow rate.
- Figure 4.5: Illustration of the integrand for momentum flux.
- Figure 5.1: Axial velocity profiles obtained by horizontal and vertical traverse for the 1.27 cm diameter nozzle; 2 diameter nozzle length.
- Figure 5.2: Axial velocity profiles obtained by horizontal and vertical traverse for the 2.54 cm diameter nozzle; 2 diameter nozzle length.
- Figure 5.3: Axial velocity profiles obtained by horizontal and vertical traverse for the 0.95 cm diameter nozzle; 2 diameter nozzle length.
- Figure 5.4: Axial velocity profiles obtained by horizontal and vertical traverse for the turbulence generating nozzle; 1.27 cm diameter exit.

- Figure 5.5: Axial velocity profiles obtained by horizontal and vertical traverse for the annular nozzle; 1.27 cm diameter exit.
- Figure 5.6: Axial velocity profiles obtained by horizontal and vertical traverse for the 1.27 cm diameter nozzle; 4 diameter nozzle length.
- Figure 5.7: Axial velocity profiles obtained by horizontal traverse for the 1.27 cm diameter nozzle; 13 diameter nozzle length.
- Figure 5.8: Axial velocity profiles obtained by horizontal and vertical traverse for the 0.91 cm diameter nozzle; 7 diameter nozzle length.
- Figure 5.9: Comparison of nondimensional shape of ground vortex for different jet board spacing for h/D equal to 4.34 and V_∞/V_j equal to .11.
- Figure 5.10: Comparison of nondimensional shape of ground vortex for the three different nozzle diameters at h/D equal to 7 and V_∞/V_j equal to .14.
- Figure 5.11: Comparison of nondimensional shape of ground vortex for 1.27 and 0.91 cm nozzles for h/D equal to 3 and V_∞/V_j equal to .1.
- Figure 5.12: Comparison of nondimensional shape of ground vortex for 2.54, 1.27, and 0.91 cm nozzles for h/D equal to 3 and V_∞/V_j equal to .125.
- Figure 5.13: Comparison of nondimensional shape of ground vortex for 2.54, 1.27, and 0.91 cm nozzles for h/D equal to 3 and V_∞/V_j equal to .15.
- Figure 5.14: Comparison of nondimensional shape of ground vortex for 2.54, 1.27, and 0.91 cm nozzles for h/D equal to 3 and V_∞/V_j equal to .18.
- Figure 5.15: Comparison of nondimensional shape of ground vortex for different velocity ratios using the 0.91 cm nozzle; $h/D = 3$; $Z_b/D = 10$.
- Figure 5.16: Comparison of nondimensional shape of ground vortex for different velocity ratios using the 1.27 cm nozzle; $h/D = 3$; $Z_b/D = 7$.
- Figure 5.17: Comparison of nondimensional shape of ground vortex for different velocity ratios using the 2.54 cm nozzle; $h/D = 3$; $Z_b/D = 5$.
- Figure 5.18: Comparison of nondimensional maximum penetration of the ground vortex along centerline for two different data sets taken.
- Figure 5.19: Nondimensional ground vortex separation distance versus V_∞/V_j along the centerline (maximum).

- Figure 5.20: Comparison of previous work of the nondimensional ground vortex separation distance versus λ^* along the centerline (maximum).
- Figure 5.21: Comparison of different velocity ratio data nondimensionalized with X_{pmax} compared with equation 4.13 for the 0.91 cm jet nozzle.
- Figure 5.22: Comparison of different velocity ratio data nondimensionalized with X_{pmax} compared with equation 4.13 for the 1.27 cm jet nozzle.
- Figure 5.23: Comparison of different velocity ratio data nondimensionalized with X_{pmax} compared with equation 4.13 for the 2.54 cm jet nozzle.
- Figure 5.24: Log - Log plot of data nondimensionalized with V_∞/V_j plotted with equation (4.16) for 0.91 cm nozzle; $h/D = 3$; $Z_b/D = 10$.
- Figure 5.25: Log - Log plot of data nondimensionalized with V_∞/V_j plotted with equation (4.16) for 1.27 cm nozzle; $h/D = 3$; $Z_b/D = 7$.
- Figure 5.26: Log - Log plot of data nondimensionalized with V_∞/V_j plotted with equation (4.16) for 2.54 cm nozzle; $h/D = 3$; $Z_b/D = 7$.
- Figure 5.27: Comparison of equation (4.13) with (4.16) which is represented by (4.22) on standard axes.
- Figure 5.28: Comparison of the nondimensional shape of ground vortex for the three different nozzle configurations; h/D_{eff} equal to 5.5 and V_∞/V_j equal to .11.
- Figure 5.29: Nondimensional comparison of the three different methods of calculating D_{eff} and V_{eff} compared with the standard nozzle; $h/D_{eff} = 6$, $V_\infty/V_j = .1$.
- Figure 5.30: Plot of repeated data for the 1.27 cm jet nozzle; $h/D = 3$, $V_\infty/V_j = 0.1$.
- Figure 5.31: Plot of repeated data for the 1.27 cm jet nozzle; $h/D = 3$, $V_\infty/V_j = 0.125$.
- Figure 5.32: Plot of repeated data for the 1.27 cm jet nozzle; $h/D = 3$, $V_\infty/V_j = 0.15$.
- Figure 5.33: Plot of repeated data for the 1.27 cm jet nozzle with jet exit spacing of 4.34 diameters; $V_\infty/V_j = .11$, $Z_b/D = 6.34$.
- Figure 5.34: Plot of repeated data for the 1.27 cm jet nozzle with jet exit spacing of 4.34 diameters; $V_\infty/V_j = .11$, $Z_b/D = 8.34$.
- Figure 5.35: Plot of repeated data for the 1.27 cm jet nozzle with jet exit spacing of 4.34 diameters; $V_\infty/V_j = .11$, $Z_b/D = 17.34$.

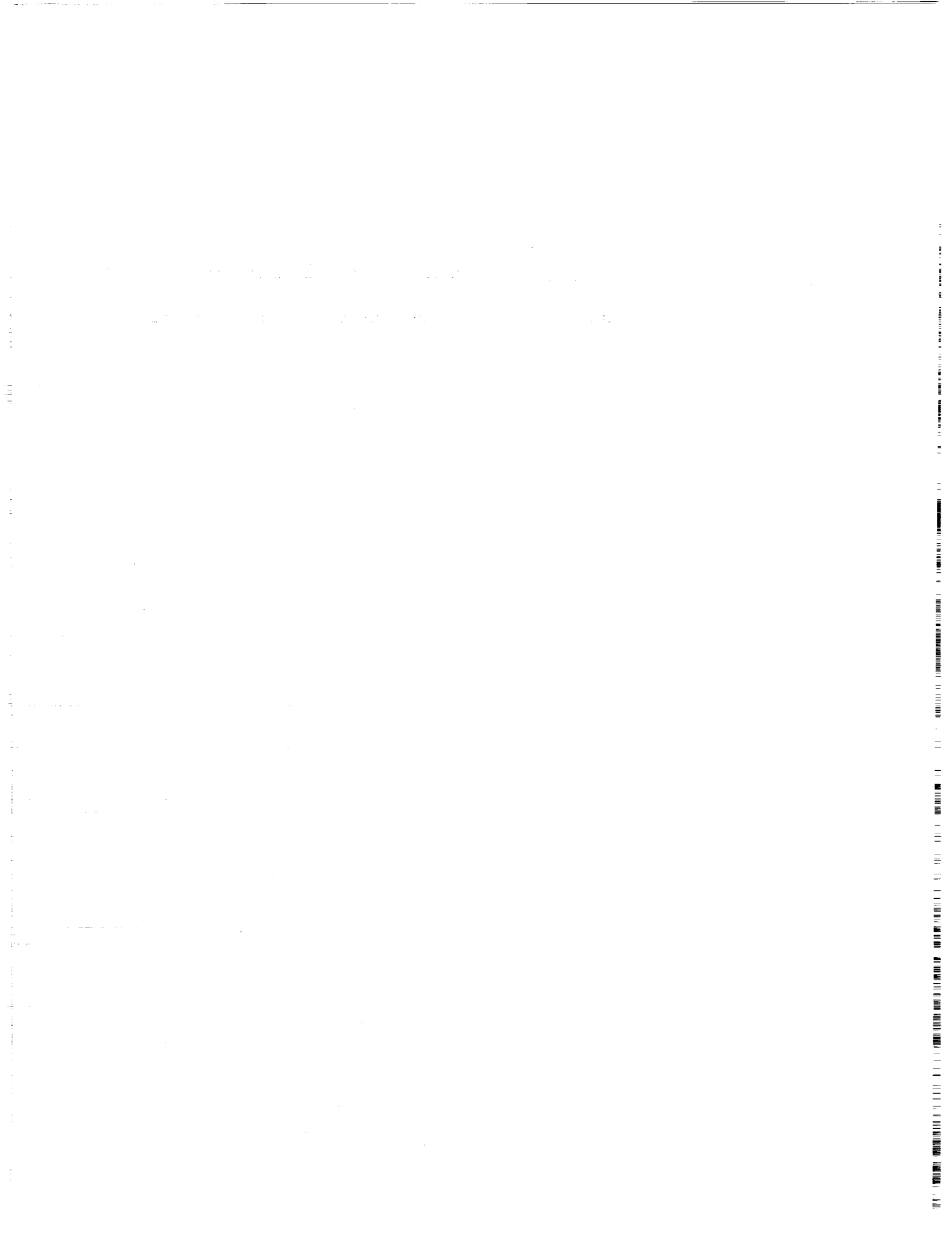
- Figure 5.36: Plot of repeated data for the 1.27 cm jet nozzle with jet exit spacing of 4.34 diameters; $V_\infty/V_j = .11$, $Z_b/D = 17.34$ (panel removed).
- Figure 5.37: Vector plot of the LV measurements on the centerline of the ground vortex ($y/D_{eff} = 0$) for the case of $h/D_{eff} = 5.5$ and $V_\infty/V_j = 0.11$. x/D_{eff} ranges from 16.00 to 3.20 in increments of 1.6.
- Figure 5.38: Vector plot of the LV measurements of the ground vortex leg at $x/D_{eff} = 8.00$ for the case of $h/D_{eff} = 5.5$ and $V_\infty/V_j = 0.11$. y/D_{eff} ranges from 0.0 to 16.00 in increments of 1.6.
- Figure 5.39: Interpolated vector plot of the LV measurements of the ground vortex leg at $x/D_{eff} = 8.00$ for the case of $h/D_{eff} = 5.5$ and $V_\infty/V_j = 0.11$. y/D_{eff} ranges from 0.0 to 16.00 in increments of 1.6.
- Figure 5.40: Interpolated vector plot of the LV measurements of the ground vortex leg at $x/D_{eff} = 8.00$ for the case of $h/D_{eff} = 5.5$ and $V_\infty/V_j = 0.11$. y/D_{eff} ranges from 0.0 to 16.00 in increments of 1.6.

LIST OF TABLES

Table 3.1: Specifications of DANTEC three color laser Doppler velocimeter.

Table 5.1: Table of calibration results for the eight nozzles utilized in the present study.

Table 5.2: Table of effective diameter and velocity calculated by three different methods.



CHAPTER 1: INTRODUCTION

1.1 Background

The flow field generated by a jet in a cross flow has many applications ranging from atmospheric flows and water sciences, such as the use of a smokestack or a waste water disposal pipe for pollutant dispersion, to the propulsive jet flows from a jet V/STOL aircraft configuration. A single circular jet impinging on a ground plane in the presence of a cross flow simulates a basic flow module for a V/STOL aircraft in close proximity to the ground (ie, in ground effect). Although most of the research performed in the area of a jet in a cross flow has focused on flow fields out of ground effect, some research has also been performed for jets in ground effect, particularly in the field of V/STOL aerodynamics. Historically, many inconsistencies have been observed in the measurements associated with the simulation of such flow fields. Also, the flow fields around various V/STOL configurations have been known to be highly configuration dependent (Stewart, 1988).

The problem of accurate simulation of such configurations has been studied in recent years. It has been experimentally determined that the flow field associated with a static wind tunnel test of a V/STOL aircraft configuration in ground effect does not have the same flow field as that same model when a dynamic moving model simulation is performed on it, and that the inaccuracy lies in the static measurements. Paulson and Kemmerly (1989) attribute this to different interactions with trailing wake vortices. It has been theorized that the static wind tunnel test is inaccurate because the boundary conditions are not properly matched, and because the propulsive jet and wake trajectories are time-dependent in the dynamic case.

Proper transformation would require that the oncoming flow be uniform at all locations, which cannot be true for the static model tests due to the no slip condition, which requires that the velocity at the ground (wind tunnel floor) must be zero. Efforts have been undertaken to match this boundary condition using a moving belt on the wind tunnel floor that moves at the velocity of the uniform flow. These moving ground belt tests allow for the matching of the boundary conditions for a static model test to be compared to a dynamic model test. Moving ground belt tests performed have ground vortex formation results 40 to 50 percent different than the experiments performed without the moving ground belt (Kuhn et. al., 1988). To date, even the ground vortex flow field associated with a static jet impinging on a ground plane without a moving ground belt has not been completely mapped to allow for a fair comparison with moving model tests.

The ground vortex flow field associated with an impinging jet in the presence of a cross flow has been studied frequently in the field of V/STOL aerodynamics. When an axisymmetric jet impinges on a surface, a radial wall jet forms which flows radially outward, while slowing due to continuity. When a cross flow is present, at some point the momentum of the cross flow will be of the same order as the momentum of the radial wall jet causing the flow to turn back on itself, resulting in separation and the formation of a parabolic ground vortex around the impinging jet. Figure 1.1 gives a schematic of this flow field, and also defines the critical dimensions associated with it and the coordinate system to be used for the present research. The critical parameters associated with the ground vortex are usually given in nondimensional form, with the most critical parameters being the jet nozzle-to-ground plane spacing, h/D , and the velocity ratio between the cross flow and the jet,

V_{∞}/V_j .

1.2 Motivation for Study

The ground vortex flow field can be compared with a horseshoe vortex flow field that occurs around a bridge pylon in a swift stream, except that a ground vortex forms around the impinging wall jet rather than a solid obstruction, and is a highly unsteady and intermittent flow field. It has been observed that the time averaged behavior of the ground vortex is not an accurate measure of the true behavior of the ground vortex. The intermittency of the ground vortex is most likely the large scale fluctuation between two distinct states, the average of which has little bearing on the time dependant flow field (Cimbala et. al., 1988). It has also been observed that the ground vortex tends to "explode" and unravel upstream into the cross flow, and subsequently to collapse on itself and disappear toward the jet nozzle. These two phenomena appear to occur with some periodicity and have been associated with the ability of the flow to "store" energy or have some energy "deficit" which causes the flow field to seek equilibrium in some violent fashion as these two phenomena alternate.

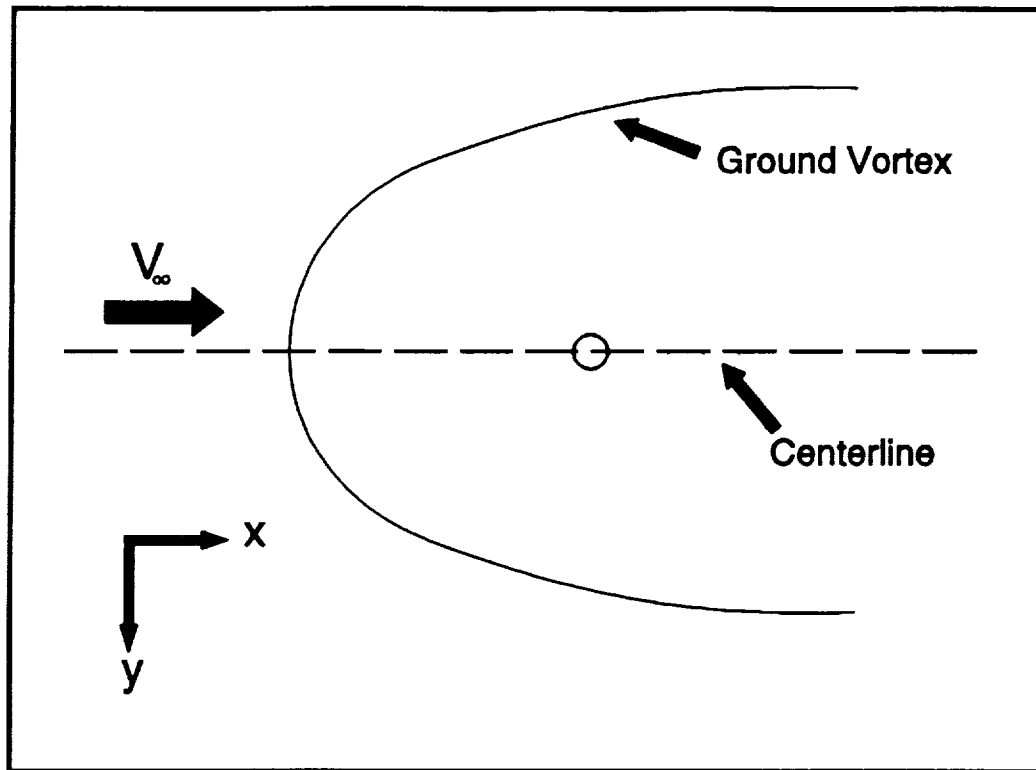
The ground vortex is a main contributor to one of the most serious problems associated with V/STOL propulsion; hot gas or debris ingestion due to the formation of the ground vortex in front of the engine inlet. This can lead to stall of the aircraft engine or thrust loss at the critical time of landing, perhaps even causing the aircraft to crash. Figure 1.2 illustrates a V/STOL aircraft (the F-15 SMTD) with thrust reversers activated during landing causing a ground vortex to form at the engine inlet. Ground vortex formation has

also been associated with jet induced lift loss in ground effect on an aircraft body. Several studies (eg. Spreemann and Sherman, 1958) have examined how a vortex trapped under an aircraft body due to the close proximity of the ground will cause what is known as "suck down", which is when a sudden loss of lift in ground effect causes a V/STOL aircraft to crash straight down during landing. These problems occurring in ground effect are a result of the near field turbulent jet behavior, which at one time was believed to be universal. However, Kuhlman (1987) illustrated that a non-uniform jet exit velocity profile, caused by an annular or swirl nozzle, alters near field jet behavior significantly. Methods have been developed to determine effective diameters and effective average jet velocities (Ziegler and Wooler, 1968) for these types of jet nozzles, to allow for a rational nondimensional comparison with other jet nozzles. It was speculated at the start of the present study that this might be a way to change the behavior of the ground vortex.

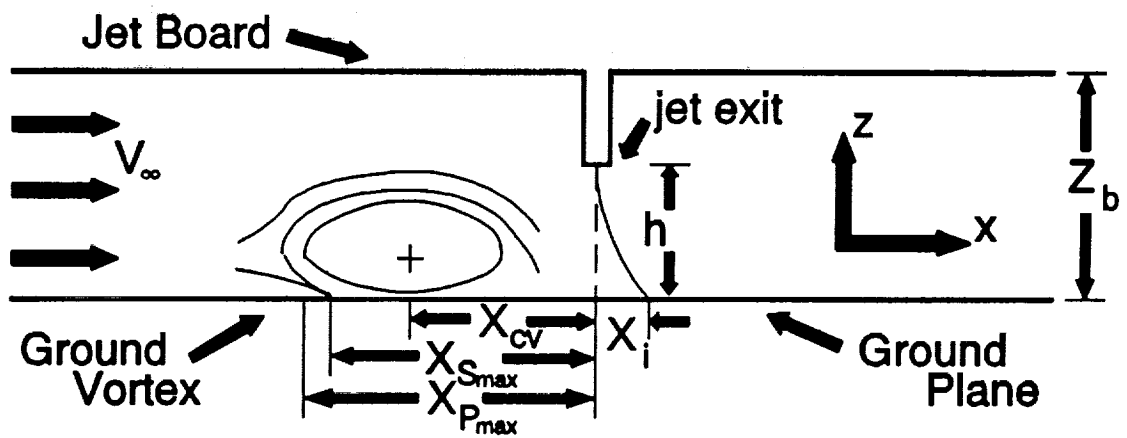
1.3 Statement of Research

A study of the ground vortex flow field associated with a single, turbulent jet issuing from a nozzle which protrudes from a flat plate into a 90 degree cross flow in close proximity to the ground has been performed. Flow visualization has been performed to determine the size and shape of the ground vortex flow field for different values of h/D and V_∞/V_j to determine what case was of most interest for further study using LV. Also investigated were such critical problems as nondimensional agreement of the ground vortex for different size nozzles, effects of tunnel blockage, the effect of jet nozzle length or jet board spacing, and the effect of non-uniform velocity profile and turbulence intensity on

formation of the ground vortex. Laser Doppler velocimetry measurements have been made on the case chosen for further investigation in an attempt to better understand the means of formation and the reason for the unsteadiness of the ground vortex. The ground vortex flow field for the case of h/D equal to 5.5 and V_∞/V_j equal to 0.11 was chosen for further investigation because it was representative of applications and also because it was determined that blockage should be minimal in the prescribed parameter space. The present research program has been briefly summarized by Kuhlman and Cavage (1992).



a.) top view



b.) centerline side view

Figure 1.1: Schematic of Ground Vortex illustrating both a.) top view and b.) centerline side view.

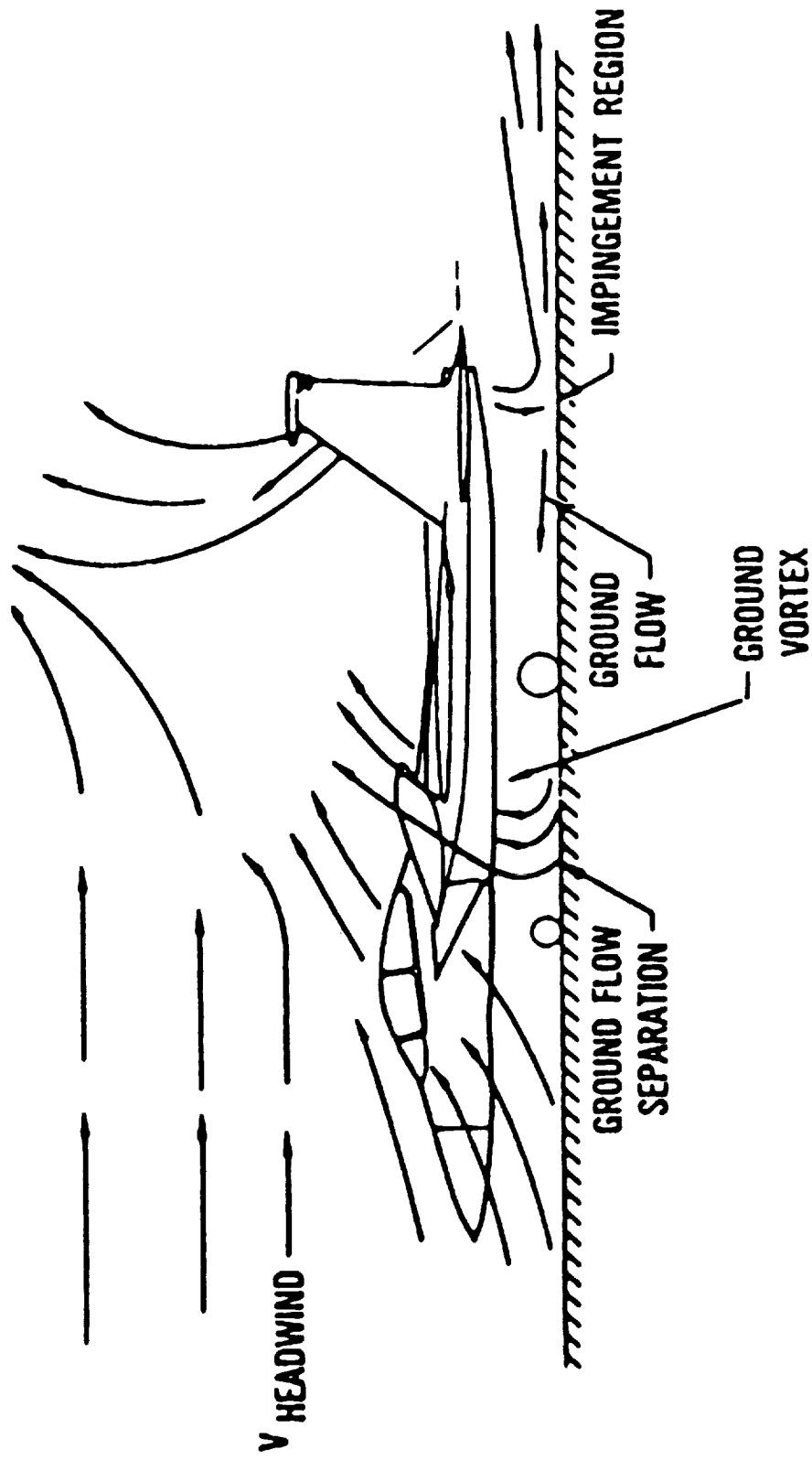


Figure 1.2: Schematic of flow field around F-15 SMTD with thrust reversers activated illustrating ground vortex formation (Blake and Laughrey, 1987).

CHAPTER 2: LITERATURE REVIEW

2.1 Turbulent Jets

A large body of information is available on turbulent jets issuing into a submerged fluid. Tennekes and Lumley (1972) outline the traditional analysis for a turbulent jet with the assumption it is a pure shear flow, and a brief discussion of self preservation is given. Self preservation is the term given to a turbulent flow when mean and turbulent velocity profiles collapse to unique curves for all axial stations. Wygnanski and Fiedler (1969) laid the original ground work for experimental studies of turbulent jets by making careful, well documented measurements of mean and turbulence quantities, including Reynolds stresses and RMS velocities, using a hot wire anemometer. Their experiments showed that although the mean behavior of a turbulent jet is self-preserving at 20 diameters from the nozzle exit as was thought before, the turbulence quantities are not self-preserving until approximately 70 diameters from the exit. This paper also documented the triple velocity correlations and explained their significance in turbulent free shear flows. Hussein, George, and Capp (1988) made the same types of measurements as Wygnanski and Fiedler, but with a two component laser Doppler velocimeter (LV), to study the errors due to intrusive hot wire probes which cannot detect flow reversals. Some significant errors were discovered, leading to better agreement with theory. Kuhlman and Gross (1990) made three component LV measurements in a self-preserving jet, further adding to the body of knowledge on turbulent jets.

A jet issuing into a cross flow out of ground effect has been studied extensively by Margason (1968), Keffer and Baines (1963), Kamotani and Greber (1972), and Wright

(1977). Margason used flow visualization to determine the centerline trajectory of a jet out of ground effect issuing into a cross flow at various large angles. Kamotani and Greber made hot wire anemometer measurements in both heated and unheated jets in a 90 degree cross flow and determined turbulence quantities. This study determined that the jet structure was dominated by a vortex wake which formed behind the jet. A semi-empirical model describing the trajectory of heated and unheated jets in cross flow was given by Wright. The jet trajectory is given as a power law which is derived using dimensional arguments. Keffer and Baines documented the "kidney bean" shape of the jet flow which is a direct result of uneven entrainment into the jet flow due to the cross flow. The vorticity associated with a jet in a cross flow was studied by Fearn and Weston (1974). This study made measurements of the velocity field with a rake probe in an attempt to develop an analytical model to describe the two counter-rotating vortices that form in the jet flow that give it the kidney bean cross sectional shape.

2.2 Annular Jets

A jet issuing from a nozzle that has some type of centerbody, which causes a low velocity central core and a non-uniform exit velocity profile, is classified as an annular jet. Some studies of annular jets have been performed illustrating the difference in behavior and structure from that of a uniform jet (eg, Ko and Lam, 1985). Ziegler and Wooler (1973) studied annular type nozzles both with and without cross flow and measured center line trajectories as well as pressure distributions on the plate from which the jet issued. These measurements showed that the jet exit plate pressure distribution changed very little due to

the different jet exit velocity profiles or conditions. Ziegler and Wooler also developed a method for determining an effective diameter and velocity for non-uniform exit velocity jets, to allow a rational nondimensional comparison with uniform velocity profile jets.

Kuhlman and Warcup (1978) studied several different annular jets produced by a concentric submerged center body inside the jet nozzle exit. Both hemispherical and a flat tipped centerbody were submerged different distances inside the jet exit, and pitot probe measurements were made to determine the centerline trajectory of a jet issuing into a uniform cross flow, as well as jet decay rate. It was determined that the jet with the fastest decay rate was the annular jet produced by a hemispherical tipped centerbody submerged 0.5 diameters inside the nozzle. The jet-induced pressure distribution on the jet plate was also measured, and was observed to be altered significantly by the annular jet. Kuhlman (1987) later showed this was a result of the increased entrainment due to the annular nozzle. A similar study was performed by Chassaing et. al. (1972), the focus of which was to relate the centerline trajectory for different velocity ratios and velocity profiles to a universal profile.

2.3 Impinging Jets

A radial wall jet is formed by an axisymmetric jet impinging at 90 degrees on a flat surface. The book by Rajaratnam (1976) contains a chapter on the radial wall jet. Analytical analysis is given as well as experimental data to show velocity profiles for different radial locations. The effect that impingement has on the free jet flow is also described. Experimental data illustrates that for impingement within 10 diameters of the jet exit, the jet retains a Gaussian distribution for 80 to 85 percent of the travel to the

impingement point. A thorough explanation of the behavior of a radial wall jet, as well as other related flows, is given. Padmanabham and Gowda (1991a, b) explain the effect of jet exit geometry on a radial wall jet in their two part paper. Mean flow characteristics are given as well as the turbulence quantities such as Reynolds stresses and normal stresses. It was shown that although the exit geometry effected the mean flow characteristics, it had very little effect on the turbulence quantities in the flow.

2.4 Ground Vortex Formation

Colin and Olivari (1969) examined ground vortex formation in an attempt to better define the conditions for hot gas ingestion. Their jet was seeded with helium and a simulated jet intake was positioned appropriately and evacuated to simulate a jet engine inlet. The concentration of helium was measured to determine the quantity of jet flow ingested into the inlet. Separation distance along the centerline (maximum) was measured for different velocity ratios. Abbott (1967) also performed experiments to measure the upstream separation point of the ground vortex for hot and cold jets although it is not clear how the author distinguished between separation location and maximum upstream penetration. Abbott was the first to perform both static and dynamic tests and notice a considerable difference in the results.

Cimbala, et. al. (1988) have examined ground vortex formation for various h/D and V_∞/V_j values and noticed poor agreement with the above mentioned works. Much of this was explained because Cimbala et. al. was a static test and Abbott was a dynamic test. Also the presence of a jet board, as opposed to a free jet in space was believed to cause

considerable blockage. Cimbala et. al. (1990) later focused on the unsteadiness of the ground vortex and the effect it has on ground vortex behavior. Two component LV measurements and energy spectrum data measured using a hot wire anemometer aided in the analysis of the unsteady behavior. The authors concluded that the fluctuations of the ground vortex were not correlated in time with respect to the jet flow or the cross flow. This could lead one to believe that the unsteadiness is caused by some large scale fluctuation which is caused by energy stored in, and then released from, the ground vortex itself.

Paulson and Kemmerly (1988) and Kemmerly and Paulson (1989) investigated the ground vortex formed by several different moving jet and moving model configurations with varying sink rates. These tests were compared to previous static model tests with considerable difference in results. The difference was attributed to different propulsive jet and trailing vortex interactions associated with static as opposed to dynamic tests. Stewart (1988) discusses the effect that the ground vortex has on different V/STOL configurations. Stewart (1989) also examines a ground vortex created by a moving model and gives extensive pressure data illustrating upstream penetration as well as vortex width. Stewart attributes differences in static and dynamic tests to different boundary layer interactions for the two separate cases, while Paulson and Kemmerly focus on the time lag of jet and wake trajectories for the dynamic case.

2.5 Laser Doppler Velocimetry

Laser Doppler velocimetry (LV) is a nonintrusive method of measuring fluid flow velocity with laser light scattered by seeding particles introduced into the flow. Principals of

LV have been explained in detail by Durst et. al (1981). Buchave (1983) discusses accuracy of three component LV measurements extensively and explains the significance of the optical configuration as well as other system specifications in obtaining good, consistent data. The difficulties in making good three dimensional measurements with an LV are explained by Meyers (1985). This paper illustrates that in adding a third component, there is a reduction in accuracy. The most accurate way to make LV measurements in three dimensions is with an orthogonal view, which is unattractive for large wind tunnels because it requires optical access on two adjacent sides.

Particle seeding bias has been the subject of many papers written on the subject of LV, with most of this work studying the effects of particle size and weight. For optimal accuracy, monodisperse particles are required, which are large enough to generate enough scattered signal, while being small enough to accurately track the flow. Due to the many conflicting theories and inconsistent data that had been reported relating to velocity bias, a panel of LV experts were assembled to determine some answers and report the findings. The results of this panel were reported by Edwards et. al. (1987). Although it seems an obvious point, the seeding particle must follow the flow, which can be a difficult requirement in turbulent flows. In other words, the particle must resolve the smallest scales of the turbulence. The Taylor microscale (T_λ) is a measure of the time a turbulent flow needs to change one standard deviation. Edwards et. al. determined that having more than one measurement point per T_λ in a time record could cause significant bias because the flow would not have had a significant chance to alter in such a small time. Coincidence is another problem associated with LV data biasing. Having coincidence allows a multi-component LV

system to assure each velocity component measurement in a time record was generated by the same particle. Although it is possible to obtain useful LV data for the mean flow without good coincidence, the Reynolds stresses and other turbulence information would be seriously biased. This is primarily because the different velocity components in the time record are not properly correlated in time. Thus, the turbulence information is not indicative of one eddy.

CHAPTER 3: APPARATUS AND PROCEDURE

3.1 Apparatus

The jet was aligned horizontally with the axial jet direction spanning the test section of the WVU low speed recirculating wind tunnel, using the glass test section side door as the ground plane to allow for optical access (figure 3.1). The test section has a cross section of 81.3 cm by 114.3 cm and is 121.9 cm long (32 by 45 by 48 inches). A blower, manufactured by Clements National, was chosen by use of the performance chart provided by the manufacturer and was used to supply the jet air flow. The air traveled from the blower, located at the back side of the wind tunnel, across the wind tunnel test section to the jet nozzle through a long plexiglas tube of 10.16 cm (4 inch) inner diameter as indicated in figure 3.1. The tube exited flush into an axisymmetric plenum which was machined out of aluminum round with a 10.16 cm inner diameter, and contracted to fit several aluminum interchangeable jet nozzles. To insure uniform flow entering the plenum, a flow straightener fabricated from plastic drinking straws of length to diameter aspect ratio of 8:1 was placed in the tube approximately 1 plenum diameter upstream of the plenum. A static pressure tap was machined in the plenum just before the contraction to allow for measurement of the plenum pressure. The plenum contracted with a 12.70 cm (5 inch) radius circular arc, while the nozzles completed the flow contraction by first continuing the 12.70 cm radius, if necessary, and then changing to a reverse curvature at a tangency point for the rest of the contraction. Appendix A gives a sample calculation of the critical dimensions for machining the 1.27 cm diameter nozzle, as well as a table of these dimensions for the three different diameter

nozzles. The reverse curvature, tangency point location, and arc length of each nozzle depended solely on the desired jet diameter.

The jet plenum was attached to the back side of a jet board consisting of a frame made from aluminum angle fitted with plexiglas panels with recesses machined to allow for a flush fit in the aluminum frame (figure 3.2). The jet board ran parallel to the glass test section door which acted as the ground plane, and spanned the height of the wind tunnel test section. The dimensions of the jet board were 81.3 cm high by 96.5 cm wide by 1.27 cm thick (32.125 by 38 by 0.5 inches). It had an elliptical leading edge and an ogive trailing edge to allow for smooth flow between the jet board and the ground plane. A schematic showing a top view of the jet-ground interaction facility has been given in figure 3.1. The jet board was mounted at four positions, one near each corner, on threaded rods that allowed for adjustment of the jet board spacing with respect to the ground plane, from outside the wind tunnel section. The jet board consisted of three major parts; a 14.0 cm wide center section, and two large panels approximately 32 cm wide, above and below the jet center section. The upper and lower panels could be removed to examine the effect of jet board confinement on the ground vortex (see figure 3.2).

Figure 3.3 gives cross sections of the three different diameter nozzles, and shows one of the nozzles mounted in the aluminum plenum. The three different nozzle diameters are 2.54, 1.27, and 0.95 cm (1, 0.5, and 0.375 inches) respectively. Since the plenum had a 10.16 cm diameter inlet these correspond to area contraction ratios of 16:1, 64:1, and 144:1. After the nozzle contraction, each jet nozzle had a certain nozzle length which the jet flow traveled before reaching the jet exit. Several different nozzle lengths have been used. Most

nozzles had a nozzle length which extended 2 diameters beyond the jet board, although nozzles having nozzle lengths of 4, 7, and 13 diameters were also fabricated and tested.

Two separate special nozzle configurations were also fabricated. First was a 1.27 cm diameter nozzle which was fitted with a turbulence generating plate of 0.47 cm diameter holes on staggered 0.635 cm centers, giving a 50% porosity. Second was a special annular nozzle made from a 1.27 cm diameter nozzle, but fitted with a 0.95 cm hemispherical tipped centerbody, or plug, positioned on the centerline of the nozzle 0.5 diameters inside the nozzle. This configuration resulted in a non-uniform exit velocity profile, with a high turbulence intensity and low velocity central core. A cross section of this nozzle can be seen as Figure 3.4. Both special nozzle configurations had a nozzle length of 2 nominal diameters beyond the jet board.

Smoke supplied by a commercial fog machine was injected into the blower inlet to visualize the ground vortex. The flow was examined in room light and recorded on video tape for future viewing with a VHS-C Video Recorder. A grid of one inch squares drawn on the glass ground plane aided in obtaining numerical values for x/D and y/D , the nondimensional x and y location of the maximum extent of the ground vortex. It has been determined that this ground vortex shape is a good indication of the average behavior of the ground vortex, and that this behavior is quite repeatable. The impingement point of the jet could be determined by examining fog fluid that tended to recondense on the glass ground plane which allowed for good flow visualization of the inner radial wall jet, especially near its origin. This fog fluid also tended to puddle at separation regions, giving the location of the separation line associated with the ground vortex. In addition, laser light sheet cuts have

been obtained of the ground vortex, using a 5W ion laser and a cylindrical lens to generate the light sheet.

Three component laser Doppler anemometer (LV) measurements have been made with a commercial three color DANTEC system which uses the same 5W argon ion laser. The three colors provide the three components of velocity and are given by the three wave lengths of light of 514.4 nm, 488.0 nm, and 476.5 nm. Table 3.1 gives the specifications of the three channels of the LV system. Figure 3.5 gives a top view of the LV system as positioned to make measurements in the jet-ground interaction facility. Polystyrene latex spheres of 0.6 micron diameter have been used as scattering sites, and were injected into the flow with a commercial agricultural atomizing spray nozzle. Numerical measurement of velocity data was provided by DANTEC counters and interface boards which allowed for the data acquisition by a DEC PDP-11. The raw data was then uploaded to a VAX computer where a FORTRAN data reduction program was utilized to compute transformed orthogonal mean and RMS velocity data, as well as to omit spurious outlier data.

3.2 Procedure

For calibration of the eight jet nozzles utilized in the flow visualization studies, a manual velocity traverse of each nozzle was obtained using a pitot static probe mounted on a dial caliper to allow for accurate distance measurement. The volume flow rate at the exit (Q) and momentum flux (MF) could then be obtained by numerically integrating the velocity profiles in radial coordinates. The pressure in the jet plenum was measured several times over the time period of traversing and an average was used to give a plenum pressure

corresponding to the Q measured for the nozzle. From this volume flow rate, V_j , the average jet velocity, was obtained. All pressures were read with two 40 inch water manometers. A program was written to perform the numerical integration for Q and MF. The program output consisted of Q and MF as computed from both sides of the traverse and an average, as well as calculation of effective diameter and velocity information to be discussed later.

Flow visualization has been performed in the jet-ground interaction facility to study the effect that several parameters had on the formation of the ground vortex. These parameters were the jet board-to-ground plane spacing (Z_b), the degree to which the flow field would nondimensionalize for different jet diameters (D), cross flow-to-jet flow velocity ratio (V_∞/V_j), jet exit turbulence intensity, and non-uniform jet exit velocity profile (using the annular or plugged nozzle). Also, tunnel blockage effects have been examined for different velocity ratios. The repeatability of data and different methods of calculating effective diameter were also explored. Data was obtained by setting the jet and wind tunnel velocity and seeding the jet flow with smoke from the commercial fog machine. The video recorder and/or 35 mm camera were then used to obtain a frontal view of the ground vortex for later review and quantitative analysis. In addition laser light sheet flow visualization has also been utilized to examine the structure of the ground vortex as well as to study the intermittent behavior. Both lateral and centerline laser light sheet "cuts" were observed and the results were video taped for later review.

To obtain a graph of the nondimensional shape and size of the ground vortex from the video tape data, the video in question was reviewed on a large color television monitor in a

dimly lighted room from several feet away to give maximum contrast. First, the maximum upstream penetration of the ground vortex was determined with a close up zoom of the leading edge of the ground vortex which is at the beginning of each data video run. Next the camera was zoomed back to view the entire ground vortex along the jet axis. Random x locations were then selected and the lateral extent of the ground vortex (y distance) was then measured by using the grid of one inch squares viewed on the glass ground plane. The x locations were taken randomly and out of order to allow for minimum data biasing. The ground vortex was assumed to be symmetric about the x axis and its lateral extent was measured both positive and negative and an average was taken giving the lateral extent from zero. In some cases, portions of the ground vortex were not viewable due to poor lighting or poor video technique. In these cases often only one point (positive or negative) was obtainable for lateral extent, thus reducing the accuracy of the value obtained. Note that the graphs presented in the Results chapter are simply the data plotted on the positive y axis and mirrored to the negative axis. Several runs were repeated on different dates to check repeatability and give a good indication of random error.

To obtain the desired velocity data the LV system was first properly aligned to obtain a good signal to noise ratio on all three channels, and to insure coincidence of the three probe volumes. An explanation of LV theory and methods can be seen in Appendix B. Seeding was injected in the wind tunnel plenum and also in the jet flow plenum in an effort to insure that no data biasing occurred. However, for the present study results have been obtained when only the cross flow was seeded. First a centerline ($y = 0$; an xz plane) data traverse was performed using a grid of 17 points ranging from 5 to 85 mm above the ground

plane in the z direction (vertical) at 9 different x locations ranging from 200 to 40 mm upstream. Next, one lateral traverse through the leg of the ground vortex has been performed at the x location of 100 mm downstream of the jet exit. The y coordinate was varied from 0 to 200 mm from the jet centerline for the z locations of 15, 30, 40, and 50 mm from the ground plane. The lateral measurements have been performed assuming the ground vortex is symmetric about the x axis at $y = 0$.

Table 3.1: Specifications of DANTEC three color laser Doppler velocimeter.

Specification	514.4 nm	488.0 nm	476.5 nm
Focal length of lenses			
imaging lens	600.0 mm	600.0 mm	600.0 mm
collecting lens	600.0 mm	600.0 mm	600.0 mm
Beam diameter, at e^{-2} intensity of laser	2.375 mm	2.313 mm	2.285 mm
Beam half-angle	2.4836°	2.4597°	2.3163°
Fringe separation	5.936 μm	5.685 μm	5.889 μm
Major and minor axis to e^{-2} intensity	3.82 mm 0.16 mm	3.76 mm 0.16 mm	3.94 mm 0.16 mm
Number of fringes	28	28	27

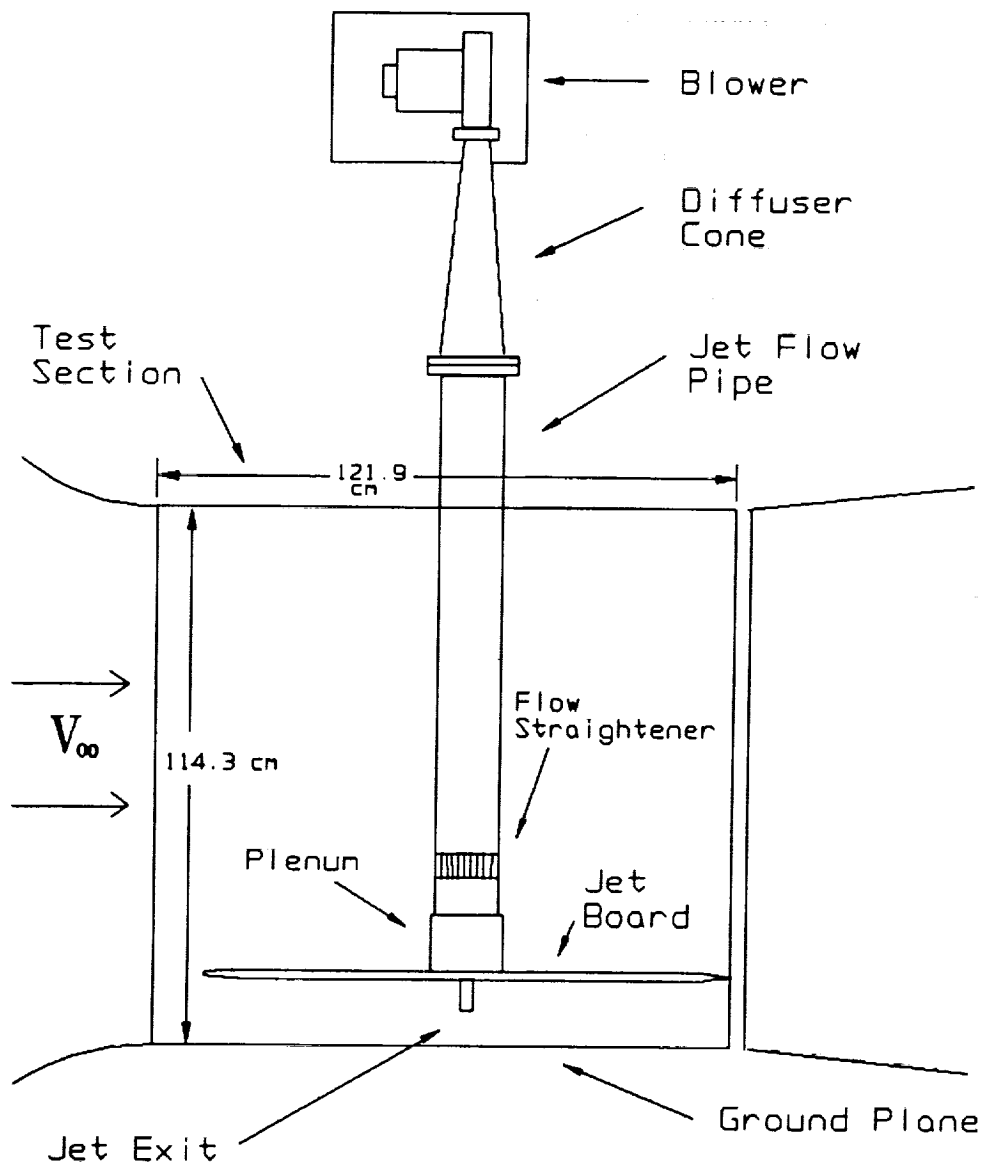


Figure 3.1: Top view of jet-ground interaction facility.

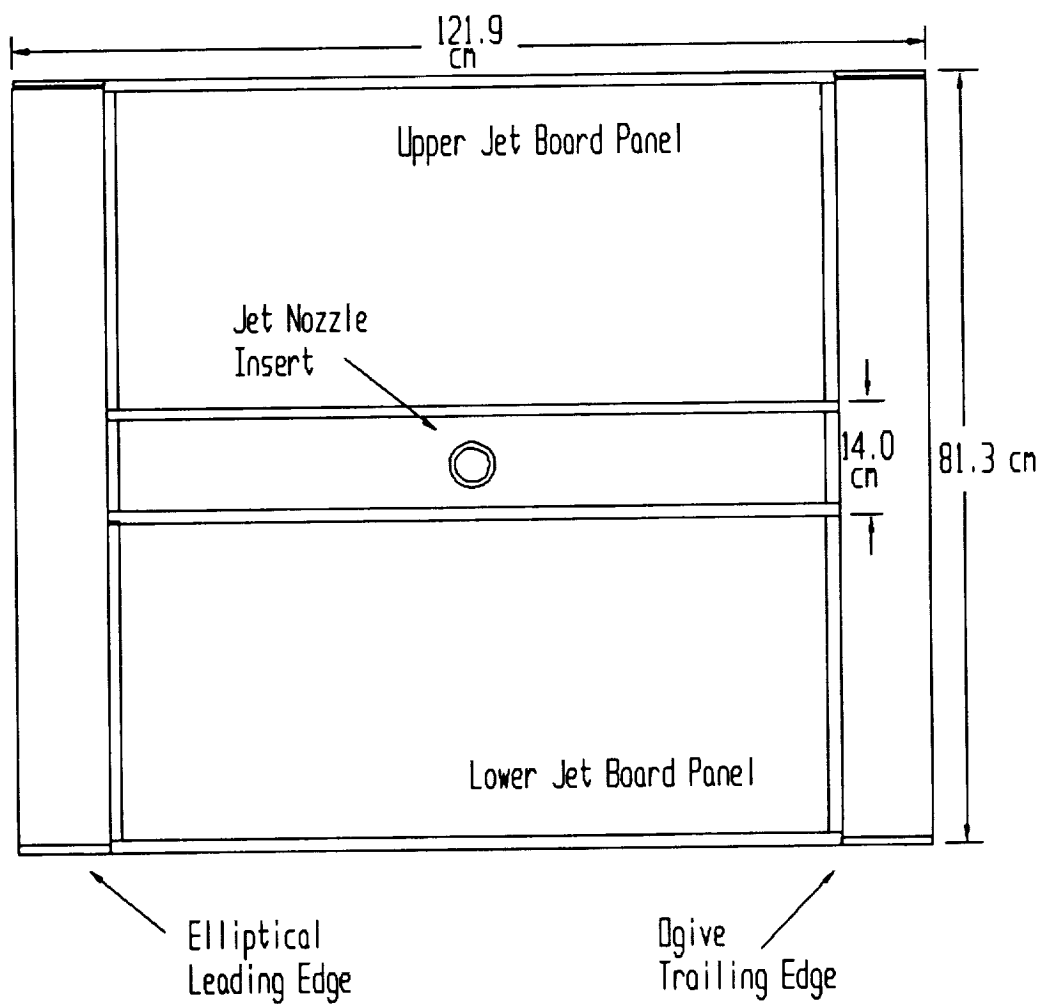


Figure 3.2: Jet-ground interaction facility jet board.

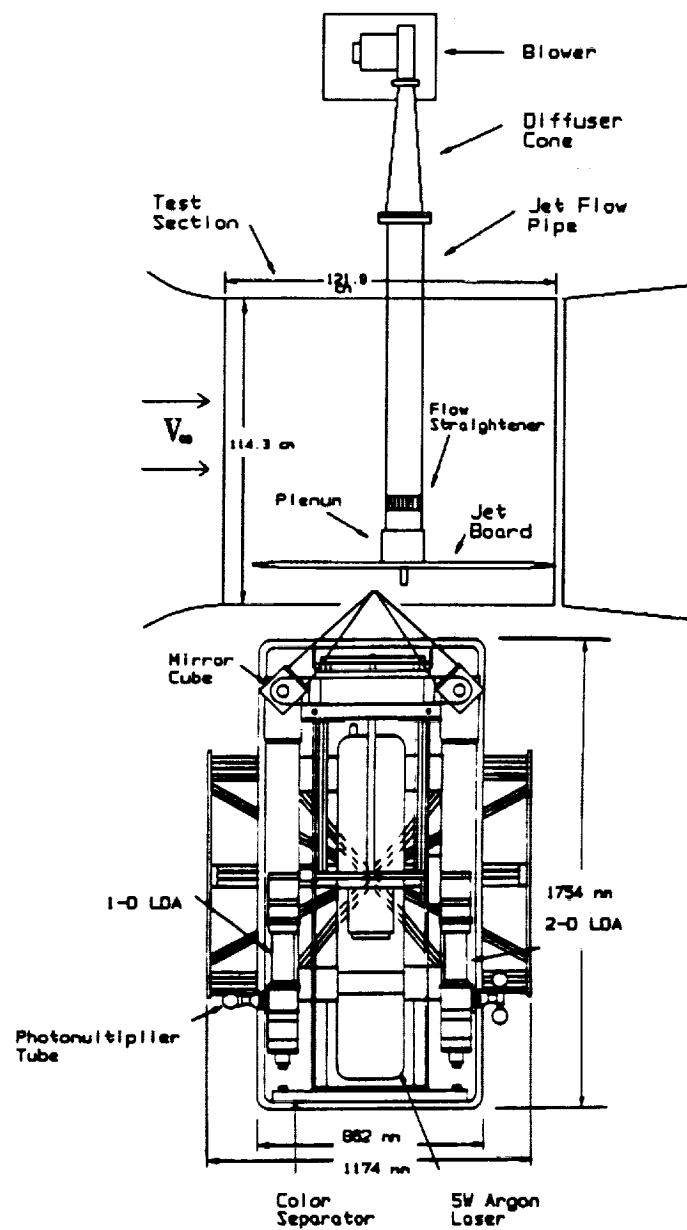


Figure 3.5: Top view of LV system positioned with jet-ground interaction facility.

CHAPTER 4: THEORETICAL BACKGROUND

4.1 Description of Jet Behavior

Fluid flowing from an orifice into a submerged fluid is termed a jet flow. As the jet fluid enters the submerged fluid the turbulent shear layer formed causes the jet to grow in width, while the centerline velocity slows as the jet loses momentum to the surrounding fluid. At some distance from the jet exit, the lateral velocity profile can be described by a universal profile which is approximately Gaussian in nature. The jet mean flow is said to be self-preserving at this point and this self-similar velocity profile gives the velocity distribution for axial locations beyond which the jet is self-preserving.

The present work considers axisymmetric turbulent jet flow. The Reynolds number for a jet can be described by the following equation.

$$Re = \frac{UD}{\nu} \quad (4.1)$$

In this equation ν is the kinematic viscosity, D is jet diameter and U is jet velocity.

Dimensional physical analysis of axisymmetric turbulent jet flow as a free shear flow for jet centerline velocity ($U(x)$) and jet width ($b(x)$) as functions of x gives the following relations, which match experimental observations.

$$U(x) \sim 1/x$$

$$b(x) \sim x$$

Where the width of the jet $b(x)$ is the lateral extent of the jet at a given axial location x .

Although the far field behavior of turbulent jets can be described analytically (in the self-

preserving region), the near field behavior of turbulent jets is not so easily defined and has no analytical description or well defined theory.

Two important integral characteristics of a jet are the initial volume flow rate and the integrated momentum flux hereafter referred to as momentum flux. Initial volume flow rate allows for the calculation of the initial average velocity while volume flow rate at several longitudinal (jet-wise) locations gives the entrainment rate into the jet. Entrainment rate is a measure of how well a jet mixes with the ambient fluid. The virtual origin is a measure of the near field entrainment rate of a jet. It can be defined as a point along the centerline of the jet axis defined by the crossing point of a line which consists of the lateral extent (width) of the jet at all the longitudinal locations (figure 4.1). A uniform velocity profile, with a thin wall boundary layer, has a positive virtual origin, while jets with thick wall boundary layers, such as fully developed pipe flow, have negative virtual origins, or virtual origins inside the jet. The integrated momentum flux of an ideal jet nozzle is constant for all longitudinal jet locations.

Volume flow rate is defined by the following equation where V is the average velocity and A is the jet exit area.

$$Q = UA \quad (4.2)$$

Considering non-uniform velocity exit conditions, the velocity must be integrated over the jet exit area.

$$Q = \int U dA \quad (4.3)$$

For an axisymmetric jet with radius R and radial velocity profile $U(r)$, dA is equal to $2\pi r dr$

giving equation (4.4).

$$Q = 2\pi \int_0^R U(r) r dr \quad (4.4)$$

Similarly momentum flux for an axisymmetric jet of radius R with radial velocity profile $U(r)$ and fluid density ρ is defined below as equation (4.5).

$$MF = 2\pi\rho \int_0^R U(r)^2 r dr \quad (4.5)$$

4.2 Effective Diameter Calculation

The concept of an effective diameter was first developed by Ziegler and Wooler (1973) and then by Kuhlman and Warcup (1978). These studies, as well as others, were interested in examining the effects of different nozzle configurations, such as the annular or swirl nozzle, on various jet flow field characteristics such as entrainment or decay rate. Such studies concentrate on altering the jet near field behavior, by using a variation from the usual uniform jet exit velocity profile to a non-uniform velocity profile. However, it becomes obvious that it is not consistent to make a nondimensional comparison between annular and uniform jet results compared in terms of actual jet diameter. Ziegler and Wooler reasoned that a non-uniform exit velocity profile could be expressed nondimensionally in terms of its initial volume flow rate and momentum flux, yielding an effective diameter for a uniform velocity profile. This could be accomplished by accelerating

an ideal, uniform jet from the same stagnation conditions as the nonuniform velocity profile to the same exit pressure, while maintaining the same initial volume flow rate and momentum flux.

Following Kuhlman and Warcup (1978), to obtain the effective diameter, first Q has been calculated from measured velocity profiles and used to determine the initial mass flow rate. Next an equivalent momentum flux has been calculated using the maximum dynamic pressure (q_{\max}) measured at the jet exit as the reference dynamic pressure.

$$MF = \dot{m} \sqrt{\frac{2RT_0 q_{\max}}{P_0 + \frac{(\gamma-1)}{\gamma} q_{\max}}} \quad (4.6)$$

This effective momentum flux was then used to calculate an effective area, from which effective diameter was calculated easily.

$$A_{eff} = \frac{MF}{2q_{\max}} \quad (4.7)$$

$$D_{eff} = \sqrt{\frac{4A_{eff}}{\pi}} \quad (4.8)$$

The corresponding effective velocity has been determined from the continuity equation.

$$V_{eff} = \frac{Q}{A_{eff}} \quad (4.9)$$

A more detailed explanation of this procedure has been given in Appendix C. The effective diameters calculated by this procedure are reduced for the annular jet relative to the uniform jet, tending to increase the size of the ground vortex when plotted nondimensionally.

4.3 Nozzle Calibration Data Reduction Program

To perform the numerical integration of the measured velocity profiles and also to calculate effective diameter and velocity a program has been written in the language QuickBASIC. Input data files consist of the velocity traverse measurements, atmospheric temperature and pressure, as well as information pertinent to the particular nozzle geometry. Output consisted of data files as well as printed copy, if requested, containing calculated initial volume flow rate, momentum flux, average velocity, effective diameter, and effective velocity. The ratio of initial volume flow rate to volume flow rate based on maximum dynamic pressure at the jet exit and exit area, the ratio of momentum flux to momentum flux based on maximum dynamic pressure at the jet exit and exit area, and the discharge coefficient were also calculated in the program and examined to allow for a better understanding of the calibration of each nozzle.

Two different methods of numerical integration have been used to calculate Q and MF. A modified version of Simpson's rule which has been altered to allow for unequal Δr increments across the interval of integration was utilized as the primary integration scheme (Katsikadelis and Armenakas, 1984). Equation (4.10) describes the modified Simpson's rule giving the area under a curve connected by three points with interval steps S_1 and S_2 with end values f_1 and f_2 and mid value f_0 .

$$A = \frac{(f_0 - f_1) S_2^3 + (f_0 - f_2) S_1^3 + S_1^2 S_2 (2f_1 + 3f_0 + f_2) + S_1 S_2^2 (f_1 + 3f_0 + 2f_2)}{6 S_1 S_2} \quad (4.10)$$

Figure 4.2 illustrates the use of the above equation for numerical integration. When

substituting S in for S_1 and S_2 for uniform spacing, this formula simplifies to the standard Simpson's rule. The numerical integration has also been performed with the trapezoidal rule as a check for the Simpson's rule routine.

Due to discrepancies in the measurement of the velocity profiles, the program altered the original raw data to create two velocity profiles from the one traverse. First any redundant zero points were eliminated at the edge of the integration. Next the program found the centerline of the jet by finding the midpoint between two points in the shear layer where the local velocity was exactly half of the jet maximum velocity. The program then eliminated any velocity points that were greater than the radius of the jet (eg, $u(r) > 0$ for $r > R$). These points existed because of inaccuracies associated with the use of a pitot probe in a highly turbulent flow field (ie, in the turbulent shear layer). Figure 4.3 is an example of a raw velocity traverse and velocity profile as altered by the program, which reveal the discrepancy between the two. Figure 4.4 and 4.5 are illustrations of the integrand for initial volume flow rate and momentum flux respectively.

Effective diameter and velocity were calculated by the program using three different methods to check and verify the results as well as the logic behind the argument for effective diameter. The first method is the method which has been described in section 4.2, which is also the method which has been used to nondimensionalize the acquired data for non-uniform jet ground vortex formation. The second method is the original method developed by Ziegler and Wooler (1968) which varies from the above method by first calculating an equivalent nozzle dynamic pressure using the measured momentum flux, and then calculating effective area and velocity. The third method which was explored is simply using the calculated

momentum flux, and measured maximum dynamic pressure. A listing of the data reduction program is given in appendix D along with a sample data input file and example program output.

4.4 Analysis of Ground Vortex Formation

To describe the lateral extent of the ground vortex, potential flow arguments can be developed, by relating a line source flow strength to maximum upstream penetration of the ground vortex (Colin and Olivari, 1969). Consider the superposition of a source flow at the origin and a uniform flow. The equation for the stagnation streamline of this potential flow field is given below.

$$\frac{q}{2\pi} \tan^{-1}\left(\frac{Y}{X}\right) - u_{\infty}Y = 0 \quad (4.11)$$

In the above equation $(q/2\pi)$ represents the source strength and u_{∞} is the uniform flow magnitude. Considering the maximum penetration of the ground vortex at y equal to zero (the stagnation point), gives the following relation.

$$X_{P_{\max}} = \frac{q}{2\pi u_{\infty}} \quad (4.12)$$

Substituting (4.12) into (4.11) and simplifying gives a relation relating x and y coordinates of a ground vortex in terms of $X_{P_{\max}}$.

$$X_{P_{\max}} \tan^{-1}\left(\frac{Y}{X}\right) - Y = 0$$

$$\tan\left(\frac{Y}{X_{P_{\max}}}\right) = \frac{Y}{X} \left(\frac{X_{P_{\max}}}{X_{P_{\max}}}\right)$$

$$\frac{X}{X_{P_{\max}}} = \frac{\frac{Y}{X_{P_{\max}}}}{\tan\left(\frac{Y}{X_{P_{\max}}}\right)} \quad (4.13)$$

Note that in this model, the downstream shift of impingement point as velocity ratio increases has been ignored.

Another relation that may predict the shape and size of the ground vortex was suggested by Wright (1977). Wright develops nondimensional arguments and obtains an expression for the trajectory of a jet in a cross flow out of ground effect. Since the expression was developed considering the momentum exchange of the two flow fields, it could be reasoned that it might be applicable to the case of a jet in a cross flow in ground effect. Translating the data to have the origin at the leading edge of the ground vortex and using the Wright relations, gives the following nondimensional x and y, expressed here as X' and Y'.

$$Y' = \frac{YV_{\infty}}{DV_j} \quad (4.14)$$

$$X' = \frac{(X - X_{P_{\max}}) V_{\infty}}{DV_j} \quad (4.15)$$

X' and Y' are related by the following expression.

$$Y' = C(X')^{1/3} \quad (4.16)$$

In the above equation C is an unknown constant experimentally observed to be approximately

1.2 for the application of ground vortex formation.

To compare the two methods to determine which method has best agreement with obtained experimental data, one needs to make a rational comparison of the two different methods of nondimensionalization. To do this first consider the nondimensional parameter λ^* which is defined below.

$$\lambda^{*2} = \frac{P_i}{q_\infty} \quad (4.17)$$

In equation (4.17), P_i is the impingement pressure on the ground plane. Considering a small jet exit spacing ($h/D < 4$), P_i is approximately equal to q_j leading to the following relation.

$$\lambda^* \approx \sqrt{\frac{q_j}{q_\infty}} \quad \rightarrow \quad \lambda^* \approx \frac{V_j}{V_\infty} \quad (4.18)$$

It has been experimentally observed by Colin and Olivari (1969) that λ^* relates to $X_{P_{max}}$ by the following relation.

$$X_{P_{max}} = C(\lambda^*)^{0.9} \quad (4.19)$$

In equation (4.19) C is a constant observed to be 1.03 for the experiments of Colin and Olivari. The present study utilizes the value for C of 0.7, which tends to be more representative of the flow visualization data observed. Expanding equation (4.16) and substituting equation (4.18) gives the following relation.

$$\frac{Y}{D\lambda^*} = 1.2 \left(\frac{X - X_{P_{max}}}{D\lambda^*} \right)^{\frac{1}{3}} \quad (4.20)$$

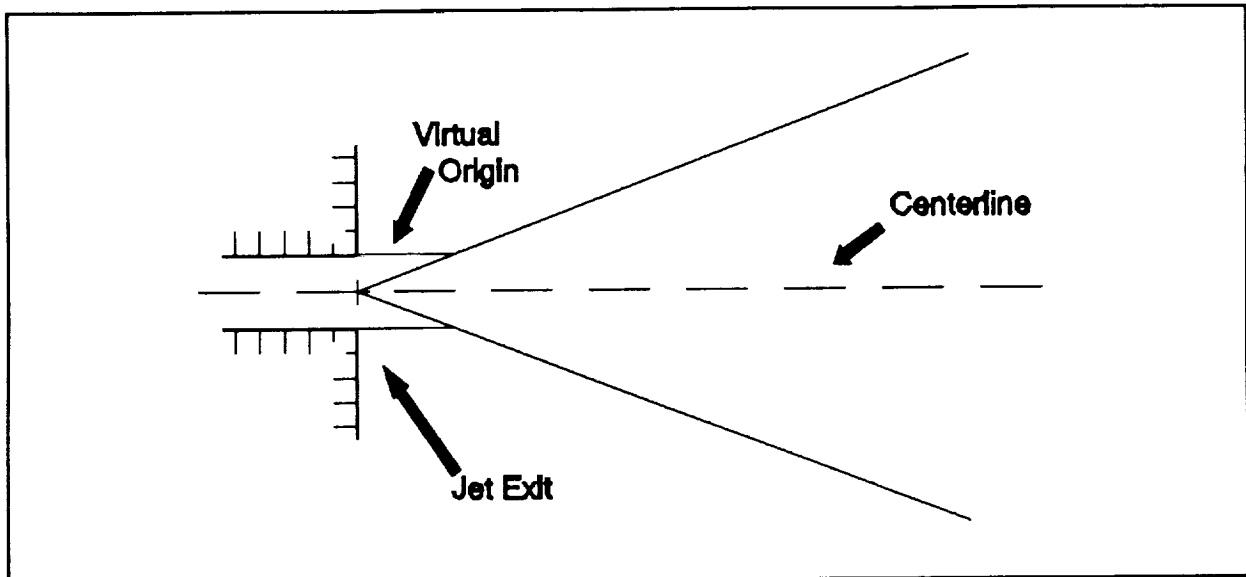
Simplifying (4.20) and eliminating D with (4.19) gives the following equation.

$$\frac{X - X_{P_{\max}}}{X_{P_{\max}}} 0.7 (\lambda^*)^{0.9} = \frac{1}{(1.2)^3 (\lambda^*)^2} \left(\frac{0.7 (\lambda^*)^{0.9} Y}{X_{P_{\max}}} \right)^3 \quad (4.21)$$

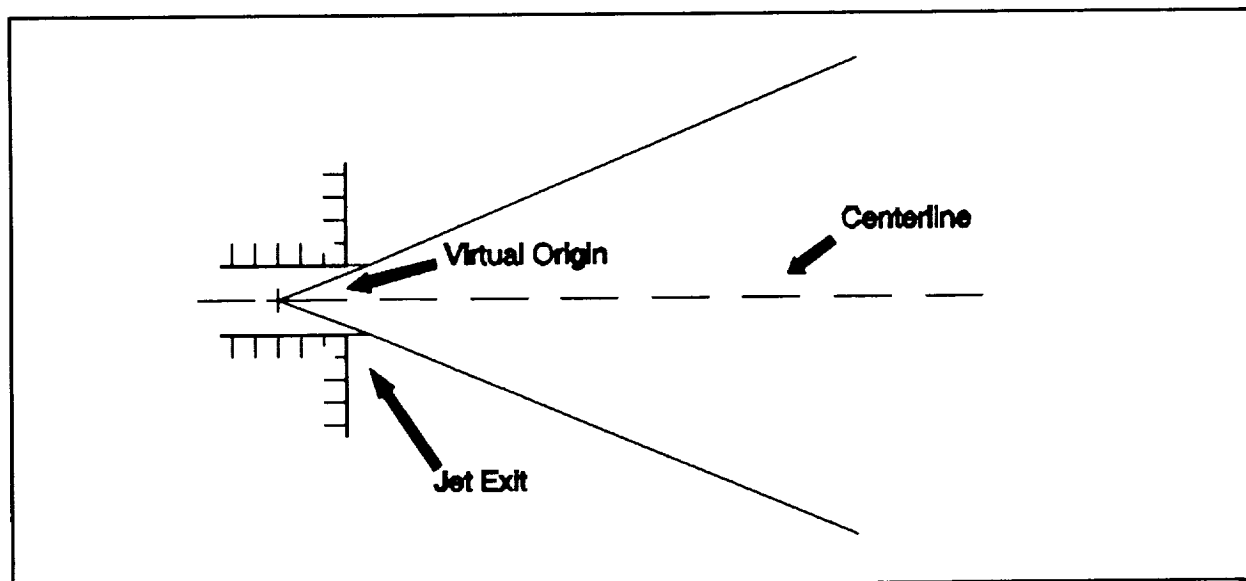
Realizing that the above equation is a weak function of λ^* over the interval of velocity ratios for the present study (varies between 0.6 and 0.71) and using the average value gives an expression relating x and y nondimensionalized with $X_{P_{\max}}$.

$$\frac{X}{X_{P_{\max}}} = 0.28 \left(\frac{Y}{X_{P_{\max}}} \right)^3 + 1 \quad (4.22)$$

Equation (4.22) relates equation (4.16) in terms of $X_{P_{\max}}$ to enable a comparison with equation (4.13) to verify how well the two methods compare.



a.) poor mixing



b.) good mixing

Figure 4.1: Illustration of virtual origin for a.) poor and b.) good near field mixing.

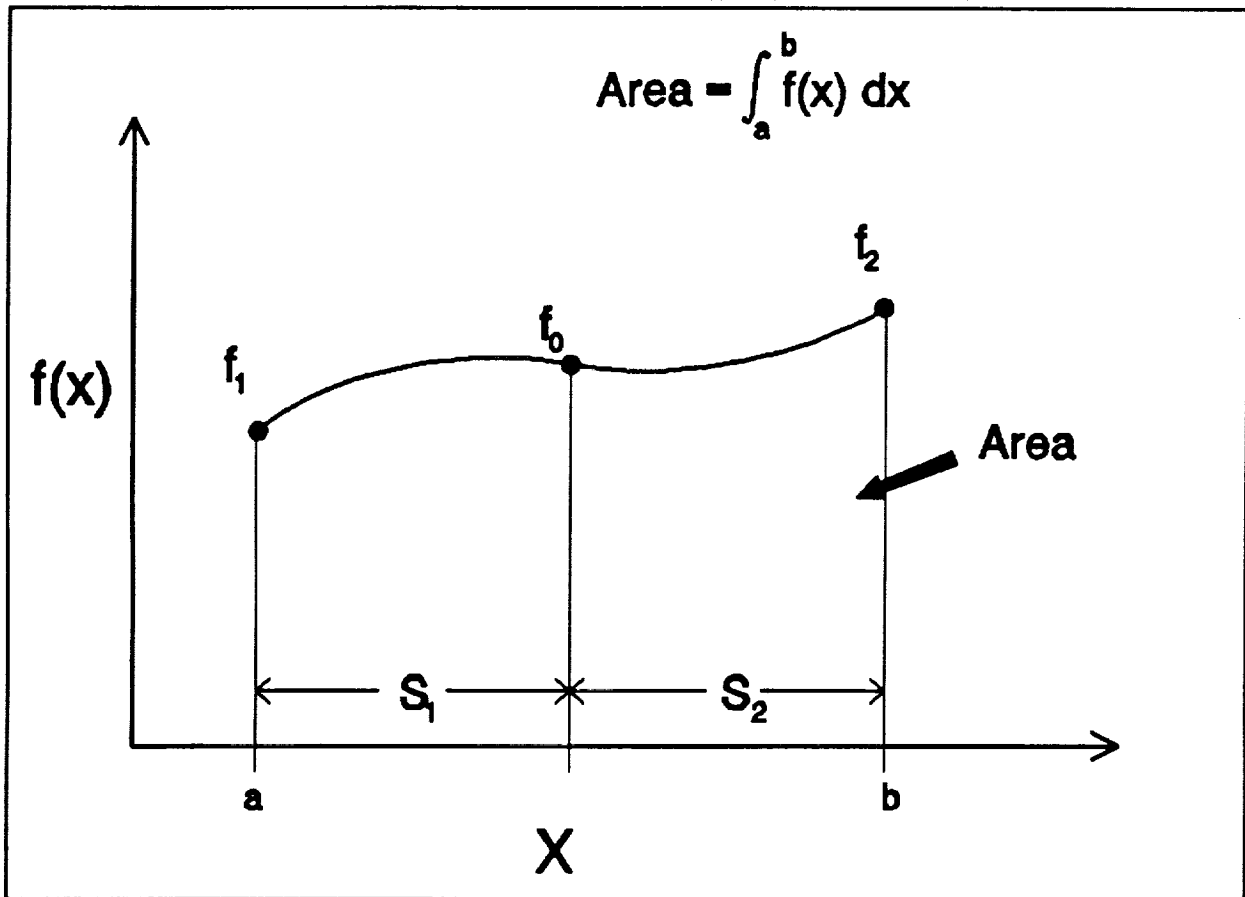


Figure 4.2: Illustration of equation (10) defining the significant dimensions for modified Simpson's Rule

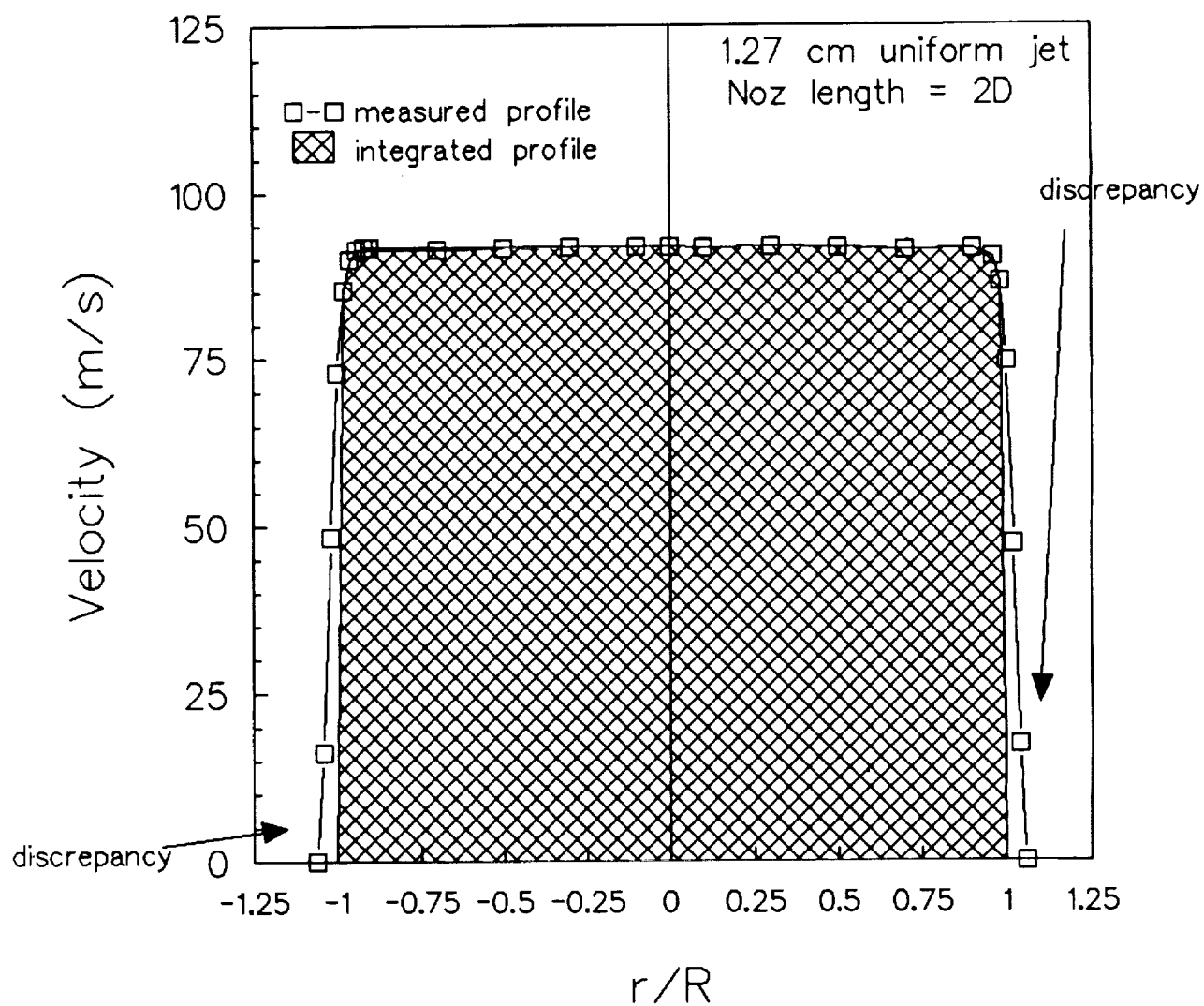


Figure 4.3: Example of a measured velocity profile with the velocity profile altered by the program for integration.

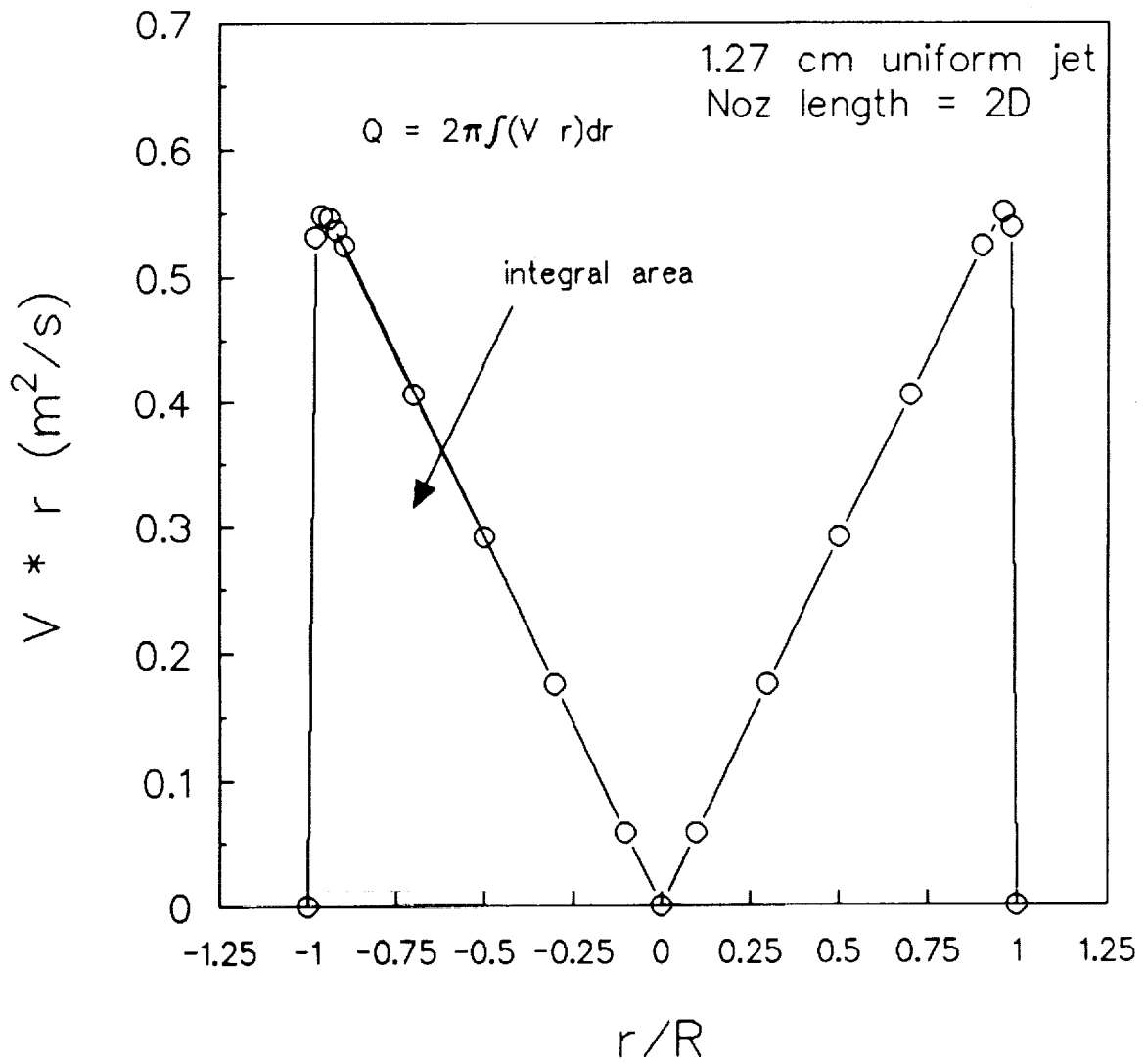


Figure 4.4: Illustration of integrand for volume flow rate.

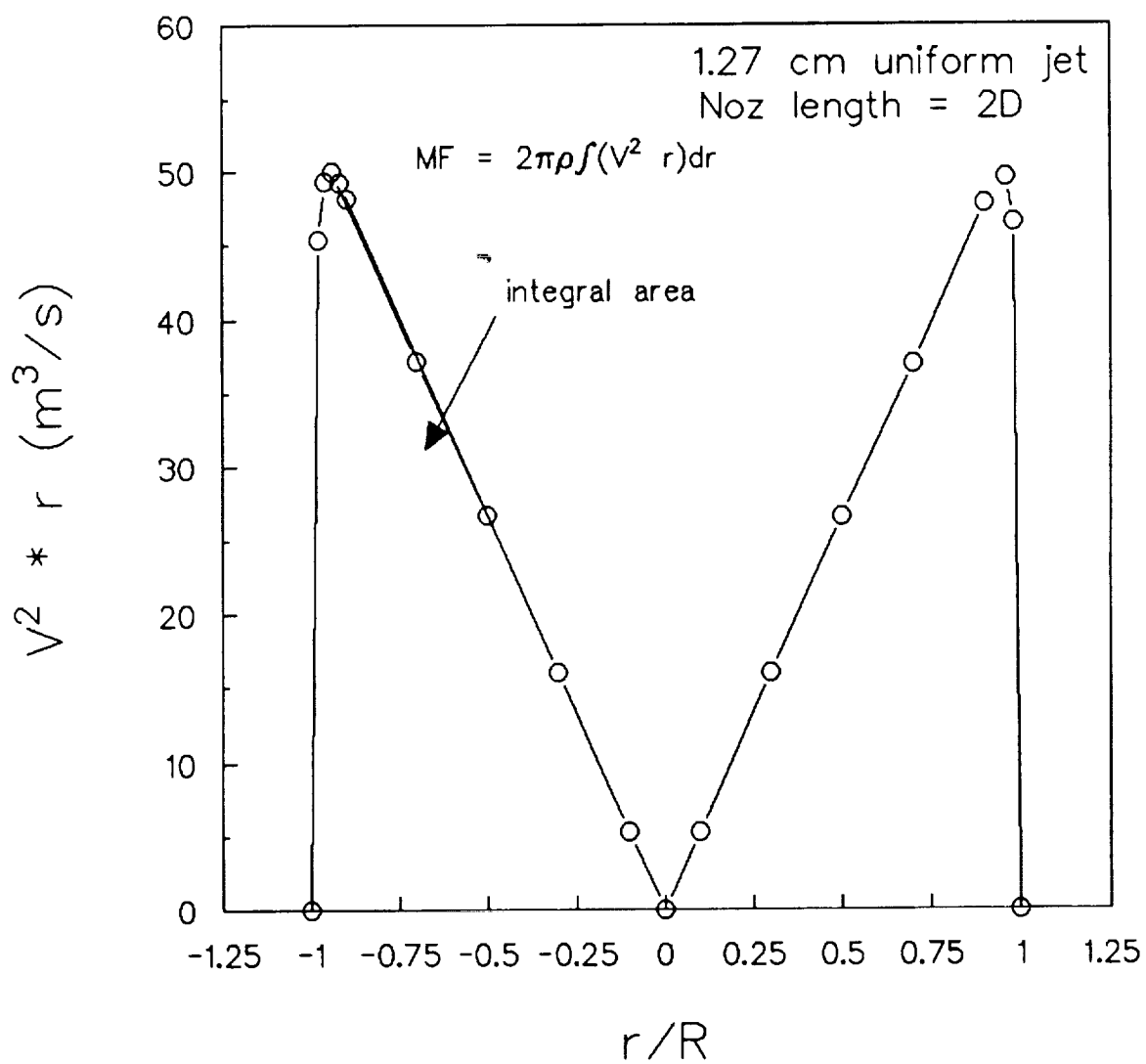


Figure 4.5: Illustration of the integrand for momentum flux.

CHAPTER 5: RESULTS

5.1 Nozzle Calibration

The present results have been summarized by Kuhlman and Cavage (1992). Results of horizontal and vertical velocity traverses through the centerline at the jet exit for each of the eight nozzles which have been calibrated in the present study are presented in Figures 5.1 through 5.8. These velocity data have been obtained using a pitot static probe, as described in section 3.1. Notice the excellent symmetry and uniformity of the velocity profiles for all nozzles. Table 5.1 summarizes the results of the calibration for the eight nozzles as calculated by the data reduction program. Note that the velocity profiles for all of the standard nozzles and the high turbulence nozzle were nearly uniform in nature (average velocity approximately equal to 98% of V_{max}), and thus the calculated effective diameters were very close to the actual jet diameter (within 2%). This allowed nondimensionalization of the data using the actual jet nozzle diameters except for those cases specifically comparing the annular nozzle with uniform nozzles.

Some sources of inaccuracy associated with the pitot static measurements made for the calibration of the eight nozzles utilized in the present study have been mentioned in section 4.3. Low accuracy of pitot static probe velocity measurements in a highly turbulent flow field is largely due to the inability of the probe to detect flow reversal near the edge of the jet, although there is also error due to the turbulent velocity fluctuations which are too rapid for the probe to respond to. For the uniform nozzles, most of the velocity traverse (approximately 90%) had very small turbulence fluctuations. Only the data in the jet shear

layer had high turbulence levels or large fluctuations. Velocity traverses for the annular nozzle were believed to be less accurate because the velocity profile consisted of a wake flow within the two jet shear layers, with no uniform flow in the velocity profile. Most of the error associated with the calibration of the annular nozzle can be attributed to the recirculating annular vortex that exists at the low velocity central core of the nozzle (Ko and Lam, 1985). The pitot static probe could only detect the positive velocity portion of this vortex, and not the reverse vortex flow back into the nozzle, resulting in some net error in volume flow rate that gave a value slightly less than that of the measured value. This value is estimated to be no more than approximately a 10% overestimation of Q .

The average velocity for each nozzle in the present study has been held fixed at approximately 91.5 m/s (300 ft/s) corresponding to an exit Mach number of approximately 0.3. This yielded approximate Reynolds numbers based on jet diameter of 153400, 76700, and 57500 for the 2.54, 1.27, and 0.95 cm diameter jets respectively.

5.2 Flow Visualization of Ground Vortex

To examine the effect of the ground board spacing on the ground vortex size, several different 1.27 cm diameter nozzles, each with a different nozzle length, have been used to compare the ground vortex for each nozzle at the same h/D while varying the spacing between jet board and ground board, Z_b . Cimbala et. al. (1988) determined that a significant difference in ground vortex behavior could be observed if the jet board location Z_b/D was equal to the h/D of the nozzle (ie, an external nozzle length of zero). They also observed that a Z_b/D of 2 diameters greater than h/D was the limiting case for the jet board to

influence the ground vortex size or shape in their experiments. Somewhat different were the observations of Spreeman and Sherman (1958), who observed no significant change in suck down behavior for a nozzle length of 0 to 3 jet exit diameters for an impinging jet in hover. For the present study with a constant h/D equal to 4.34, and at $V_\infty/V_j = .11$, Z_v/D has been varied as 6.34, 8.34, and 17.34, (nozzle lengths of 2, 4, and 13 diameters respectively) as well as a case with Z_v/D equal to 17.34 with the upper and lower jet board panels removed (see Figure 3.2), leaving only the 14.0 cm (5.5 inch) wide center section to confine the ground vortex between the ground board and jet board. These results have been presented in figure 5.9. Only a small but noticeable reduction in ground vortex upstream penetration is seen for the two cases with $Z_v/D = 17.34$. This would lead one to conclude that the presence of a jet board, regardless of spacing, has only a very small effect on the ground vortex shape and size after a nozzle length of 2 diameters or greater, consistent with Cimballa et. al., (1988).

To examine the nondimensional collapse of the ground vortices formed by the various nozzles, the ground vortices formed by the 2.54, 1.27, and 0.95 cm diameter jet nozzles (1, 0.5, and 0.375 inch diameter) have been examined for the case of h/D equal to 7 and V_∞/V_j equal to 0.14 (figure 5.10). This case has been chosen because of the relatively small size of the ground vortex formed in the present facility at these nondimensional parameter values. The nondimensional shapes of the ground vortices for the above mentioned nozzles agree very well, with a small but consistent trend that the 2.54 cm nozzle tends not to penetrate as far upstream as the others with the 0.95 cm nozzle having the greatest upstream penetration. This is most likely due to blockage effects caused by the large volume flow rate of the larger

jet in the flow channel formed by the ground board, the jet board, and the wind tunnel walls. The data does, however, appear to have good nondimensional agreement in the above mentioned parameter space.

To examine the effects of tunnel blockage for ground vortices of different sizes, the three different nozzles have been tested at the frequently studied configuration of $h/D = 3$ for a range of velocity ratios. Figures 5.11, 5.12, 5.13 and 5.14 show the measured nondimensional shape of the ground vortex for V_∞/V_j equal to 0.1, 0.125, 0.15, and 0.18 respectively. Due to facility limitations the jet board spacings for the 0.95, 1.27, and 2.54 cm diameter nozzles were 10, 7, and 5 respectively. Again, the data generally exhibits good nondimensional agreement, at least for the higher velocity ratios and smaller jet nozzles. In figure 5.11 the lateral extent or half width of the vortex for $x \geq 0$ does not agree well. This is probably due to confinement of the vortex by the tunnel side walls, which causes some blockage for the case of the 1.27 cm diameter jet. The 2.54 cm jet had a ground vortex which was too large to include in this data set, although the same effect can be seen for the 2.54 cm nozzle in figure 5.12 at $V_\infty/V_j = 0.125$. Due to the physical size of the ground vortex formed by the 2.54 cm jet, the sides of vortex pass as close as 3 or 4 diameters to the sidewalls of the tunnel for this case preventing the vortex from spreading laterally. Notice the better agreement of the nondimensional data for the greater velocity ratios (figures 5.13 and 5.14). These velocity ratios have considerably smaller ground vortices which result in insignificant blockage due to confinement by the tunnel side walls for the larger jet nozzle.

Figures 5.15, 5.16, and 5.17 show the ground vortex shape for the 0.95, 1.27, and 2.54 cm diameter nozzles, respectively at h/D equal to 3 for various V_∞/V_j values. These

figures illustrate the change in shape and size of a ground vortex with velocity ratio. Notice that the ground vortex appears to become more blunt at the upstream centerline location as the velocity ratio increases. Next, the maximum upstream penetration (on the centerline) of the ground vortex has been plotted in figure 5.18, for the three different diameter jets and for two different data sets taken. This figure gives a good idea of the repeatability of data, showing scatter of about 5 to 7 percent for all various nozzles.

The maximum upstream location of the separation point, which also occurs at y/D equal to zero, has been examined extensively by Cimbala et. al., (1990) and is a measure of the strength of the jet relative to the cross flow. The maximum separation points, nondimensionalized by jet diameter and measured relative to the impingement point location, of the ground vortices for various values of V_{∞}/V_j at $h/D = 3$ have been plotted in figure 5.19. Note in figures 5.15-5.17 that for most velocity ratios (less than 0.125), the measured impingement point is essentially zero. Although the data trends in figure 5.19 are all very similar to one another, the magnitude of the data is considerably different for the 1.5 inch jet of Cimbala et. al., (1990). There is some question as to the trend of the Cimbala data to have a constant x/D difference of two between the 3 inch jet and the 1.5 inch jet. Blockage, which has been attributed to the trend observed by Cimbala et. al., should tend to affect the lower velocity ratios more than the higher velocity ratios. This is contrary to the data obtained by Cimbala et. al., for the 1.5 inch jet, which indicates that blockage causes approximately the same change in upstream penetration for all velocity ratios. The separation point determined for the present work tends to fall on the 3 inch jet results from Cimbala et. al. This aside, good nondimensional agreement is evident for the present data,

although the 2.54 cm jet tends to deviate from the 1.27 cm jet at the lowest velocity ratio range at which they were compared. This, as explained above, can be attributed to increased blockage.

The separation data above as well as results from Abbott (1967) and Colin and Olivari (1969) have been presented in figure 5.20 in terms of the parameter λ^* (see section 4.4). Due to the fact that the jet impingement pressure has not been measured, the present study assumes that the jet impingement pressure is equal to q_j . This is a good assumption since jet decay is very small within 4 jet exit diameters for a uniform jet exit velocity profile (Rajaratnam, 1976). Also presented in figure 5.20 is another data set from Cimbala et. al., (1988). With the exception of the theoretical curve by Colin and Olivari, the data sets are very comparable. The empirical curve developed by Abbott does have a considerably different slope than a line that would pass through the present data, although the agreement of the line over the interval of selected velocity ratios is good.

Next the data obtained for the various velocity ratios has been nondimensionalized in accordance with equation (4.13) by using $X_{P_{max}}$. Figures 5.21, 5.22, and 5.23 give the data for different velocity ratios nondimensionalized with $X_{P_{max}}$ for the 0.95, 1.27, and 2.54 cm jet nozzles respectively along with equation (4.13) as developed by Colin and Olivari (1969). Notice the good agreement at the leading edge of the ground vortex, although there is significant scatter in the data for the lateral extent of the ground vortex.

The ground vortex shape data has also been nondimensionalized with velocity ratio for the three different jet nozzle diameters in accordance with equation (4.16). Figures 5.24, 5.25, and 5.26 give results plotted on log-log coordinates along with a line of slope 1/3 to

illustrate the cube root relation. Notice the significant scatter (average of 10%) for some of the velocity ratios, particularly the lower velocity ratios. The points representing lower velocity ratios deviate the greatest amount from the line, perhaps due to blockage. From figures 5.15 through 5.17 it can be seen that the ground vortex shape does seem to be different at higher velocity ratios as mentioned above, implying that perhaps different phenomena dominate in a higher velocity ratio flow field. The two ground vortex shape equations (4.13) and (4.16) have been compared using equation (4.22) which represents (4.16) nondimensionalized with X_{pmax} , in accordance with the procedure described in section 4.4. Figure 5.27 gives the two equations plotted on linear axes. The two curves are very similar, although the shape of equation (4.13) is slightly more blunt and wide laterally than (4.16). The data (figures 5.21 - 5.26) illustrates considerable scatter compared to both equations, illustrating the need for a better analytical model.

Finally, the ground vortex size for the uniform nozzle, turbulence plate nozzle, and annular jet nozzle have been compared for the case of $h/D_{eff} = 5.5$ and $V_{\infty}/V_j = 0.11$ as shown in figure 5.28. The effective diameters have been calculated by the method described in section 4.2 and are given on the graph. The x and y coordinates of the ground vortex have been nondimensionalized using D_{eff} to allow for a consistent comparison of ground vortex shape. Also, the jet velocity, V_{eff} , has been used to match the cross flow-to-jet velocity ratios. The difference between upstream penetration of the ground vortex formed by the turbulence screen and the uniform nozzle is negligible at most x/D_{eff} . This indicates that an increase in the turbulence intensity in the jet flow has little effect on the ground vortex. This is not surprising since the ground vortex flow field is already a highly turbulent flow

field, created by a flow separation. The special annular nozzle configuration yielded the greatest difference in ground vortex size when compared to the uniform nozzle. The ground vortex formed by the annular nozzle has a shape which is very similar to that formed by the standard nozzle, but has a significantly smaller lateral width at all equivalent x/D_{eff} locations. The annular jet out of ground effect has been shown to have a significant change in the decay rate of the jet in the near field (Kuhlman, 1987), which should yield a significantly smaller impingement pressure for the annular jet. This is because the annular nozzle has an increase in entrainment due to the formation of another wake-like shear layer within the jet flow itself, causing an increase in static pressure in the center of the jet, forcing the jet to spread laterally faster than a jet with a uniform jet exit velocity profile. This significant reduction in ground vortex size for the annular jet may also be influenced by greater relative entrainment in the jet shear layer, which has an increased perimeter relative to the effective diameter, when compared to the uniform jet. This reduced ground vortex size for the nonuniform jet may be of practical significance in reducing hot gas reingestion, so long as there is no increase in suck down pressure due to the increased entrainment. In addition, the present work has not investigated any possible adverse effects due to base drag on the centerbody.

In an effort to study the consistency of the present method for comparing non-uniform jet results to uniform jet data, three different methods for calculating effective diameter have been considered. Table 5.2 gives the values for D_{eff} and V_{eff} as calculated by the three methods described in section 4.3 for the 1.27 cm annular jet nozzle and the 1.27 cm uniform jet nozzle with 2 diameters nozzle length. Notice that all values have little difference for the

uniform jet. Figure 5.29 illustrates a nondimensional comparison of the ground vortex formed by the annular nozzle for h/D_{eff} equal to 6 and a velocity ratio of 0.1 using the results of these three different methods to determine annular jet effective diameter and effective velocity, and hence the different experimental settings (ie. cross flow velocity; jet exit spacing). Also shown are the corresponding results for the standard uniform velocity nozzle. Notice that the method used in the present study (method 1) and the method originally developed by Ziegler and Wooler (method 2) have good nondimensional agreement, although as Table 5.2 illustrates, the numerical values for D_{eff} and V_{eff} are quite different for methods 1 and 2. This is reassuring since the present work employs the method of Kuhlman and Warcup (1978), which is simply a rearrangement of Ziegler and Wooler's original method using the maximum dynamic pressure (q_{max}) to compute the effective momentum flux, from which effective diameter and velocity are computed, while Ziegler and Wooler's original method uses measured momentum flux to compute an effective dynamic pressure, and from that value calculates effective diameter and velocity. Notice also that the method of direct calculation (method 3) has very poor agreement with the other two methods, significantly understating the size of the ground vortex. This is because method 3 is not self-consistent and does not consider the uniform jet to have been accelerated from the same stagnation conditions as the actual non-uniform jet. For this reason, method three has not been used in the present study for comparing the annular jet results with the uniform jet data. Also, the fact that relatively good agreement between the measured ground vortex size which was obtained using the first two techniques in spite of significantly different calculated effective diameter and velocity gives confidence that the present comparison method is reasonable, and

that the present results are reliable.

As a check on the consistency of the annular jet data, the possibility of forcing the non-uniform jet data to collapse on the uniform jet data by selecting a D_{eff} which allows for nondimensional agreement was examined. The data in figure 5.28 has been used to determine that the effective diameter would need to be 0.642 cm to allow for nondimensional agreement between the uniform and annular jets. This D_{eff} is approximately 63% as large as the calculated effective diameter, corresponding to an effective area only 40% as large as the calculated effective area. Using equation (4.9), this corresponds to an effective velocity of 232.65 m/s, or a velocity 2.5 times greater than the measured maximum velocity of the annular jet. This results in a velocity ratio only 40% as large as the uniform jet value, for the same size ground vortex. This illustrates that the significant difference in the ground vortex size of the annular jet is not merely a simple matter of choosing a different scaling parameter or nondimensionalization. The flow field is significantly different as a result of the different near field flow of the annular jet as compared to the uniform jet.

Many of the experiments performed to obtain the flow visualization data presented herein have been performed more than once and compared in an attempt to determine the magnitude of any random error associated with the data taking process, and to obtain an overall view of repeatability, especially in resetting the cross flow velocity. Figures 5.30 through 5.36 illustrate examples of data repeated on different dates and plotted on the same axes. Figures 5.30, 5.31, and 5.32 represent the repeatability of the ground vortex size and shape for different velocity ratios at h/D equal to 3. Good repeatability is evident for this data sequence with percent differences ranging from 0.5 to 3 percent. Figures 5.33 through

5.36 illustrate the repeatability of the data giving ground vortex size and shape for different ground board spacings (Z_b/D). A greater percent difference in repeatability can be seen for this data sequence (1 to 7 percent). This level of repeatability is more representative of the largest percent variation in the repeatability of other data sequences not presented herein.

5.3 LV Measurements

A vector plot of the LV measurements for the uniform jet at h/D_{eff} equal to 5.5 and $V_\infty/V_j = 0.11$, made on the ground vortex centerline, has been presented in figure 5.37. This case corresponds to the uniform jet configuration compared to the annular jet in figure 5.28. The measurement field is from -200 mm to -40 mm (from 16 to 3.2 diameters) upstream of the jet axis with each vertical traverse (z direction) being 20 mm apart (1.6 diameters). Each vertical traverse was from approximately 0.4 diameters above the ground plane to approximately 6.8 diameters above the ground plane. The cross flow has good uniformity at -200 mm upstream, which is upstream of the ground vortex. The slower velocity at the z location closest to the ground plane is the result of the boundary layer forming on the ground plane. The upstream edge of the ground vortex is located approximately 8 diameters upstream (100 mm) which agrees well with the flow visualization results presented in figure 5.28, although significant deflection of the flow in the z direction can be seen at 11.2 diameters upstream (140 mm). Although measurements were obtained significantly close to the ground plane, no reverse flow was evident in this data set. This is most likely due to the lack of seeding in the jet. When seed particles were injected into the

blower inlet no Doppler signals could be detected in front of the jet exit, apparently because the seed particles coated the blower housing and impeller. Since the reverse flow associated with the ground vortex is largely jet flow (ie, a wall jet), data rates were very low in the wall jet region. Also, these measurements which were obtained very likely might not be representative of the unseeded wall jet velocities. Measurements closer to the ground plane than 0.4 diameters could not be obtained due to the glare caused by the laser beams passing through the glass. Also, measurements could not be obtained directly in front of the jet (at $x=0$), again because of problems with reflections off of the jet nozzle. It was found possible to get around these problems with flare, by swapping the PMT optics for the one-channel and two-channel optics. However, this resulted in significantly lower data rates and noisier Doppler burst signals.

Measured turbulence intensities range from about 2% in the freestream to 70% at or around the ground vortex and are given by the shading in figure 5.37. This free stream turbulence intensity agrees well with other tunnel data, although LV data cannot distinguish turbulence intensities less than 1.0% accurately, due to signal broadening inherent in the system. Also, one of the counter processors used in this work had inherently more noise than the other two counter processors. Post processing of the data helped eliminate some of this spurious noise, but the RMS velocities were more sensitive to the histogram truncations and consequently would have more inherent error. Figure 5.37 indicates that the ground vortex forming at $y = 0$ has very little vortical structure and is probably better described as a separation bubble. The known sensitivity of separation regions in other flow fields probably gives the best insight into the unsteadiness of the ground vortex. It is most likely

the streamwise fluctuation of the separation point location due to small jet or free stream flow field changes that causes the unsteadiness that is observed with ground vortex formation.

A more clearly vortical structure was observed in the laser light sheet flow visualization of cross flow plane (y z plane) cuts through the ground vortex downstream of the jet impingement location (leg of the ground vortex). Figure 5.38 shows the LV measurements made in the ground vortex leg (in a yz plane) at x/D_{eff} equal to 8.00 downstream of the jet, which shows a more clearly defined vortex. Unfortunately, the measurement grid selected was too coarse to determine the shape of the ground vortex leg accurately. Measured vortex mean velocities in this cross flow plane are only about 25 percent of the axial velocity. Figure 5.39 is a plot of the velocity vectors presented in figure 5.38 on a uniform interpolated grid in an attempt to get a better definition of the ground vortex. This vortex appears to have a center which is located approximately 10 diameters from the centerline of the ground vortex. The half width of the ground vortex appeared to be about 12 to 14 diameters, which is in close agreement with the half width observed with the flow visualization (figure 5.28). Again, very little jet flow is seen near the ground plane traveling away from the centerline, even though it is very likely that the ground vortex leg largely consists of jet flow. This is evident by the large quantities of smoke injected via the jet flow, which was seen in the ground vortex leg in the flow visualization studies. This lack of a visible jet flow could again be due to lack of seeding in the jet. The shaded contours in figure 5.39 give the streamwise component of velocity which tends to be small in high recirculation regions. This is typical of three dimensional burst vortex flows. The shading

in figure 5.40 gives the turbulence intensities measured in the ground vortex leg, which were on the order of 40 to 80 percent for the ground vortex leg flow close to the ground plane, while most of the vortex flow at the top of the vortex leg had turbulence intensities of approximately 5 to 10 percent. This gives evidence that even as far down stream as 8 diameters, the ground vortex is still readily entraining low turbulence intensity air from the freestream. The turbulence intensities at the outer edge of the vortex leg ($y/D_{\text{eff}} = 16$) were as low as 4%. Graphs of velocity magnitude of each of the mean velocity components for the present data sets have been given in Appendix E.

Table 5.1: Table of calibration results for the eight nozzles utilized in the present study.

NOZZLE TYPE	P_{noz} (cm H ₂ O)	Q_{max} (cm H ₂ O)	V_{max} (m/s)	Q_{noz} (CMM)	MF_{noz} (N)	V_{avo} (m/s)	D_{eff} (cm)	V_{eff} (m/s)
1.27 cm 2D noz	v	49.45	91.91	0.6823	1.193	89.78	1.251	92.55
	h	49.50	92.08	0.6878	1.200	90.50	1.255	92.72
	a	49.48	91.99	0.6851	1.197	90.14	1.253	92.63
2.54 cm 2D noz	v	48.69	91.38	2.752	4.767	90.51	2.519	92.01
	h	48.46	91.28	2.726	4.681	89.72	2.510	91.91
	a	48.58	91.33	2.740	4.724	90.11	2.514	91.96
0.95 cm 2D noz	v	49.50	92.13	0.3855	0.6730	90.17	0.9390	92.78
	h	49.63	92.22	0.3852	0.6720	90.10	0.9382	92.87
	a	49.57	92.18	0.3854	0.6725	90.14	0.9386	92.83
1.27 cm screen	v	49.99	92.43	0.6927	1.214	91.14	1.257	93.08
	h	49.99	92.43	0.6839	1.198	89.98	1.247	93.08
	a	49.99	92.43	0.6883	1.206	90.56	1.253	93.08
1.27 cm annular	v	48.51	91.32	0.4384	0.6227	57.68	1.006	91.94
	h	49.73	92.52	0.4502	0.6493	59.24	1.013	93.17
	a	49.12	91.92	0.4443	0.6360	58.46	1.009	92.56
1.27 cm 4D noz	v	49.05	92.13	0.6834	1.141	89.91	1.250	92.77
	h	49.68	92.75	0.6876	1.188	90.47	1.250	93.40
	a	49.37	92.44	0.6855	1.185	90.19	1.250	93.09
0.95 cm 7D noz	v	52.45	94.38	0.3835	0.6826	89.71	0.9252	95.09
	h	53.11	94.82	0.3893	0.6922	91.05	0.9299	95.53
	a	52.78	94.60	0.3864	0.6874	90.38	0.9275	95.31
1.27 cm 13D noz	h	49.25	92.39	0.6774	1.156	89.13	1.243	93.04

v - vertical
h - horizontal
a - average

Table 5.2: Table of effective diameter and velocity calculated by three different methods

NOZZLE TYPE	Present Study		Ziegler & Wooller		Direct Calculation	
	D_{eff} (cm)	V_{eff} (m/s)	D_{eff} (cm)	V_{eff} (m/s)	D_{eff} (cm)	V_{eff} (m/s)
1.27 cm v uniform h 2D noz a	1.255	92.72	1.255	92.66	1.254	92.78
	1.251	92.55	1.251	92.60	1.251	92.50
	1.253	92.63	1.253	92.63	1.253	92.64
1.27 cm v annular h a	1.013	93.17	1.117	76.62	0.9203	112.8
	1.006	91.94	1.111	75.34	0.9125	111.7
	1.009	92.56	1.114	75.98	0.9164	112.3

h - horizontal

v - vertical

a - average

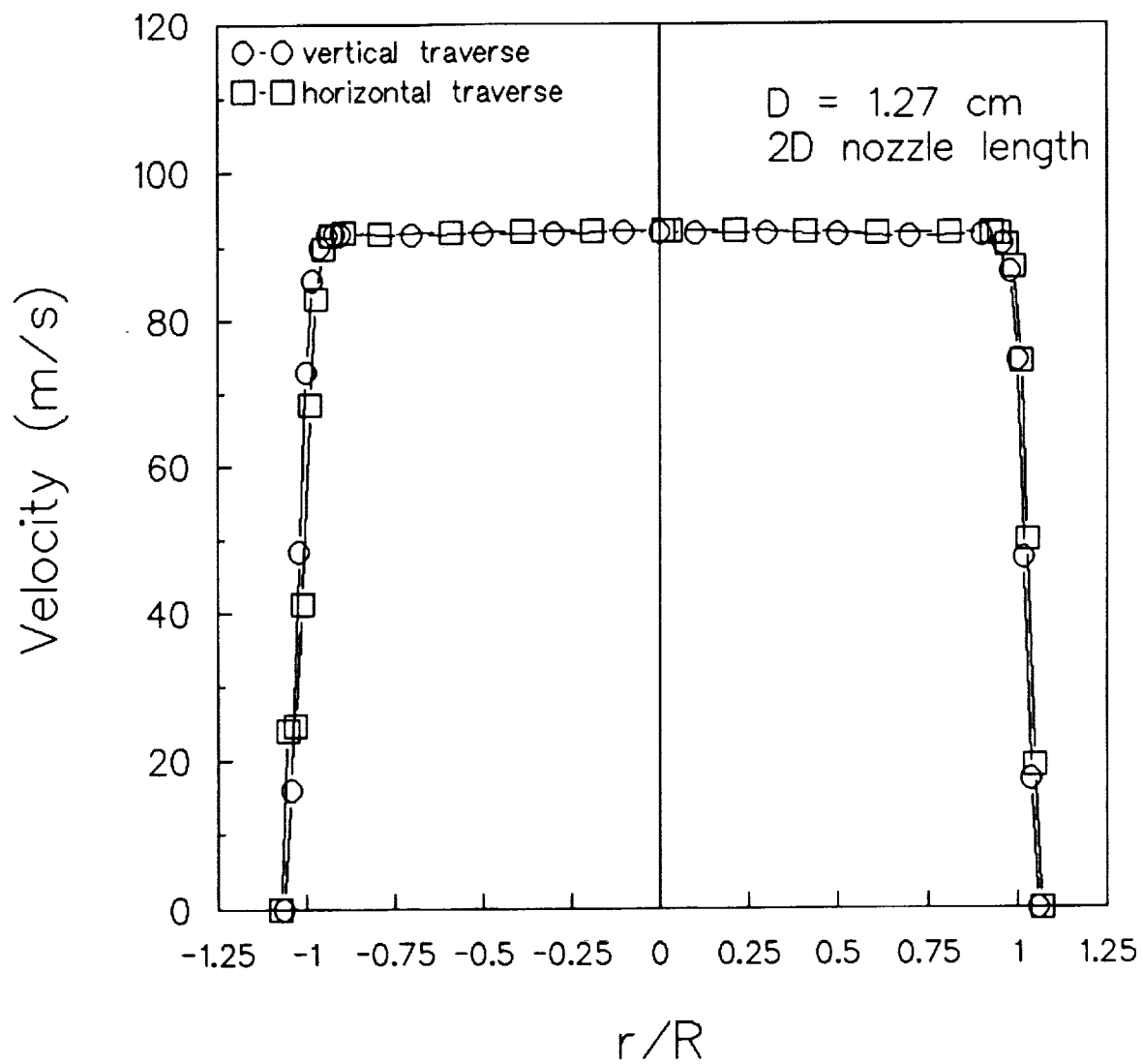


Figure 5.1: Axial velocity profiles obtained by horizontal and vertical traverse for the 1.27 cm diameter nozzle; 2 diameter nozzle length.

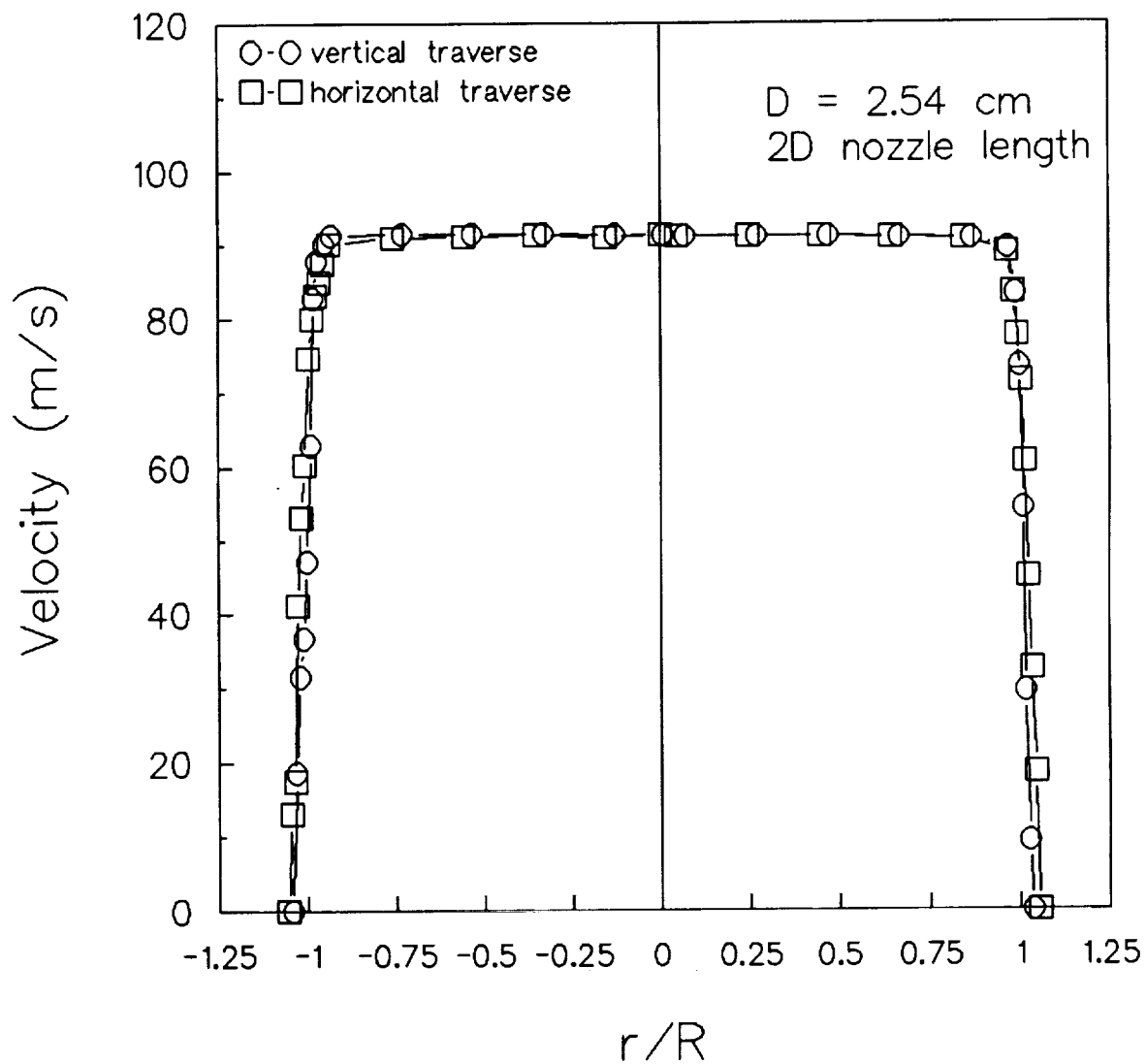


Figure 5.2: Axial velocity profiles obtained by horizontal and vertical traverse for the 2.54 cm diameter nozzle; 2 diameter nozzle length.

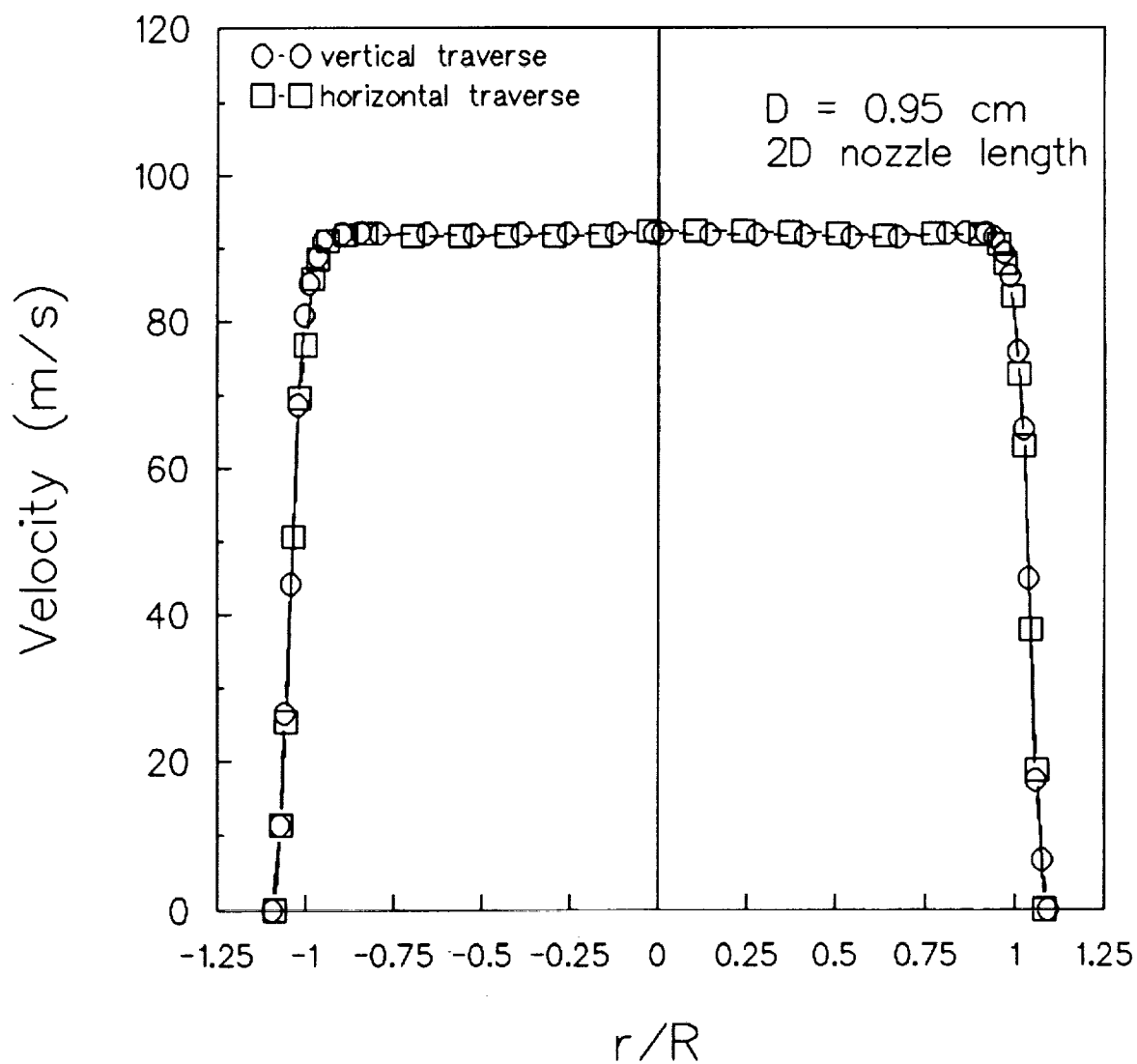


Figure 5.3: Axial velocity profiles obtained by horizontal and vertical traverse for the 0.95 cm diameter nozzle; 2 diameter nozzle length.

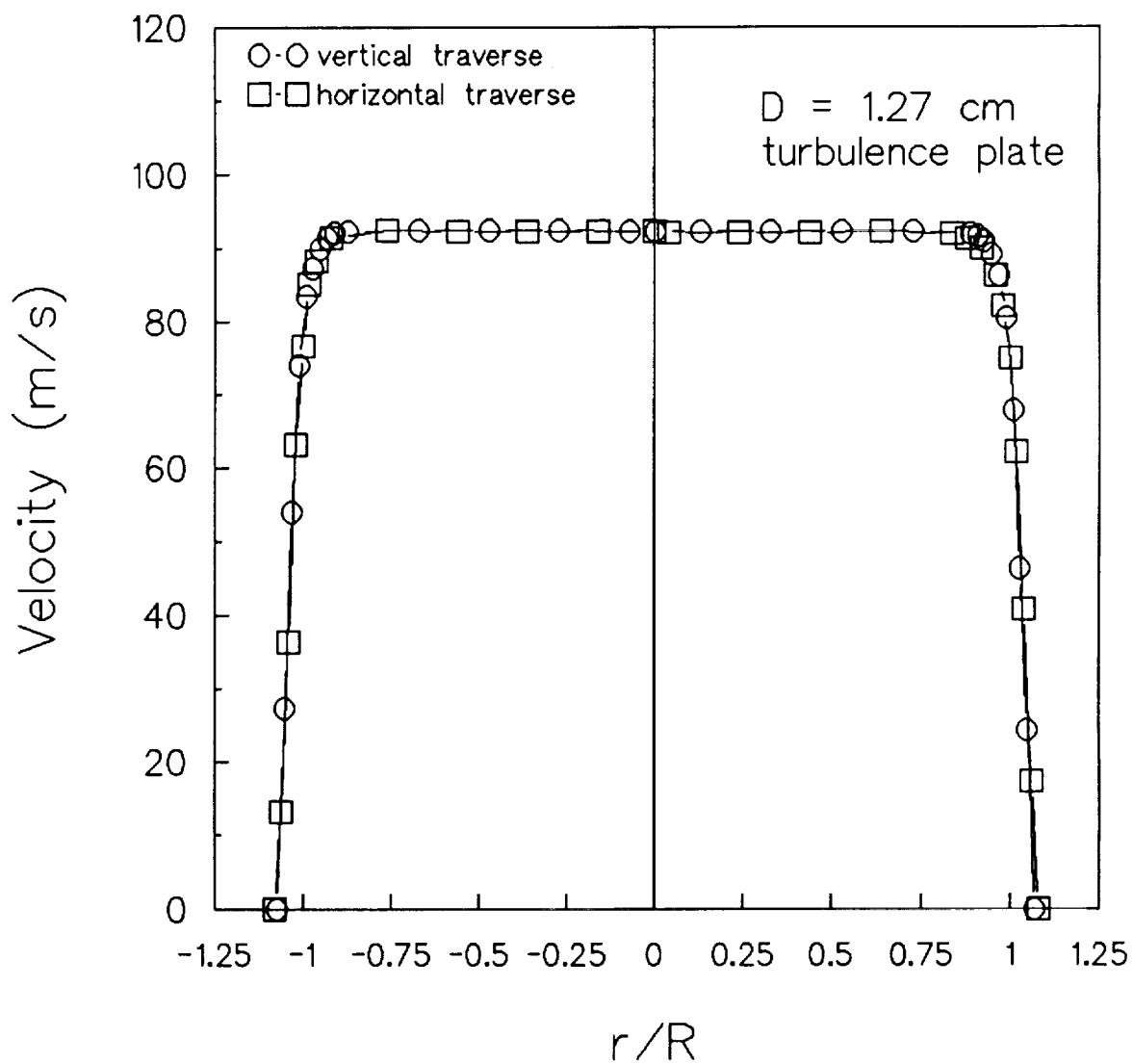


Figure 5.4: Axial velocity profiles obtained by horizontal and vertical traverse for the turbulence generating nozzle; 1.27 cm diameter exit.

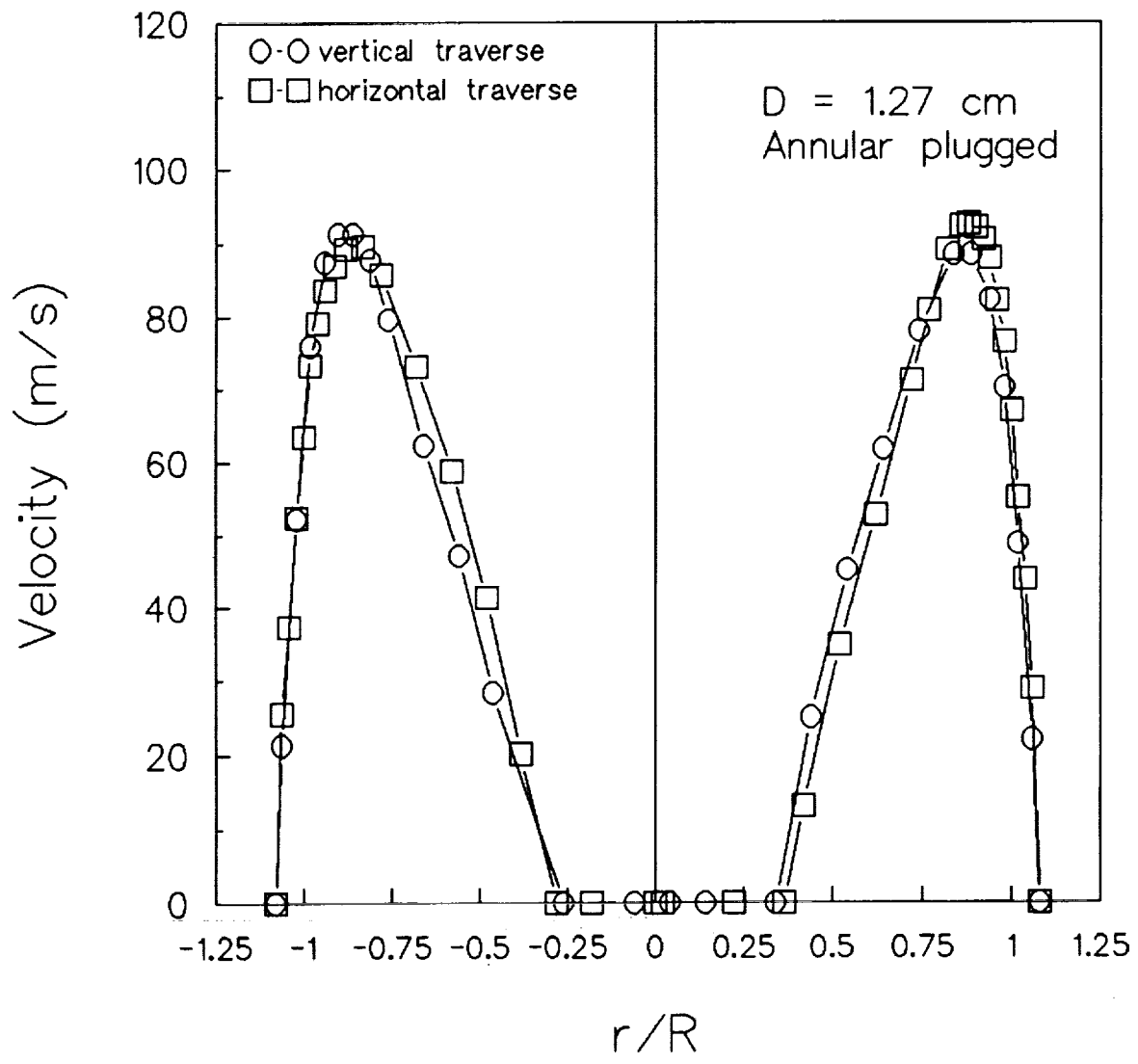
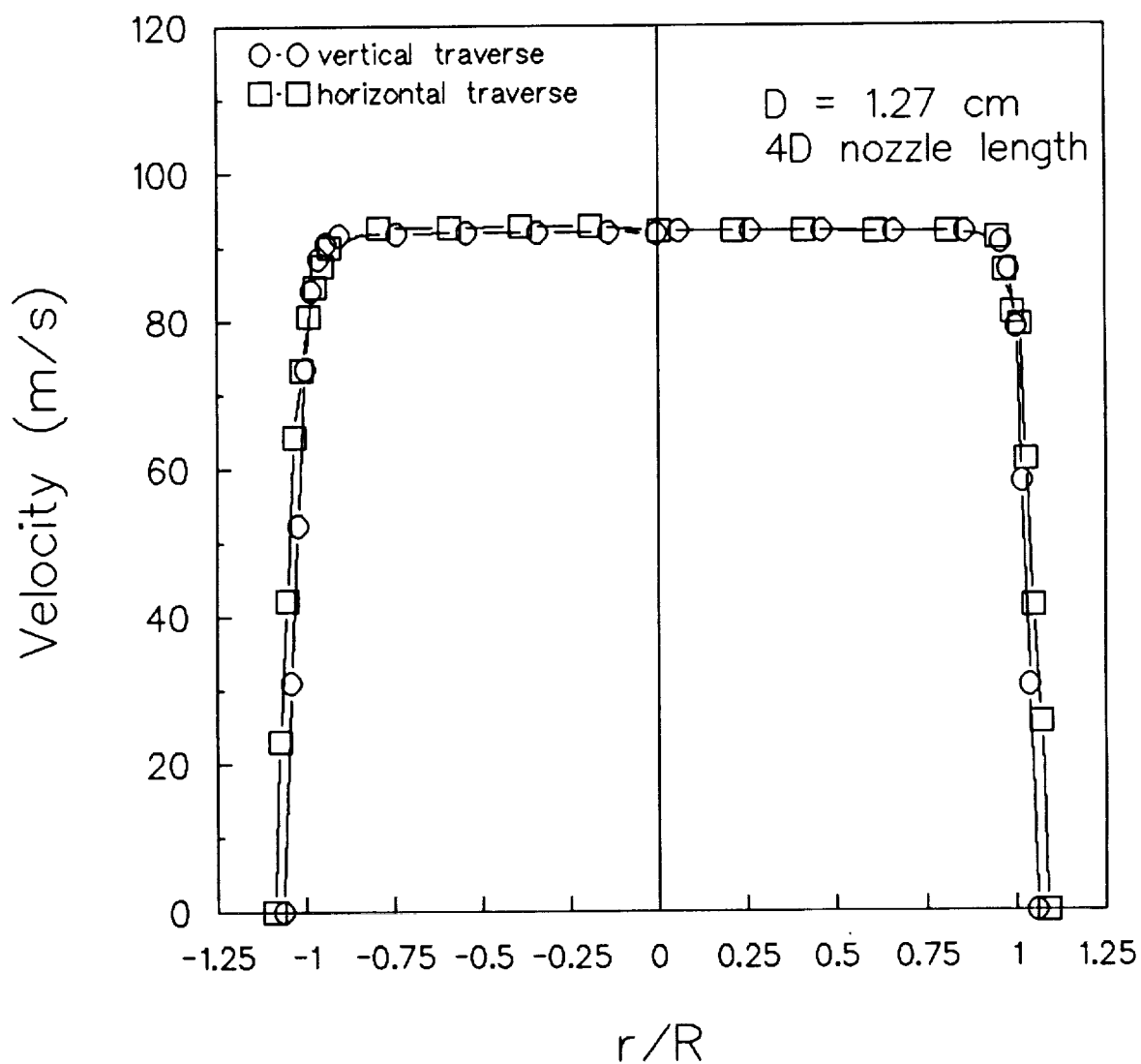


Figure 5.5: Axial velocity profiles obtained by horizontal and vertical traverse for the annular nozzle; 1.27 cm diameter exit.



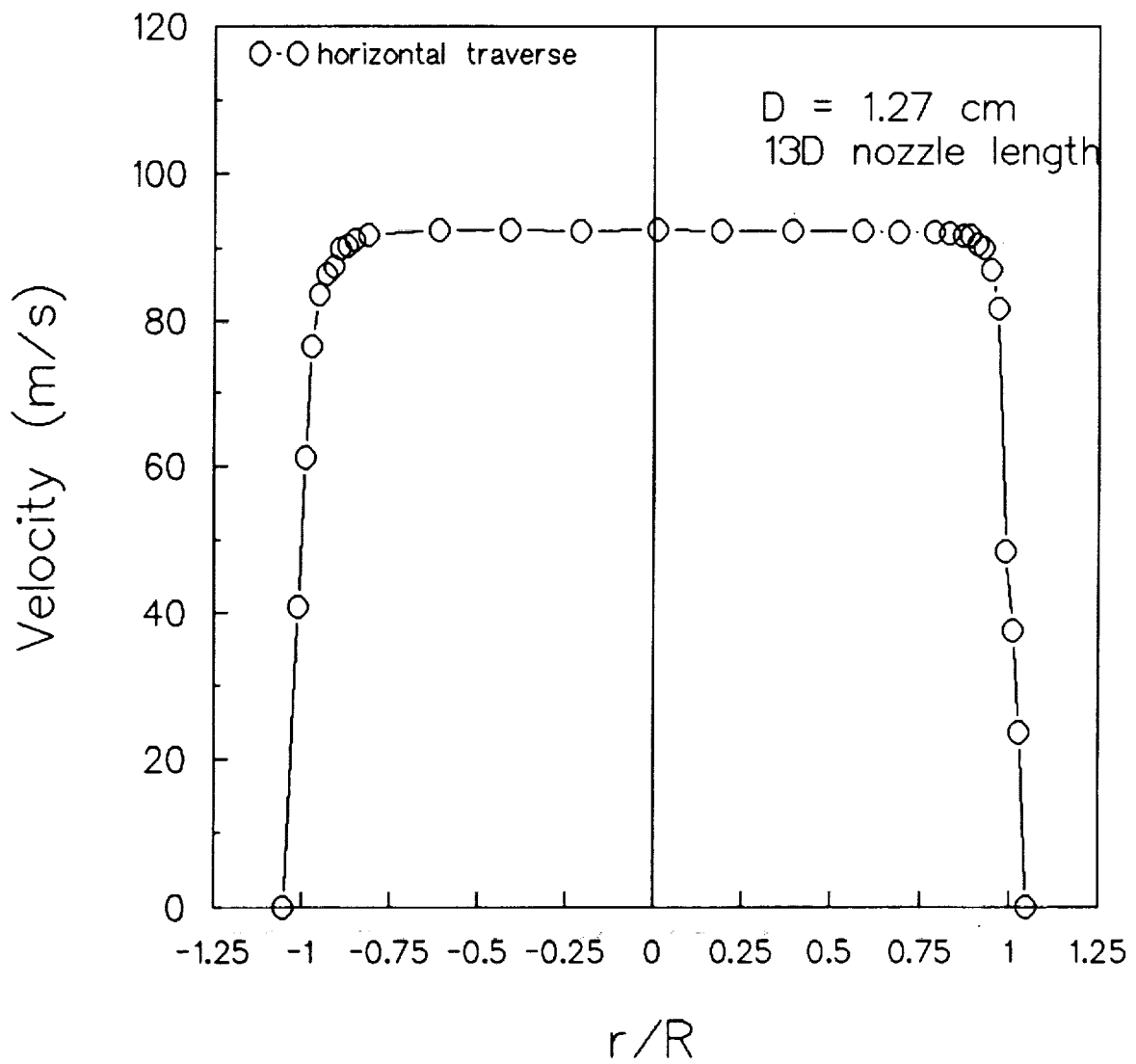


Figure 5.7: Axial velocity profile obtained by horizontal traverse for the 1.27 cm diameter nozzle; 13 diameter nozzle length.

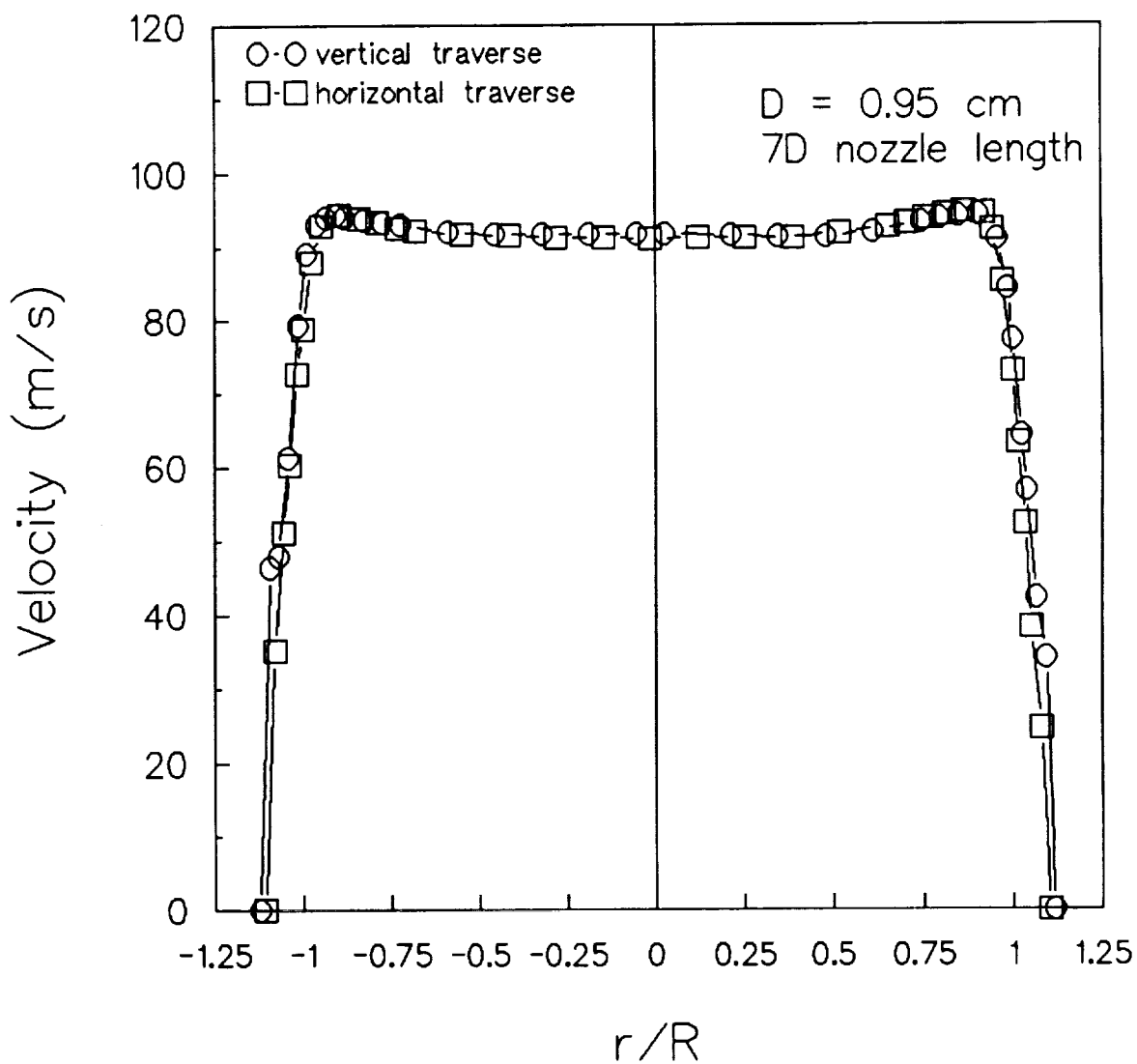


Figure 5.8: Axial velocity profiles obtained by horizontal and vertical traverse for the 0.95 cm diameter nozzle; 7 diameter nozzle length.

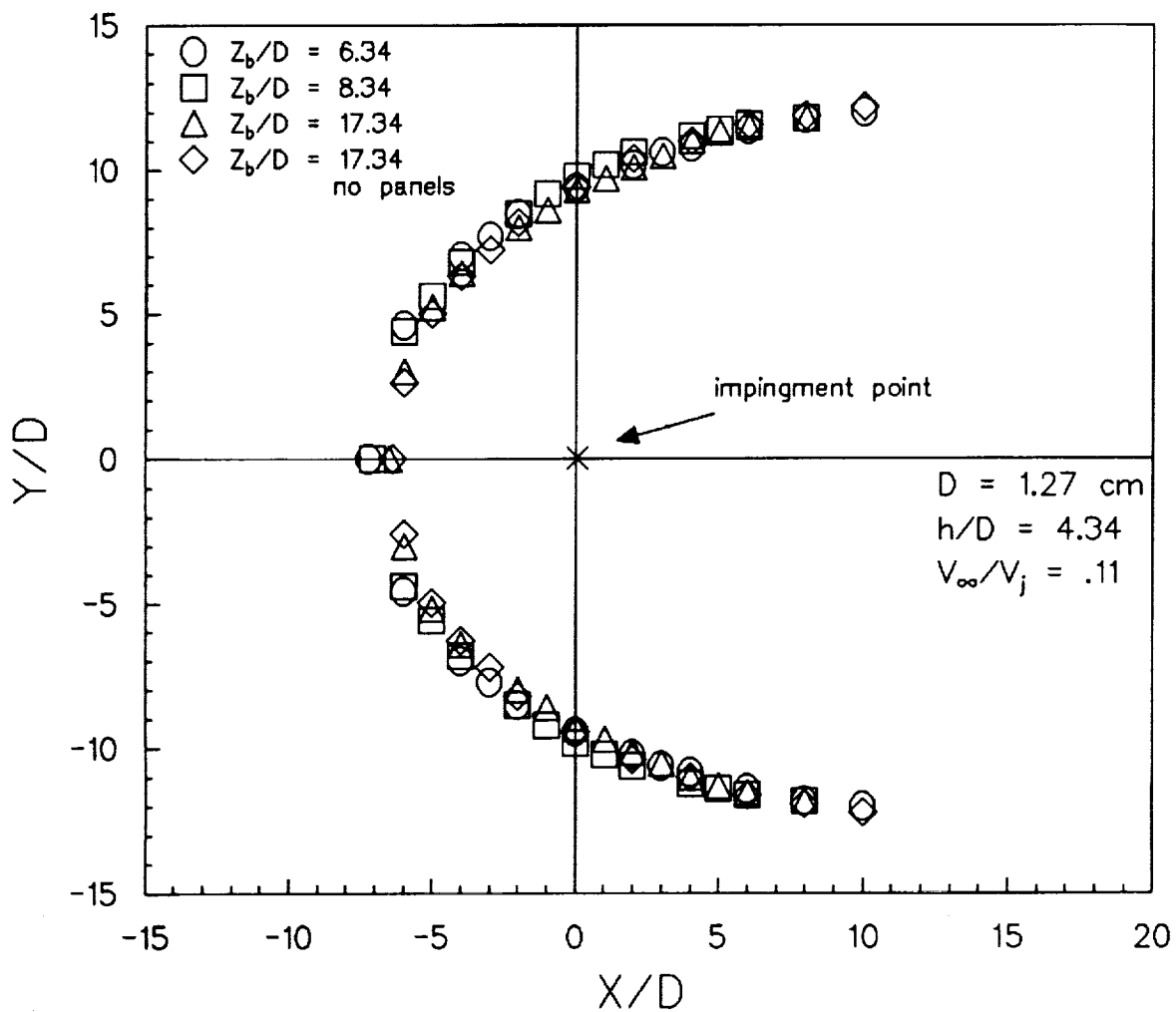


Figure 5.9: Comparison of nondimensional shape of ground vortex for different jet board spacing for h/D equal to 4.34 and V_∞/V_j equal to .11.

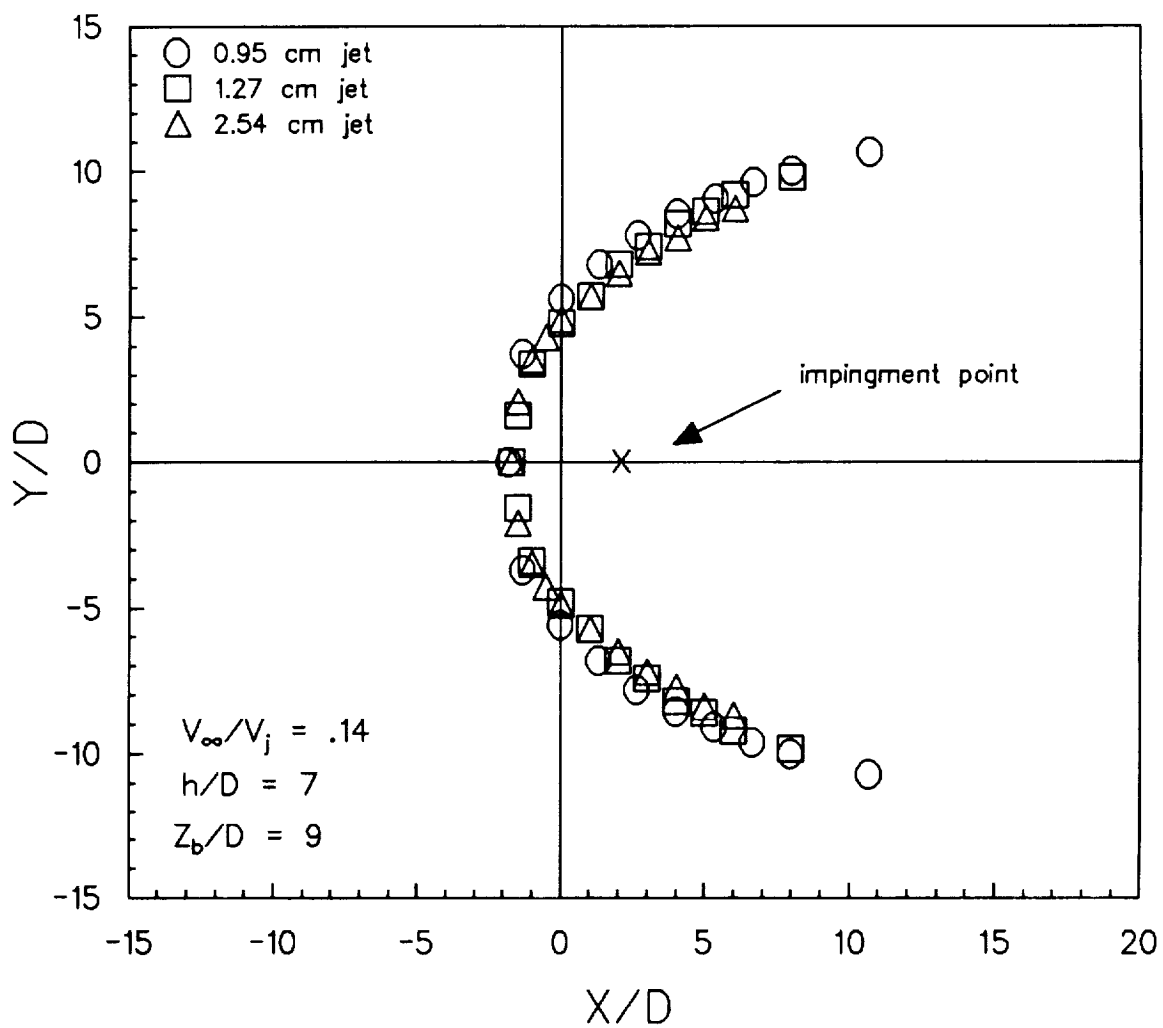


Figure 5.10: Comparison of nondimensional shape of ground vortex for the three different nozzle diameters at h/D equal to 7 and V_{∞}/V_j equal to .14.

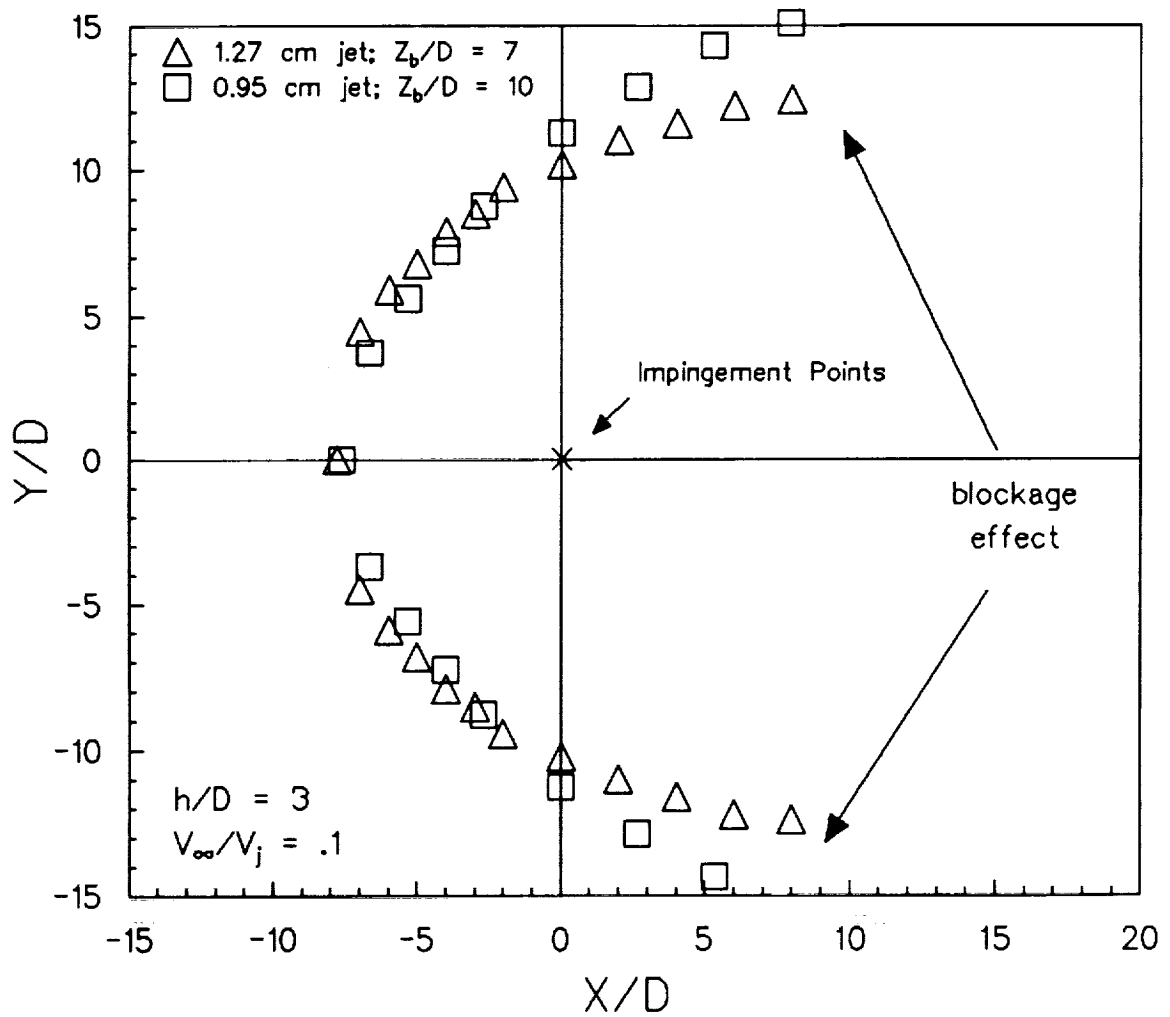


Figure 5.11: Comparison of nondimensional shape of ground vortex for 1.27 and 0.95 cm nozzles for h/D equal to 3 and V_∞/V_j equal to .1.

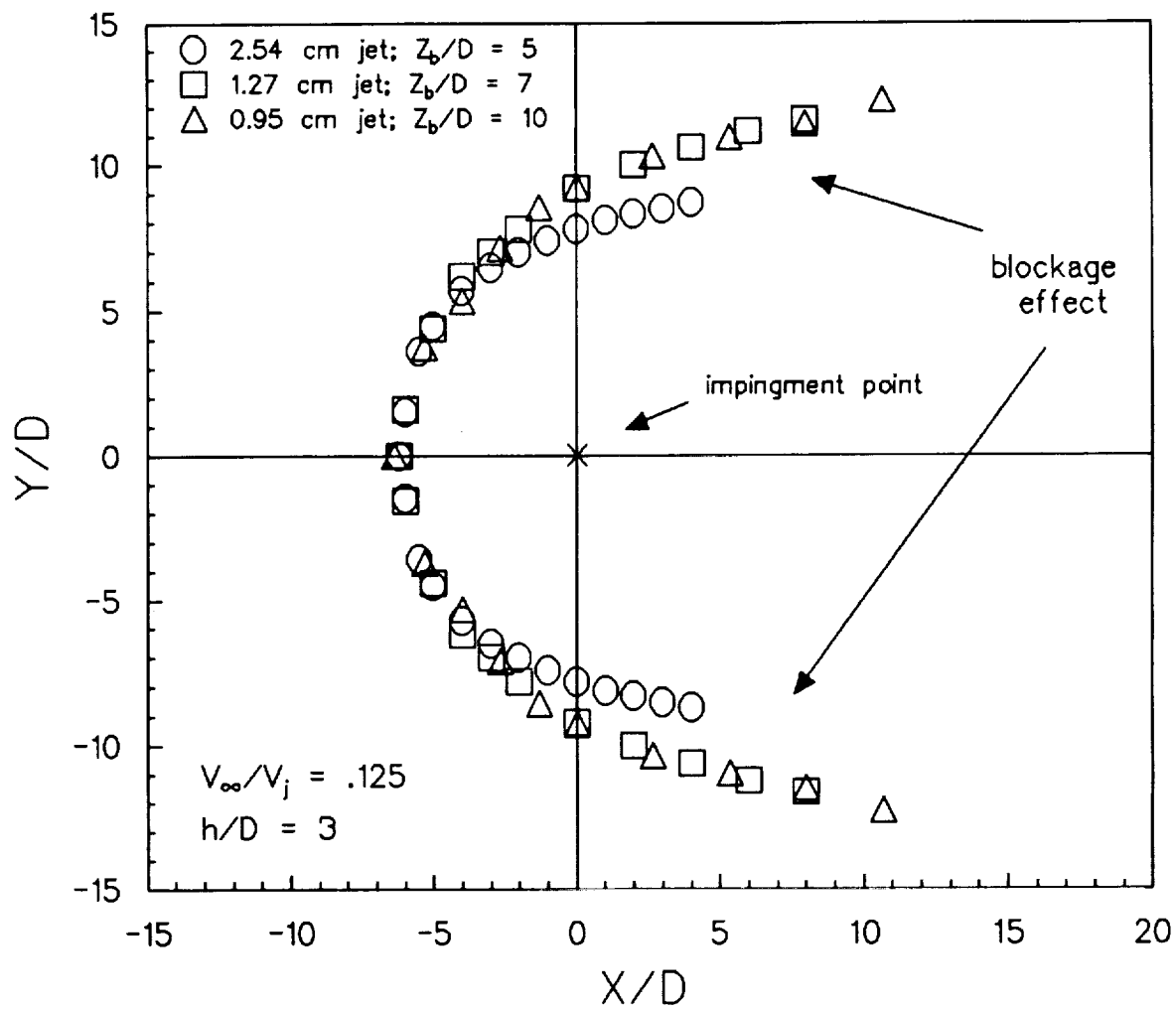


Figure 5.12: Comparison of nondimensional shape of ground vortex for 2.54, 1.27, and 0.95 cm nozzles for h/D equal to 3 and V_∞/V_j equal to .125.

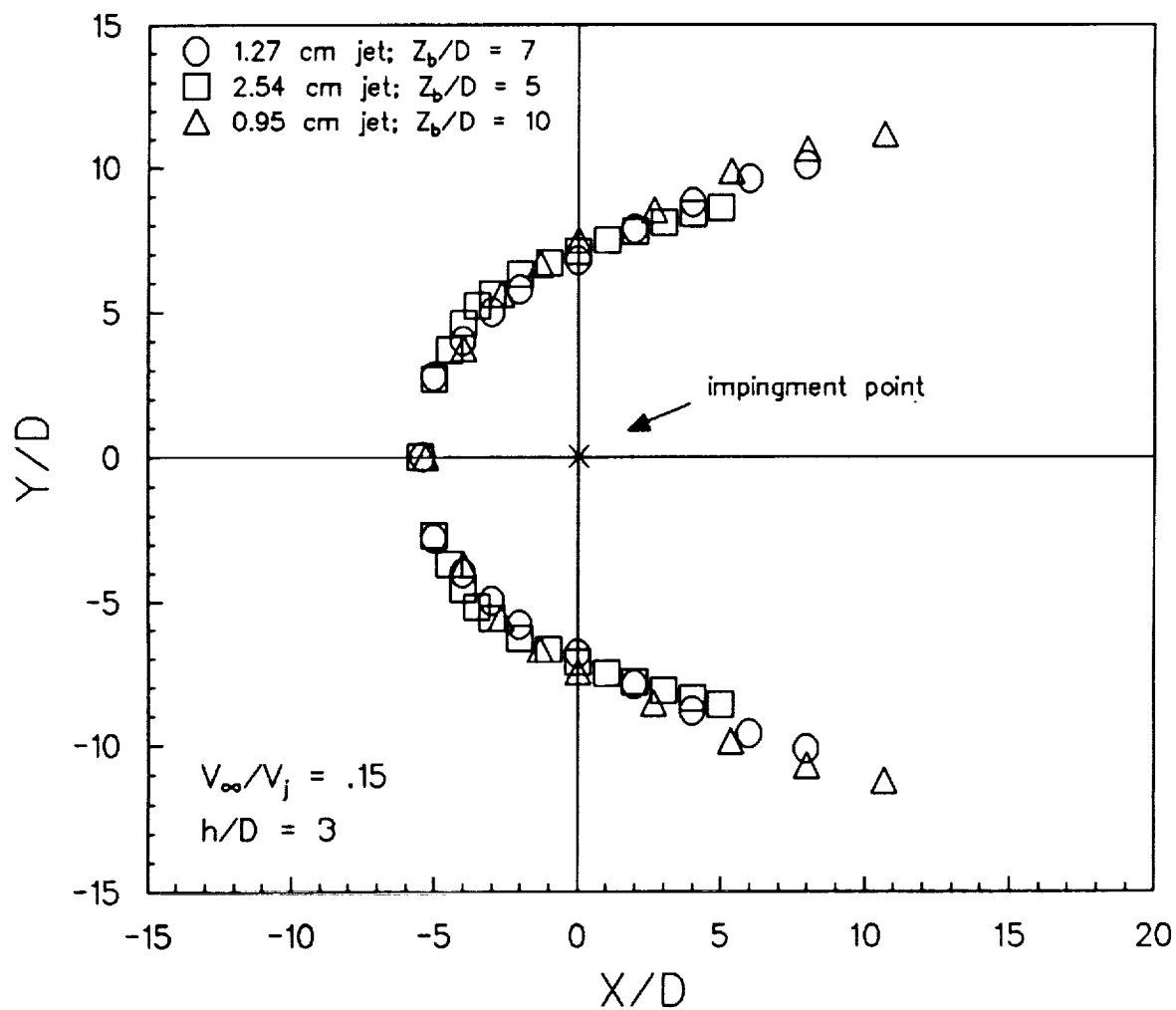


Figure 5.13: Comparison of nondimensional shape of ground vortex for 2.54, 1.27, and 0.95 cm nozzles for h/D equal to 3 and V_∞/V_j equal to .15.

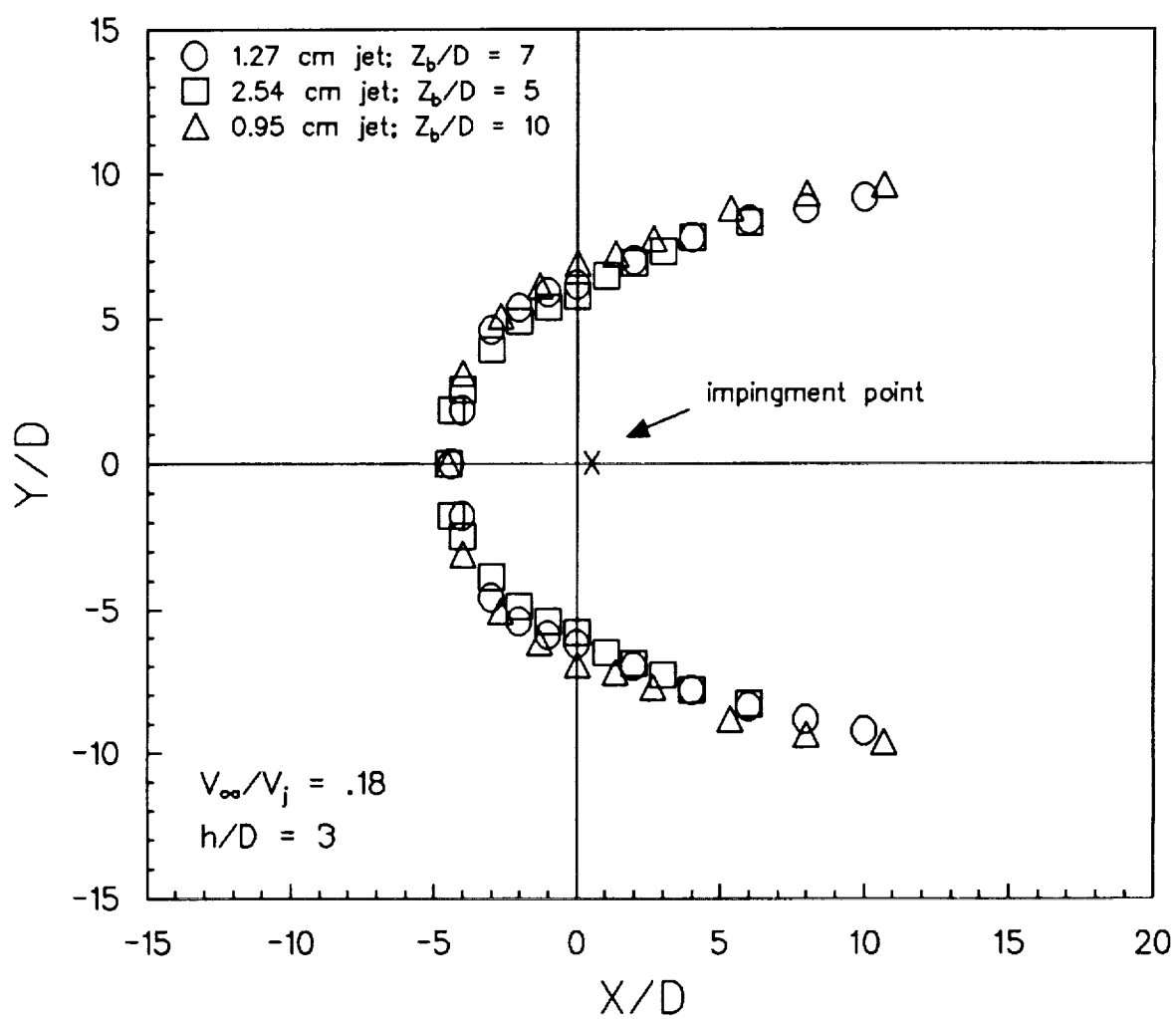


Figure 5.14: Comparison of nondimensional shape of ground vortex for 2.54, 1.27, and 0.95 cm nozzles for h/D equal to 3 and V_∞/V_j equal to .18.

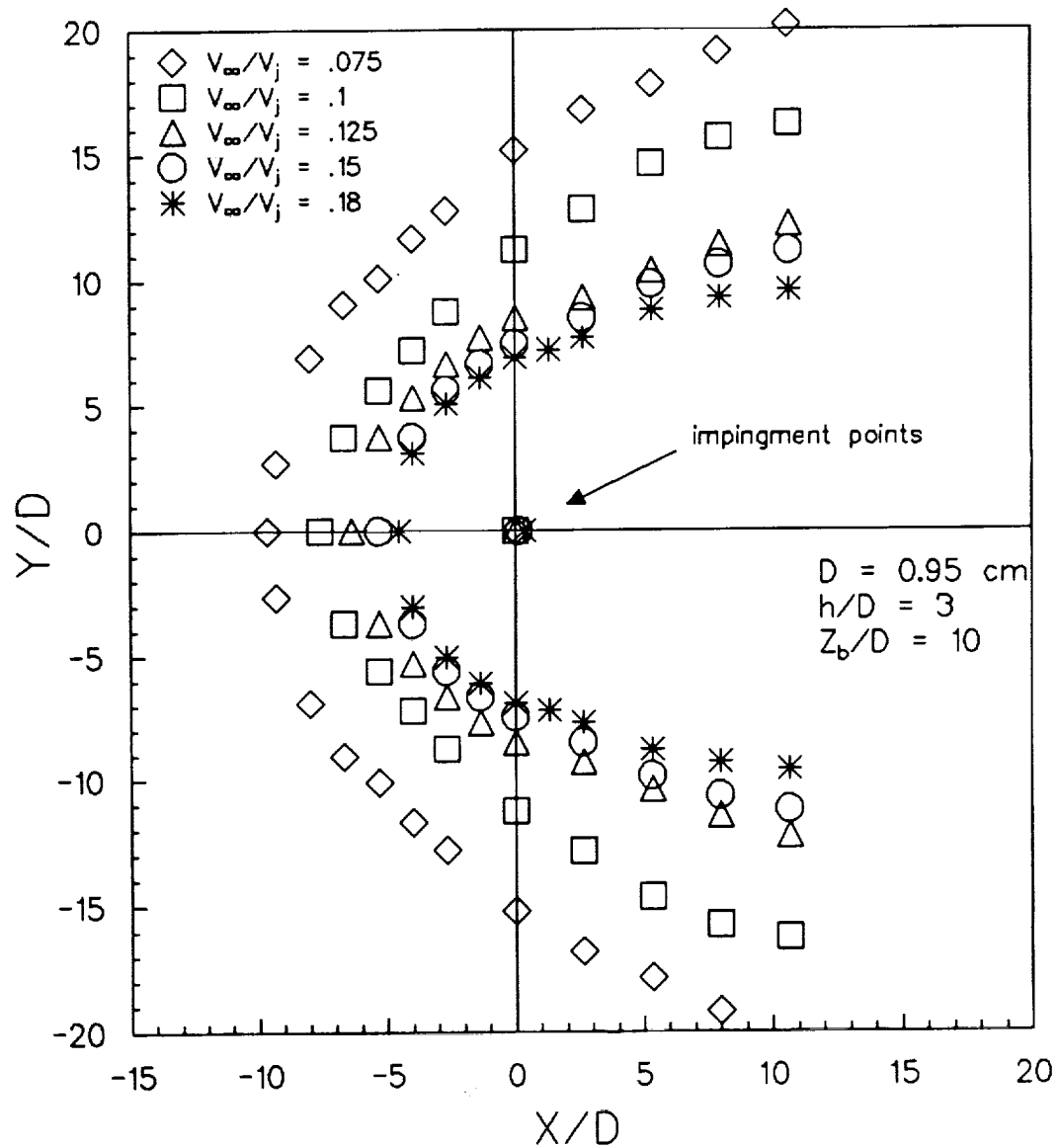


Figure 5.15: Comparison of nondimensional shape of ground vortex for different velocity ratios using the 0.95 cm nozzle; $h/D = 3$; $Z_b/D = 10$.

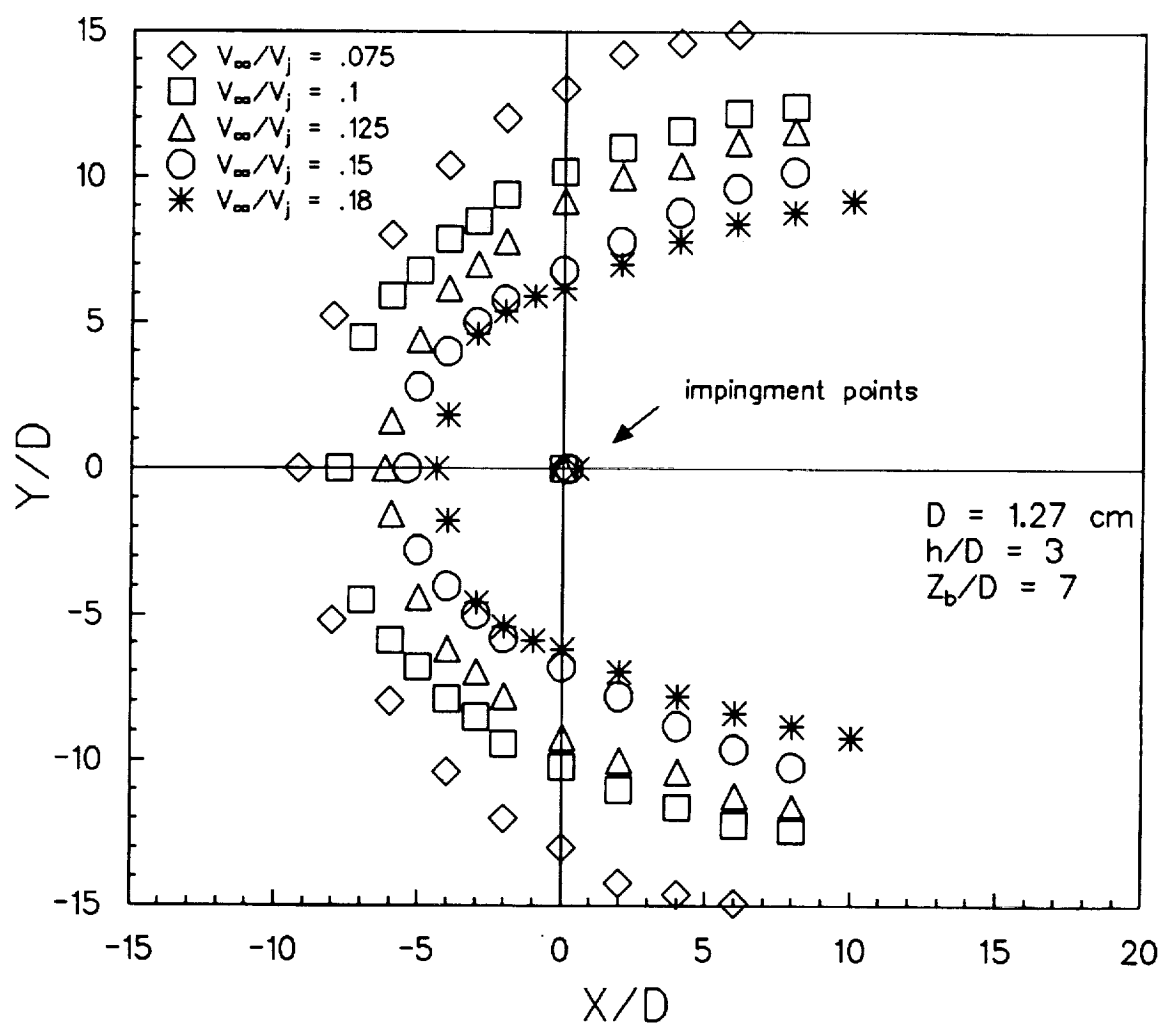


Figure 5.16: Comparison of nondimensional shape of ground vortex for different velocity ratios using the 1.27 cm nozzle; $h/D = 3$; $Z_b/D = 7$.

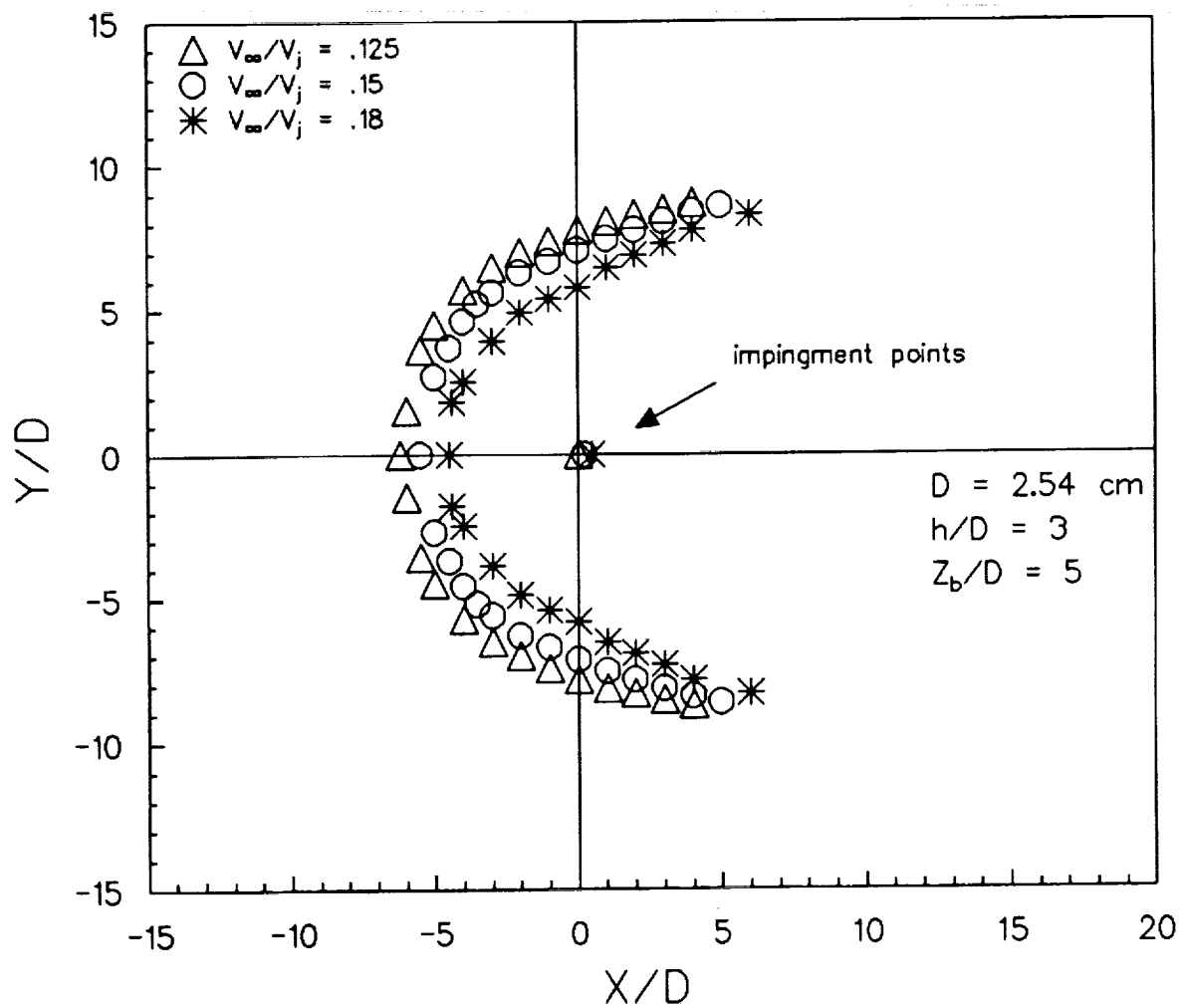


Figure 5.17: Comparison of nondimensional shape of ground vortex for different velocity ratios using the 2.54 cm nozzle; $h/D = 3$; $Z_b/D = 5$.

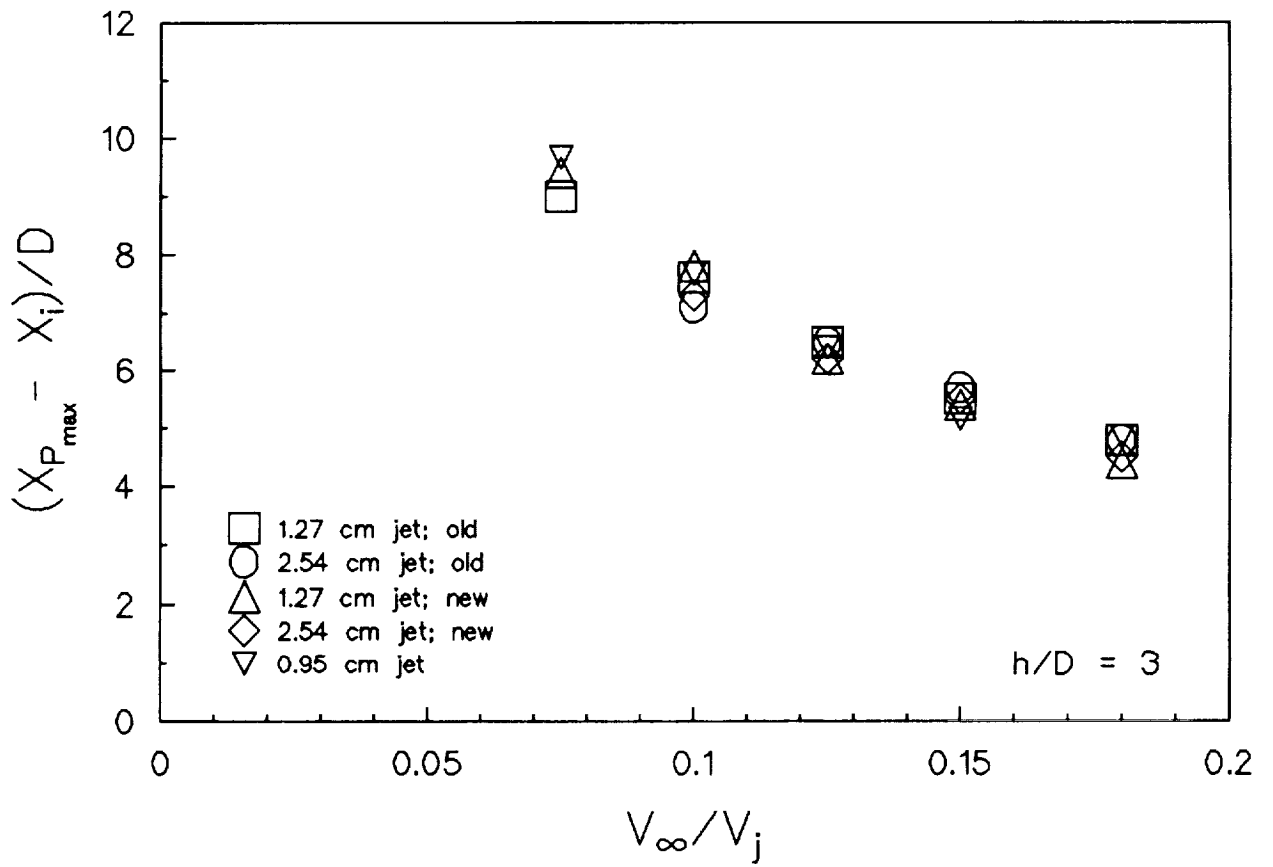


Figure 5.18: Comparison of nondimensional maximum penetration of the ground vortex along centerline for two different data sets taken.

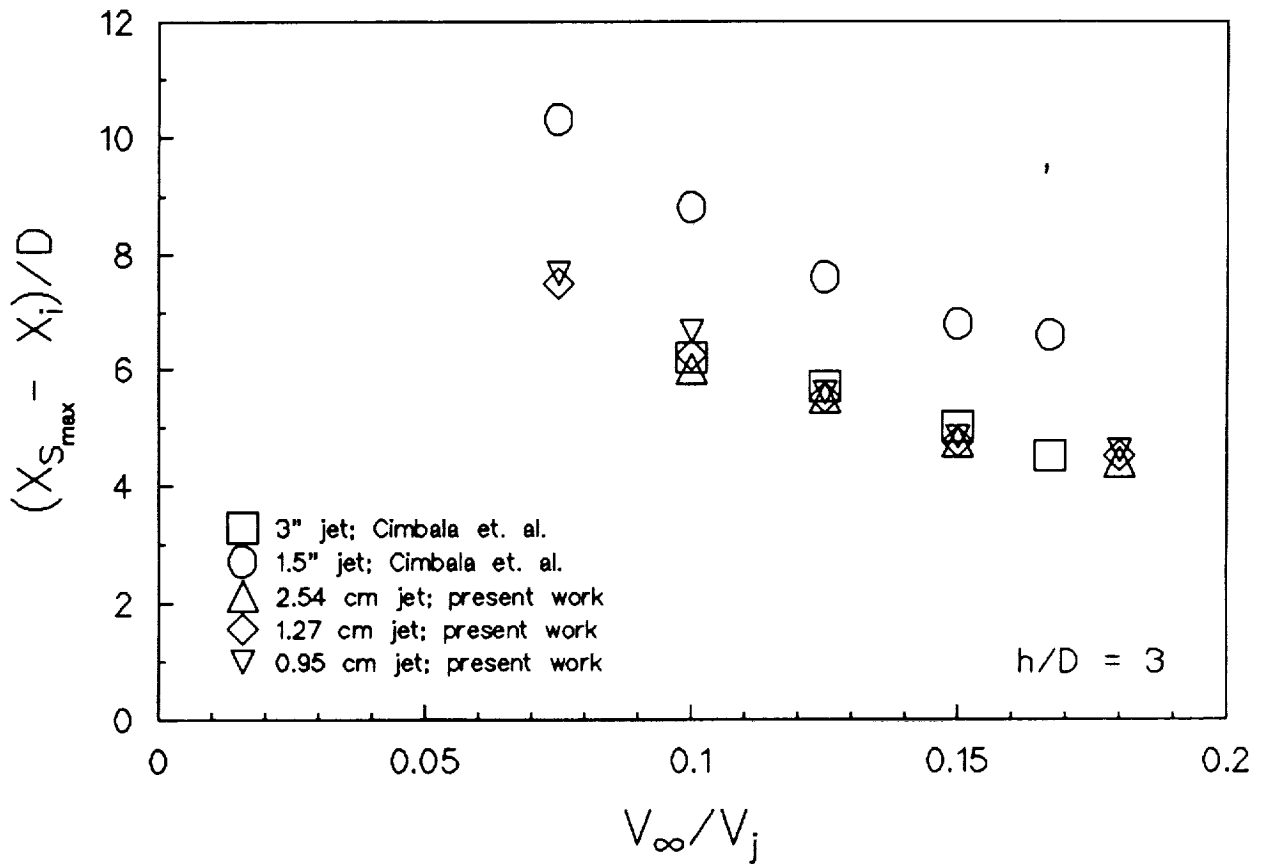


Figure 5.19: Nondimensional ground vortex separation distance versus V_{∞}/V_j along the centerline (maximum).

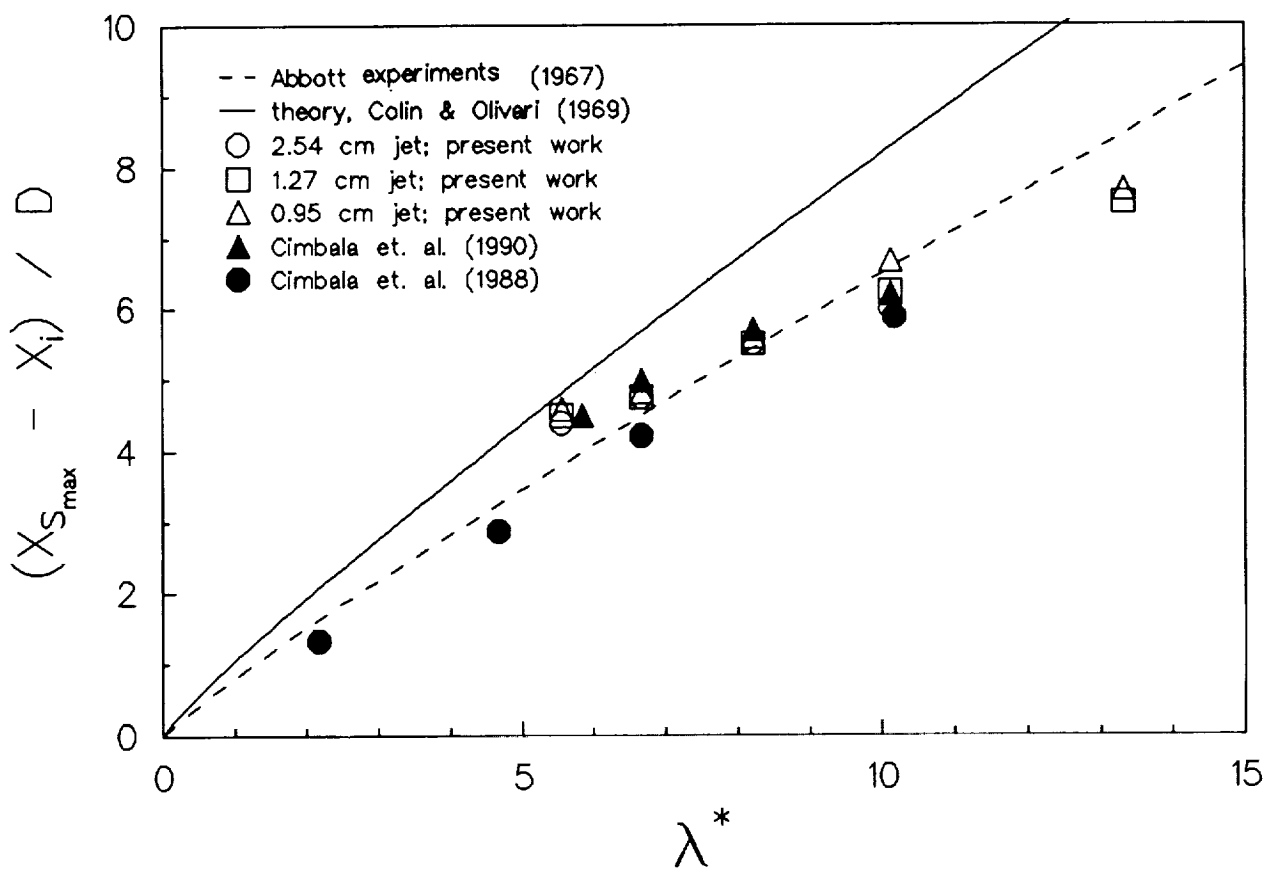


Figure 5.20: Comparison of previous work of the nondimensional ground vortex separation distance versus λ^* along the centerline (maximum).

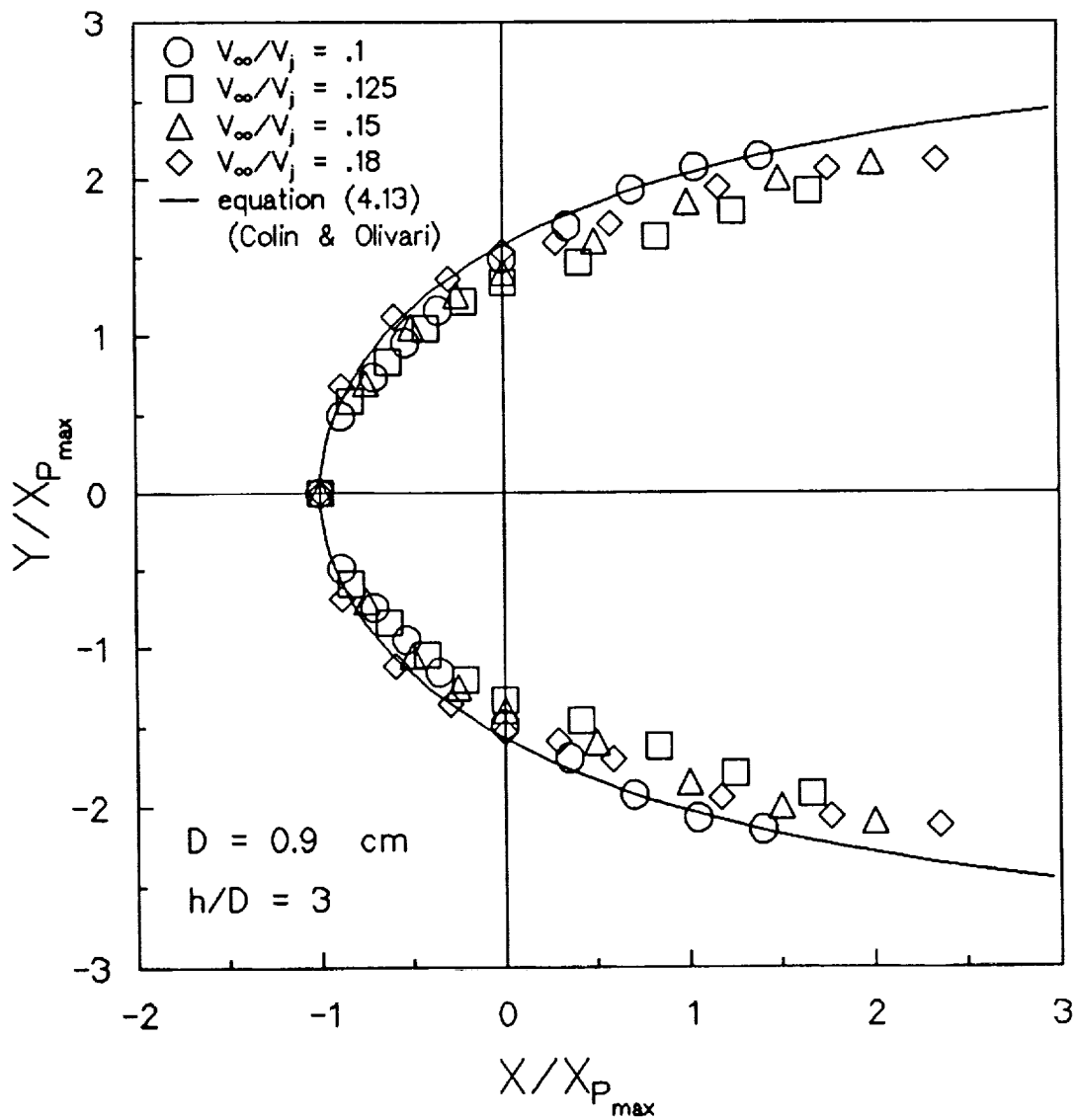


Figure 5.21: Comparison of different velocity ratio data nondimensionalized with X_{Pmax} compared with equation 4.13 for the 0.91 cm jet nozzle.

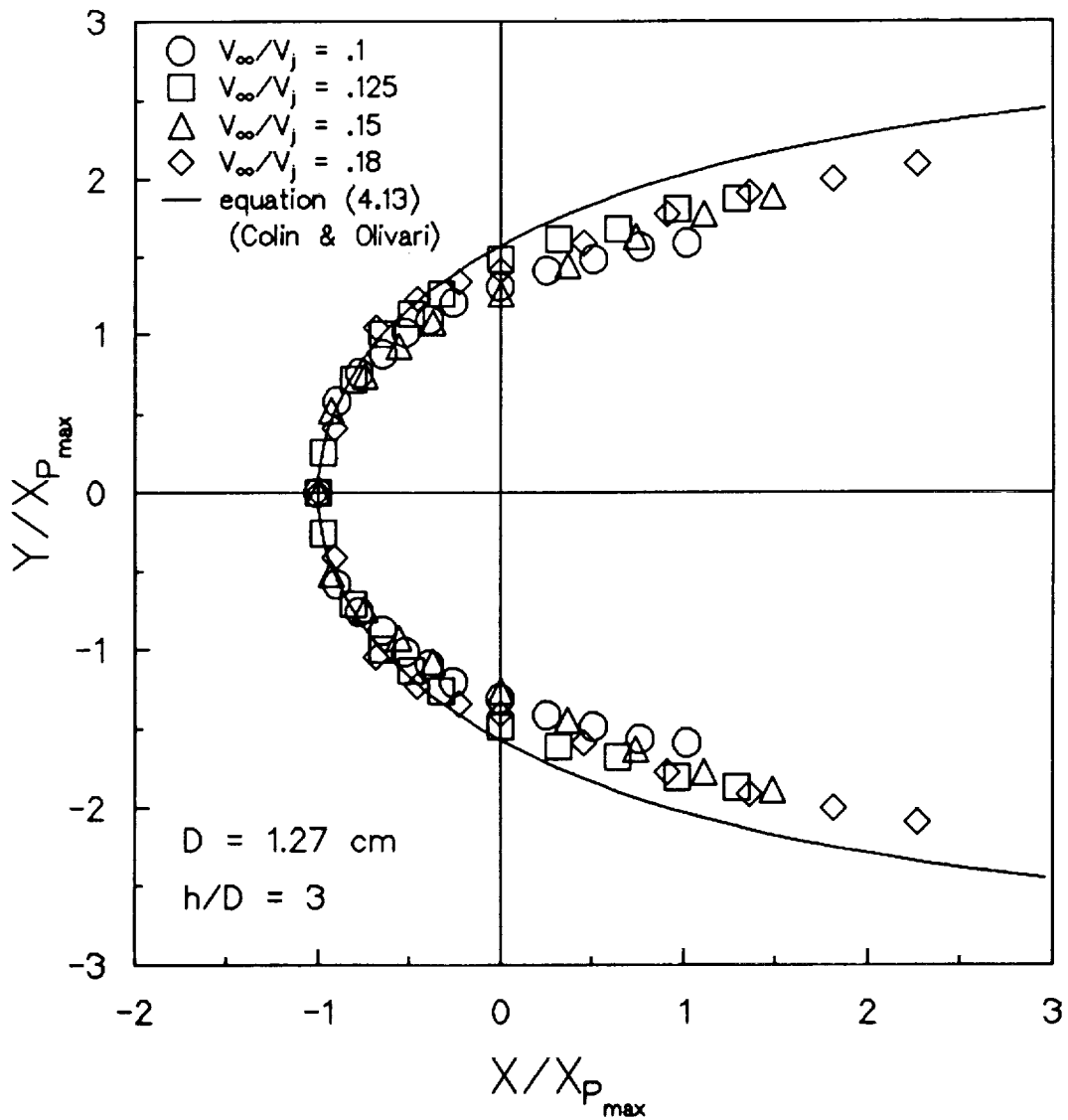


Figure 5.22: Comparison of different velocity ratio data nondimensionalized with $X_{P_{max}}$ compared with equation 4.13 for the 1.27 cm jet nozzle.

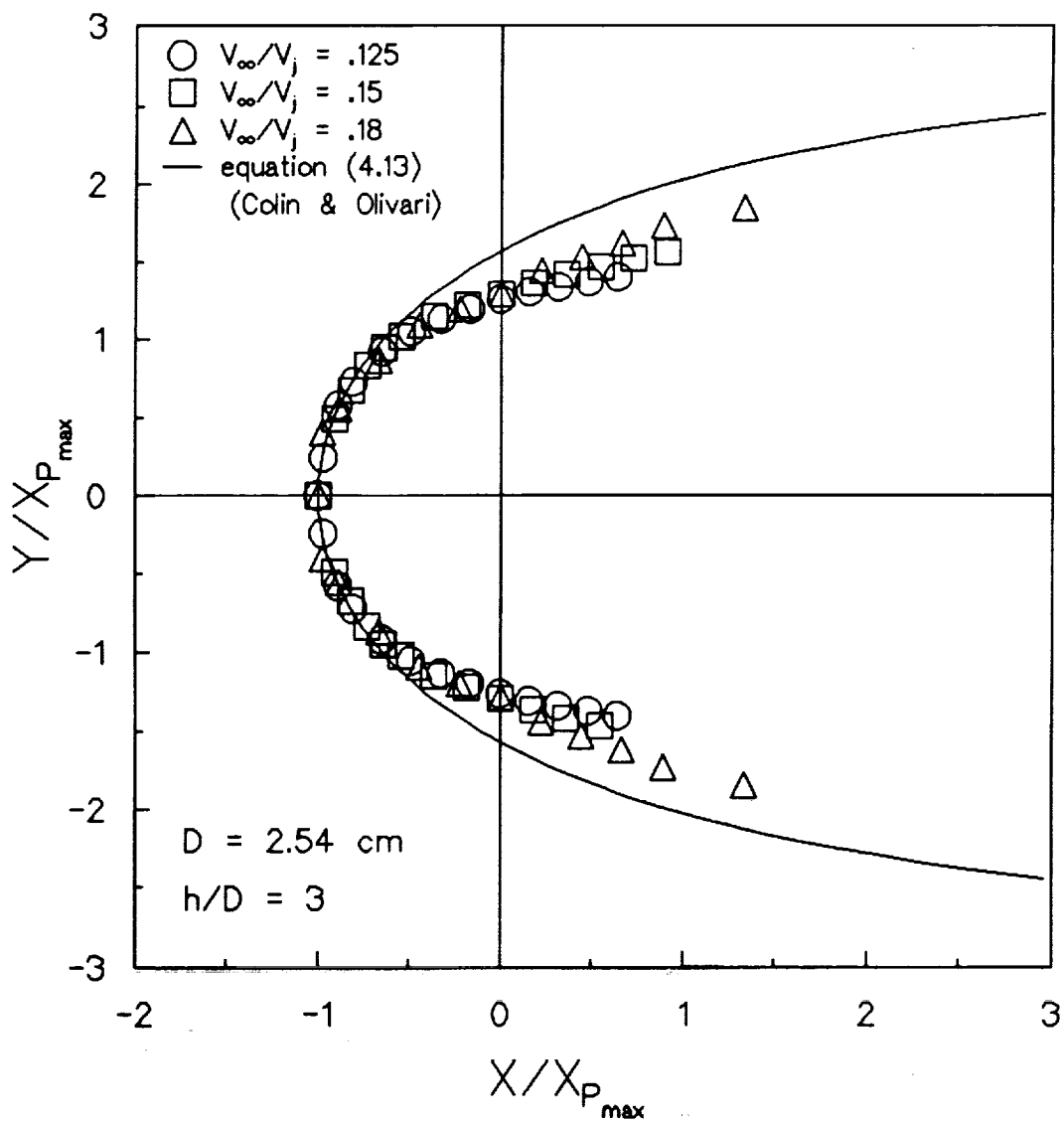


Figure 5.23: Comparison of different velocity ratio data nondimensionalized with $X_{P_{\max}}$ compared with equation 4.13 for the 2.54 cm jet nozzle.

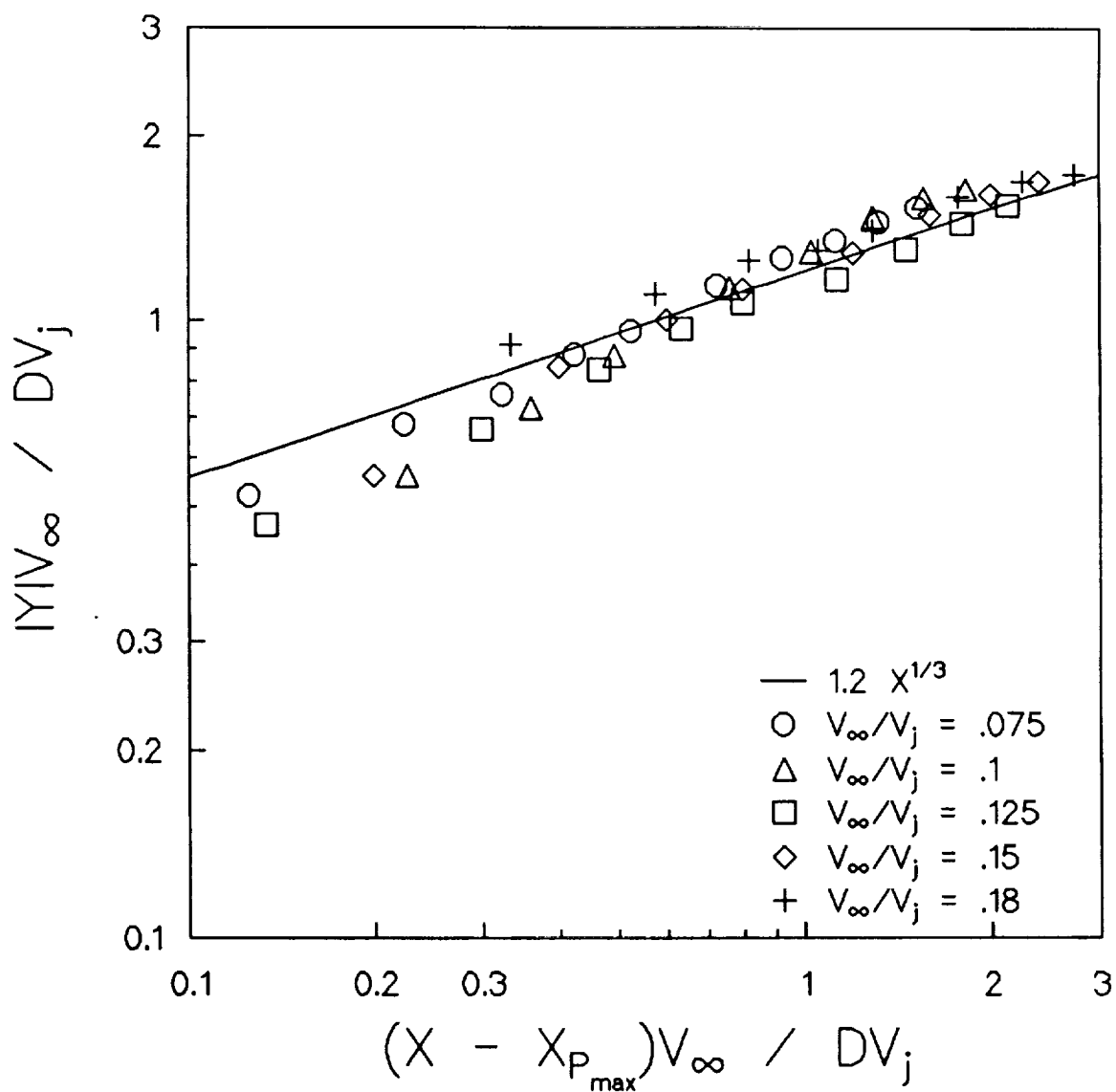


Figure 5.24: Log - Log plot of data nondimensionalized with V_{∞}/V_j , plotted with equation (4.16) for 0.91 cm nozzle; $h/D = 3$; $Z_j/D = 10$.

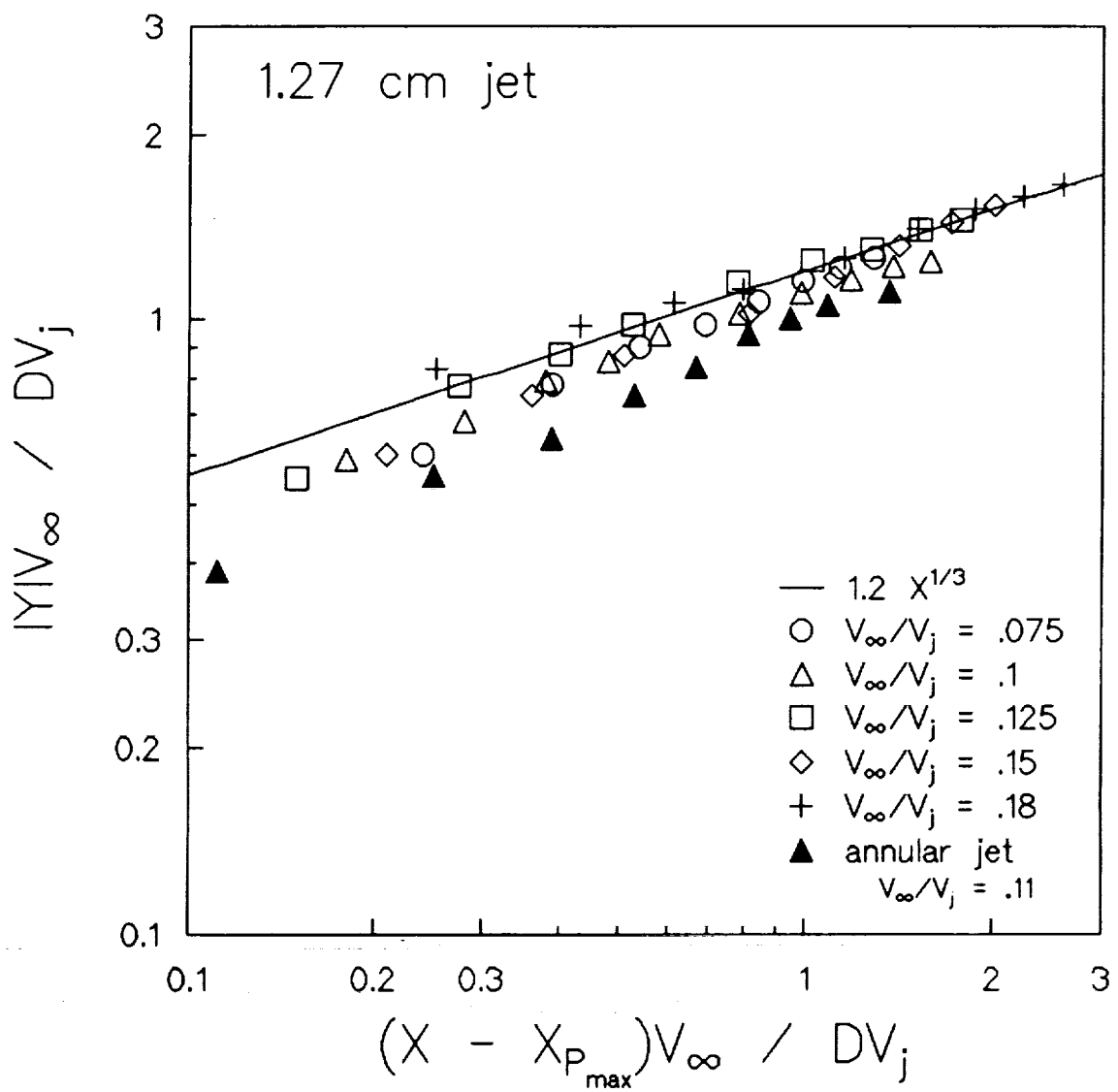


Figure 5.25: Log - Log plot of data nondimensionalized with V_∞/V_j plotted with equation (4.16) for 1.27 cm nozzle; $h/D = 3$; $Z_j/D = 7$.

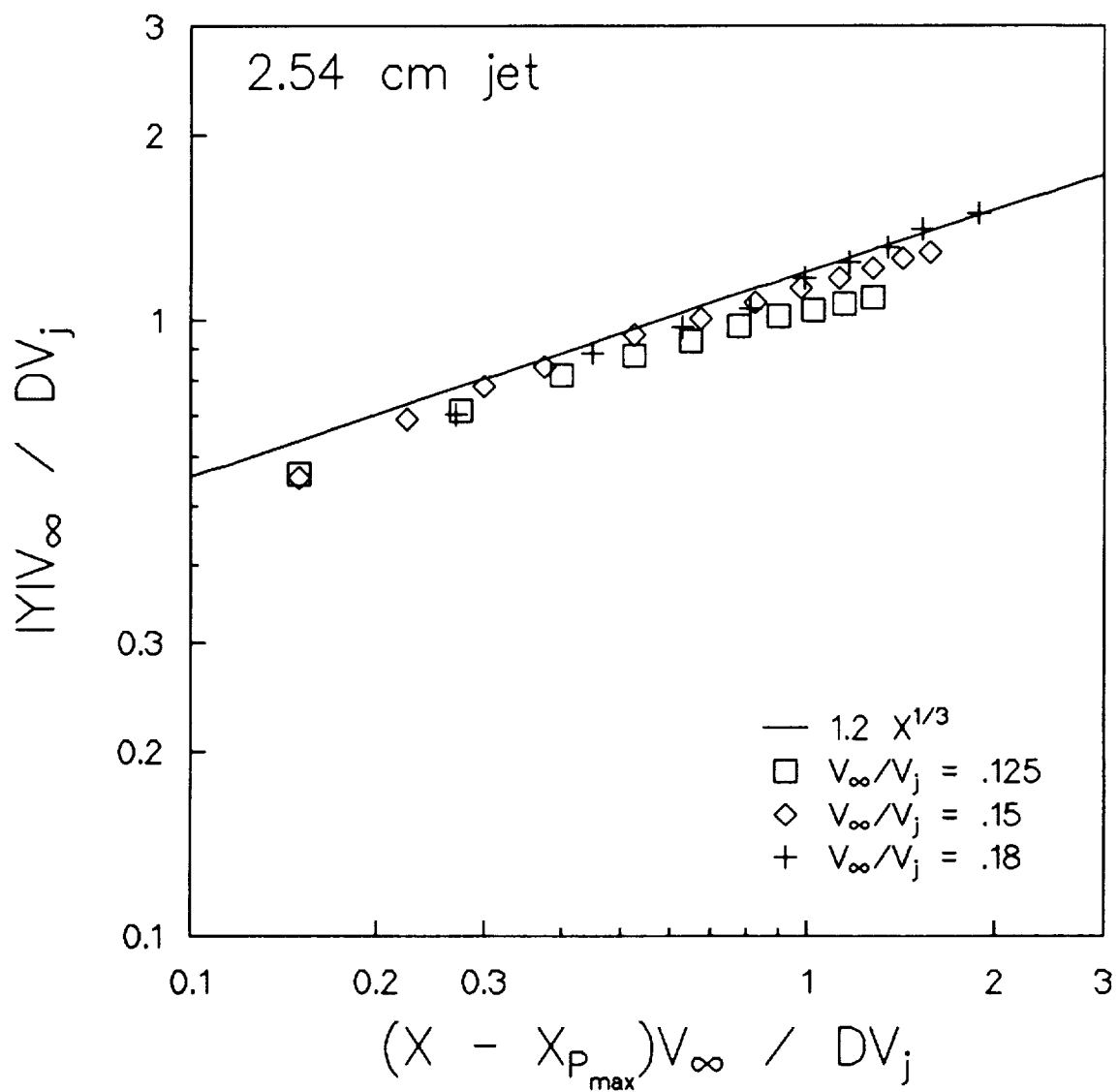


Figure 5.26: Log - Log plot of data nondimensionalized with V_∞/V_j plotted with equation (4.16) for 2.54 cm nozzle; $h/D = 3$; $Z/D = 7$.

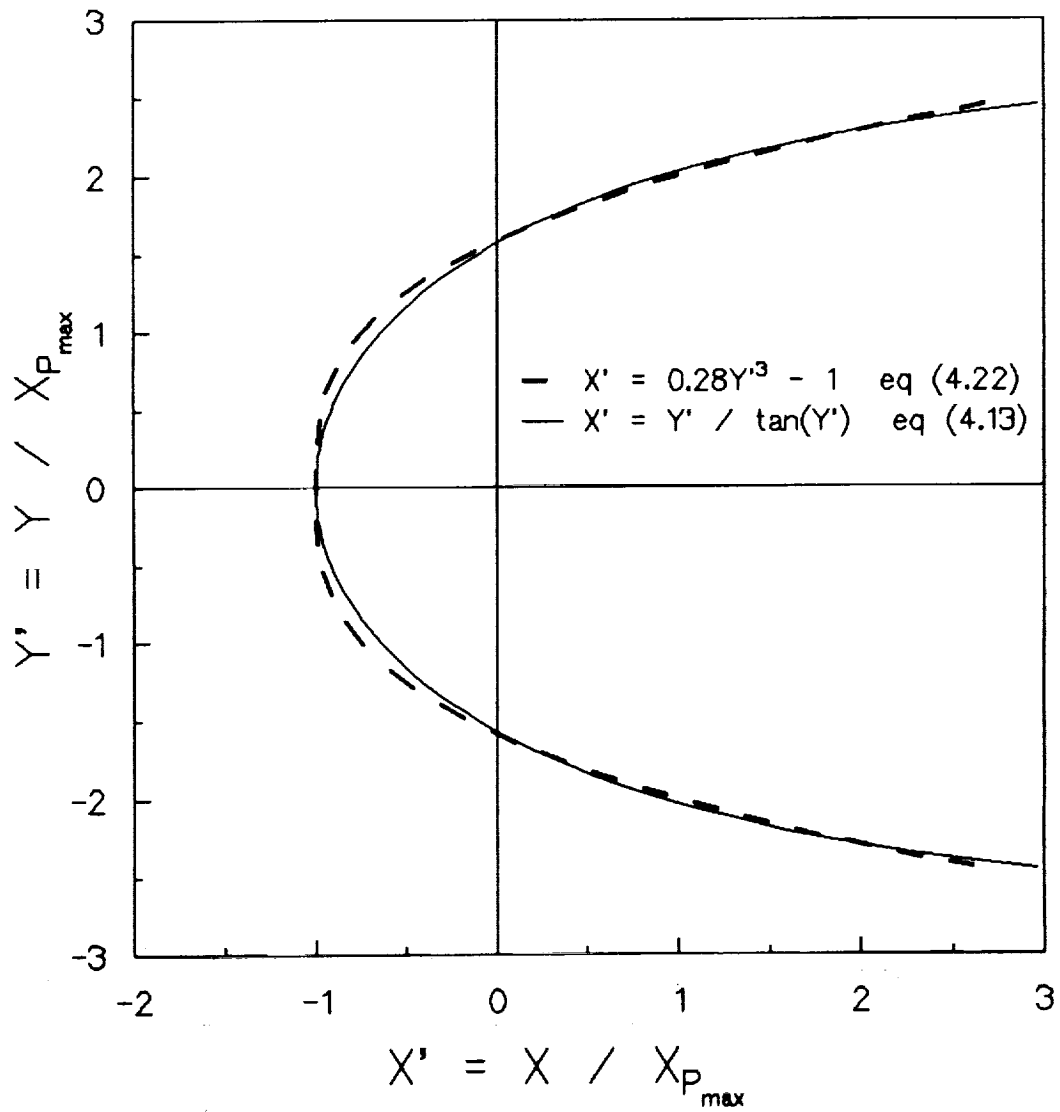


Figure 5.27: Comparison of equation (4.13) with (4.16) which is represented by (4.22) on standard axes.

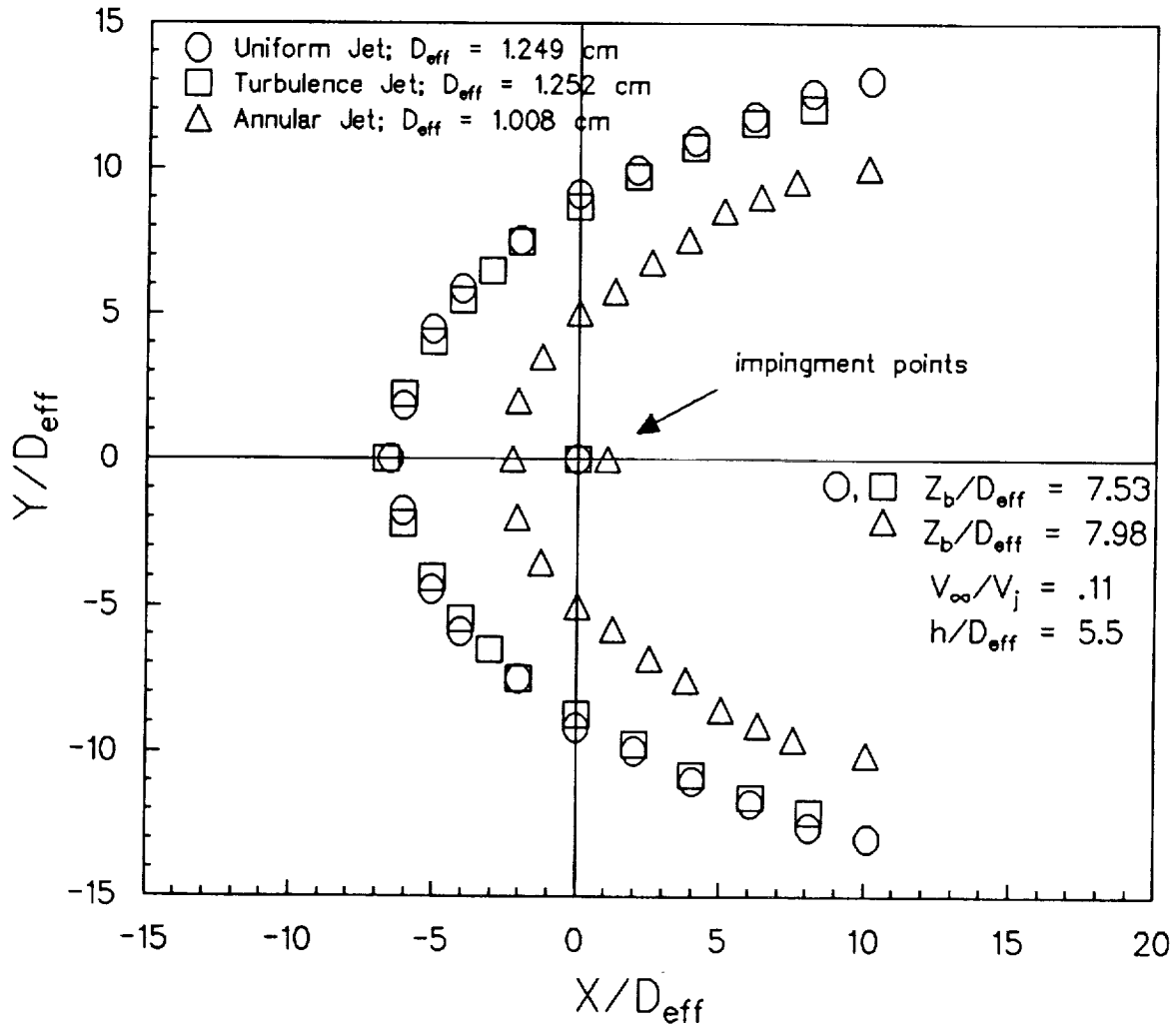


Figure 5.28: Comparison of the nondimensional shape of ground vortex for the three different nozzle configurations; h/D_{eff} equal to 5.5 and V_∞/V_j equal to .11.

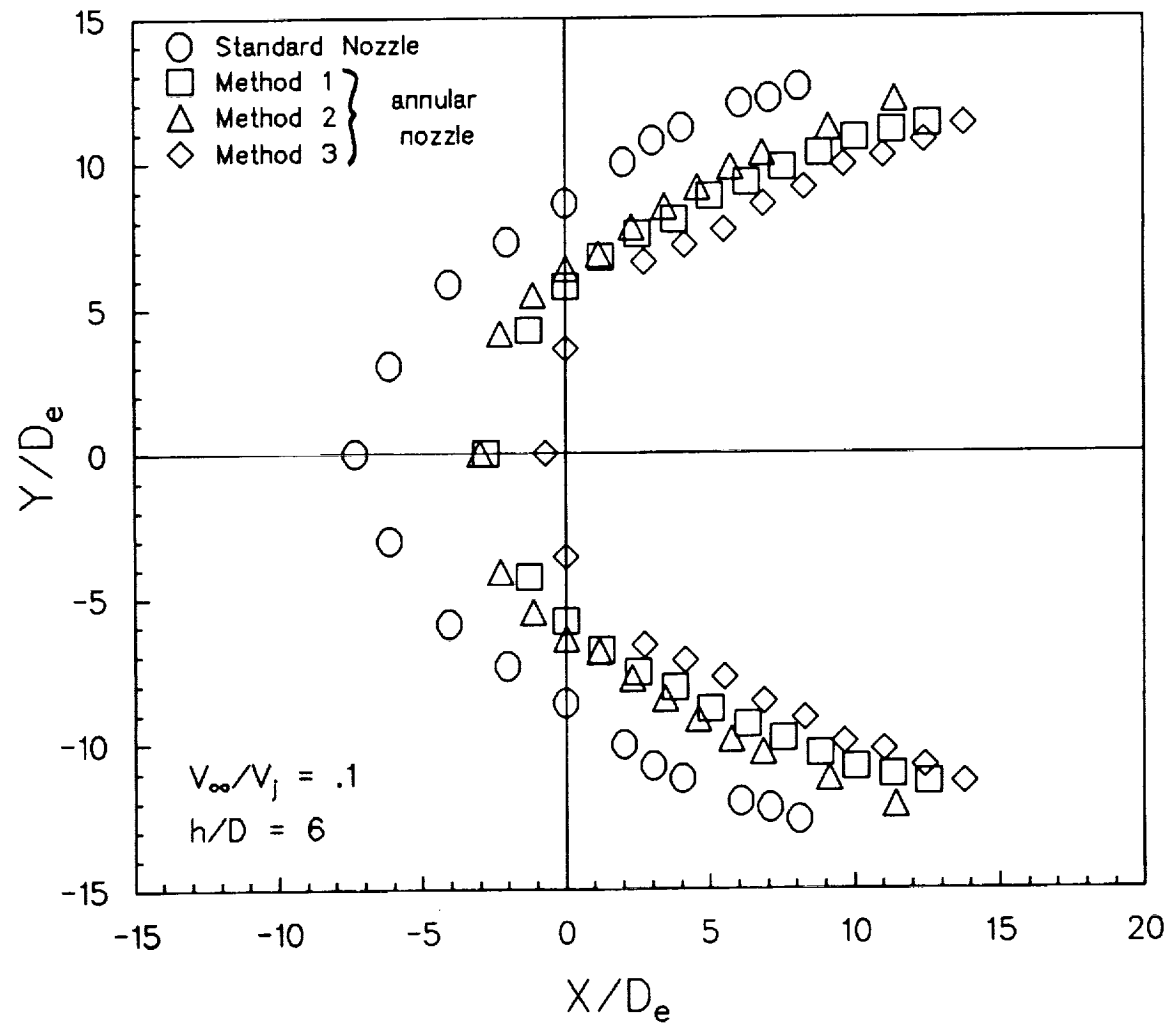


Figure 5.29: Nondimensional comparison of the three different methods of calculating D_{eff} and V_{eff} compared with the standard nozzle; $h/D_{eff} = 6$, $V_\infty/V_j = .1$.

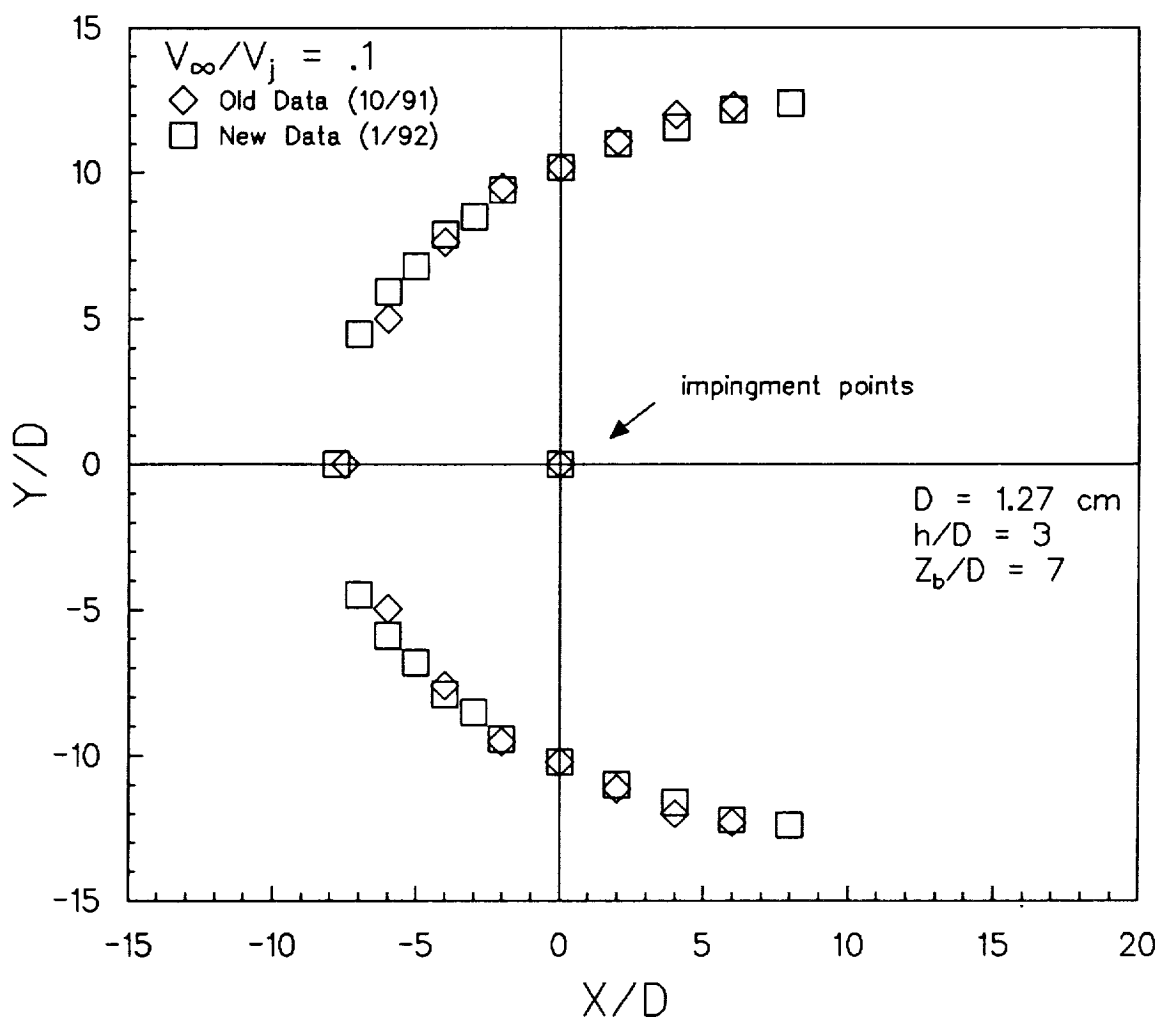
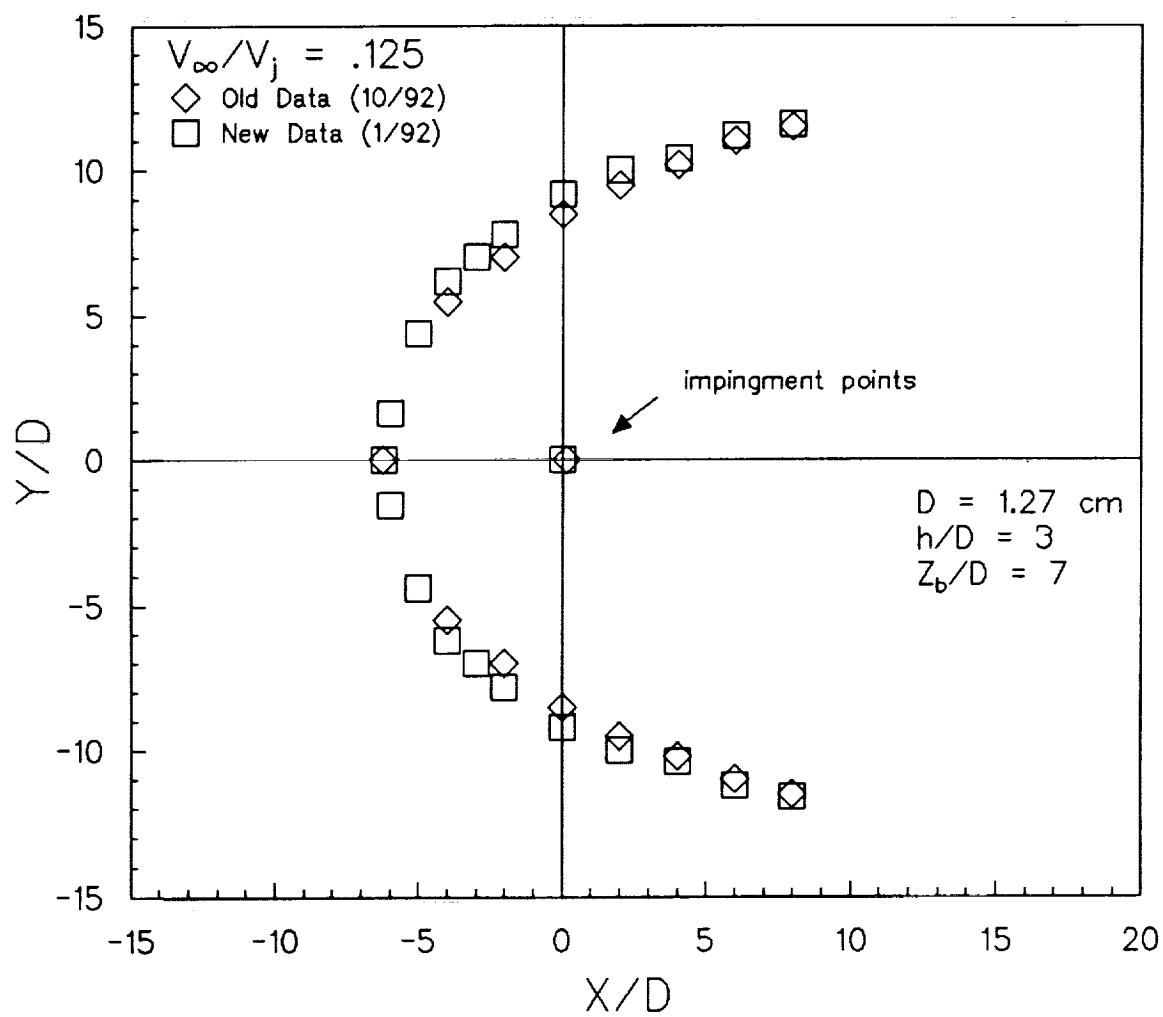


Figure 5.30: Plot of repeated data for the 1.27 cm jet nozzle; $h/D = 3$, $V_\infty/V_j = .1$.



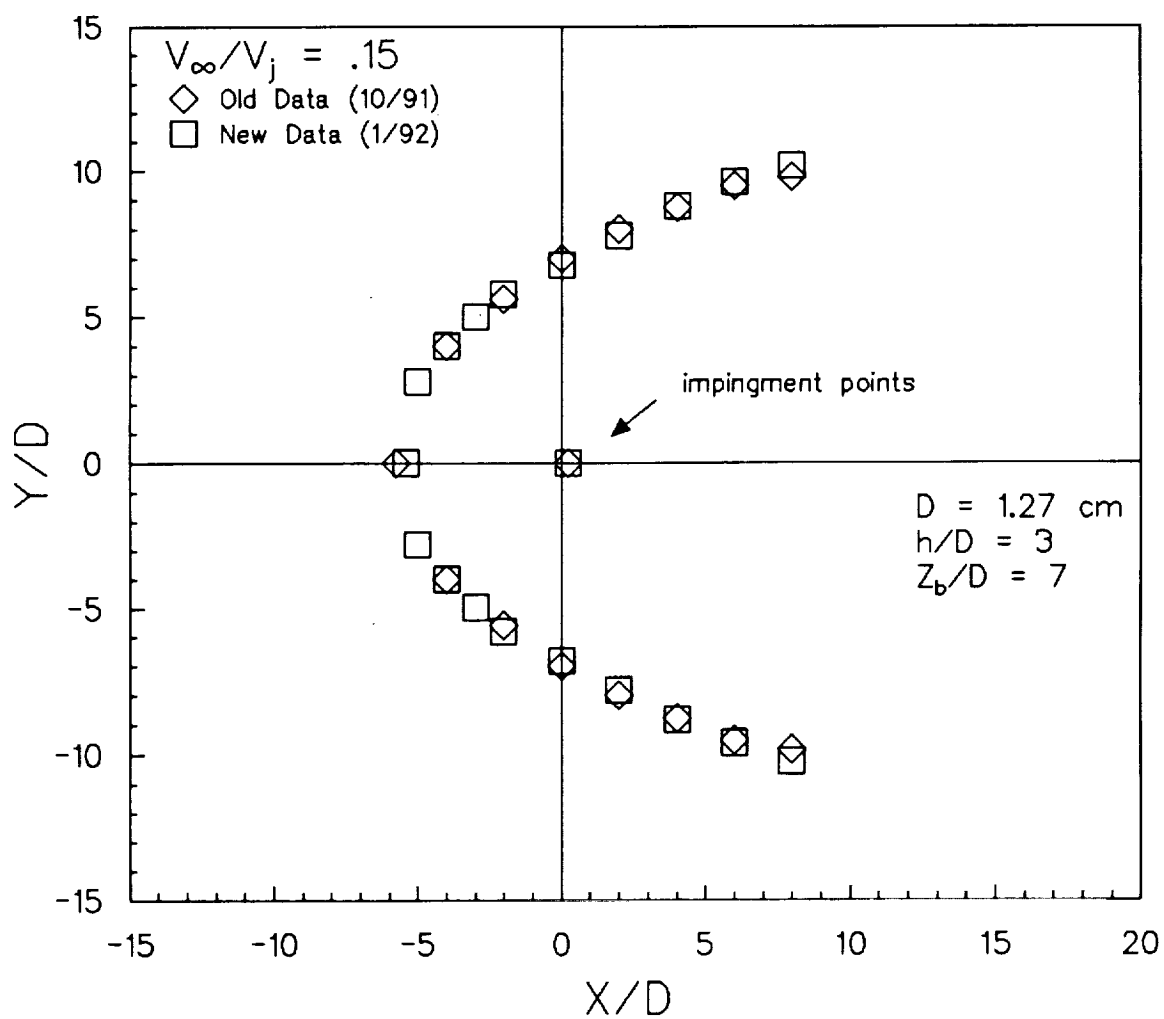


Figure 5.32: Plot of repeated data for the 1.27 cm jet nozzle; $h/D = 3$, $V_{\infty}/V_j = .15$.

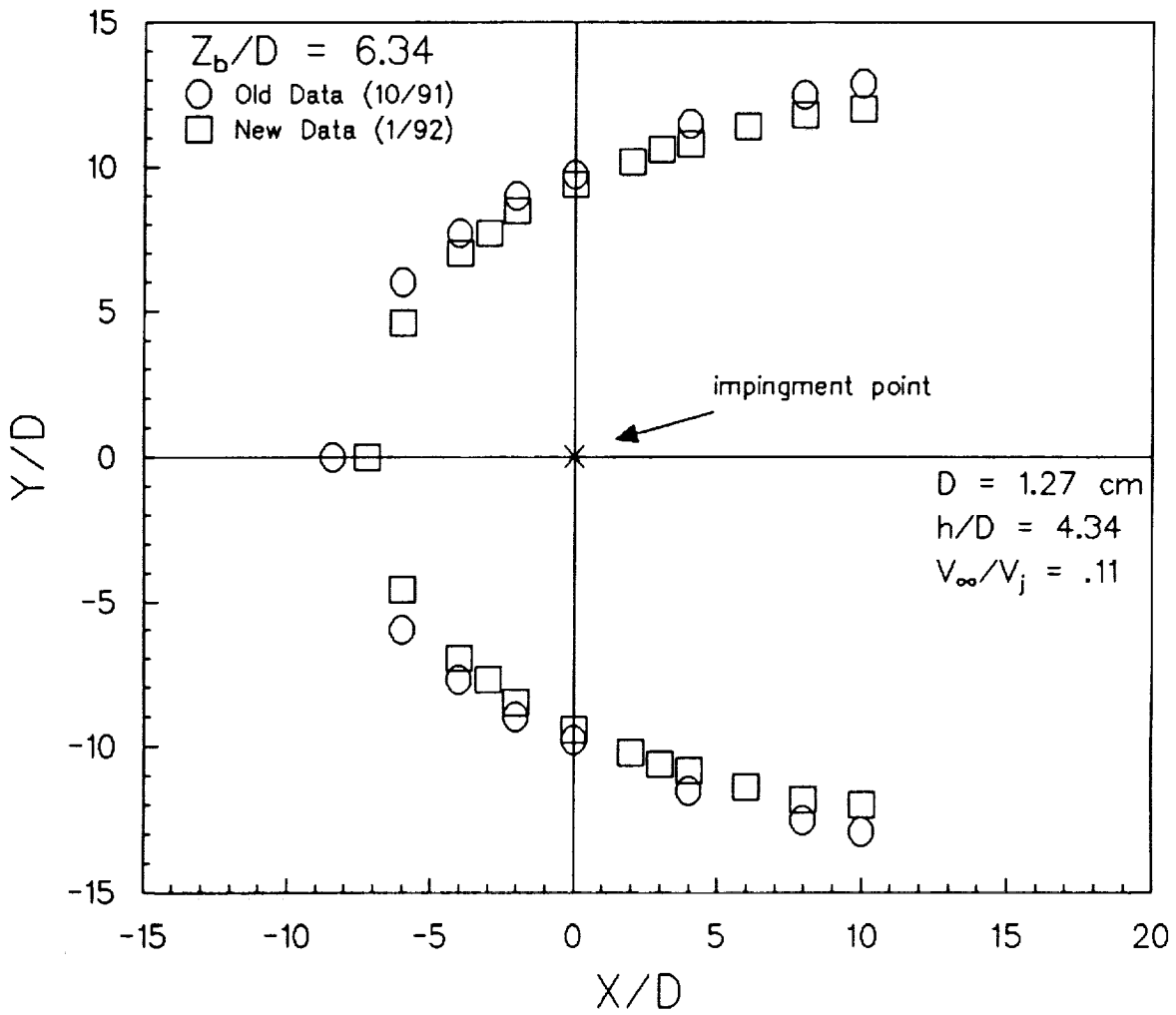


Figure 5.33: Plot of repeated data for the 1.27 cm jet nozzle with jet exit spacing of 4.34 diameters; $V_\infty/V_j = .11$, $Z_b/D = 6.34$.

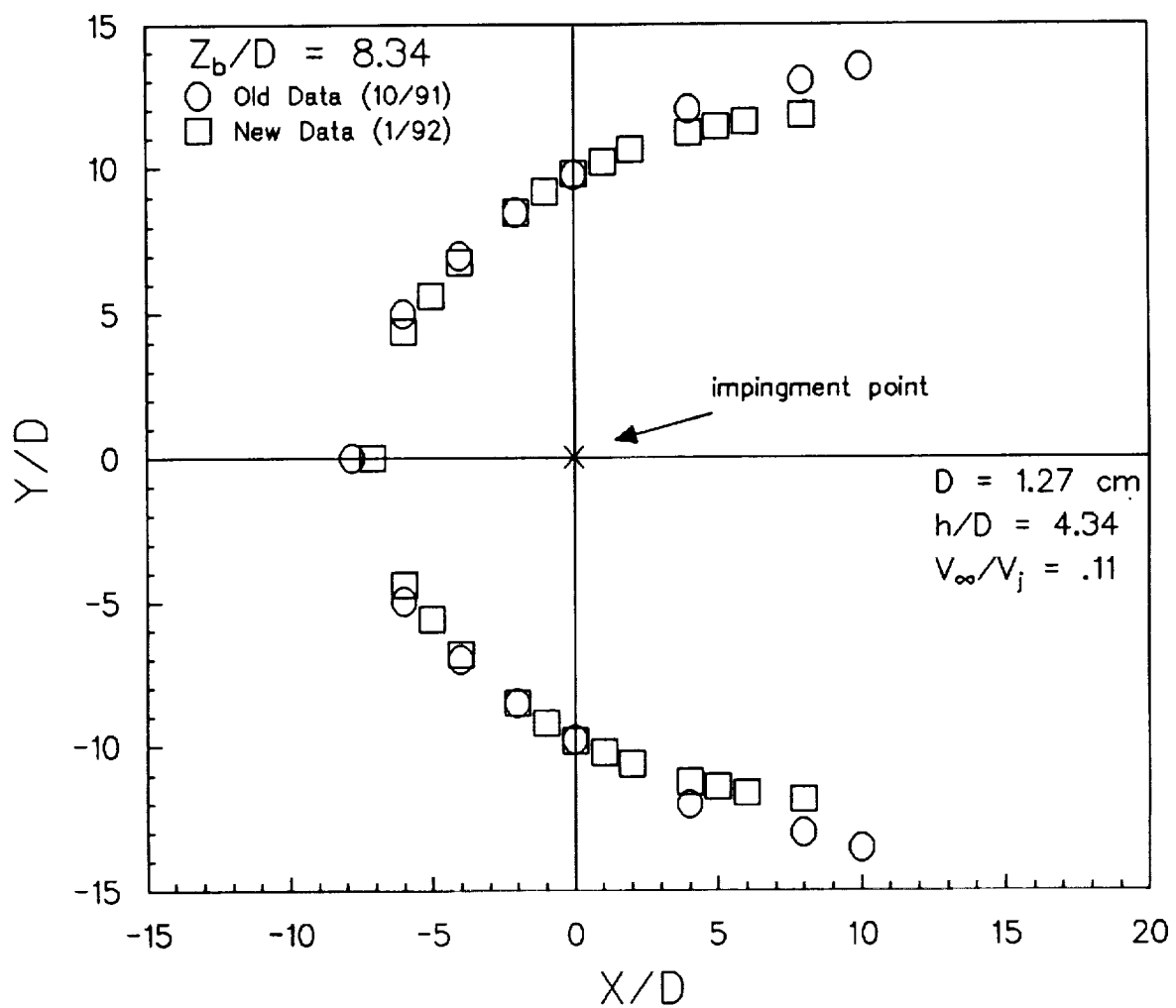


Figure 5.34: Plot of repeated data for the 1.27 cm jet nozzle with jet exit spacing of 4.34 diameters; $V_\infty/V_j = .11$, $Z_b/D = 8.34$.

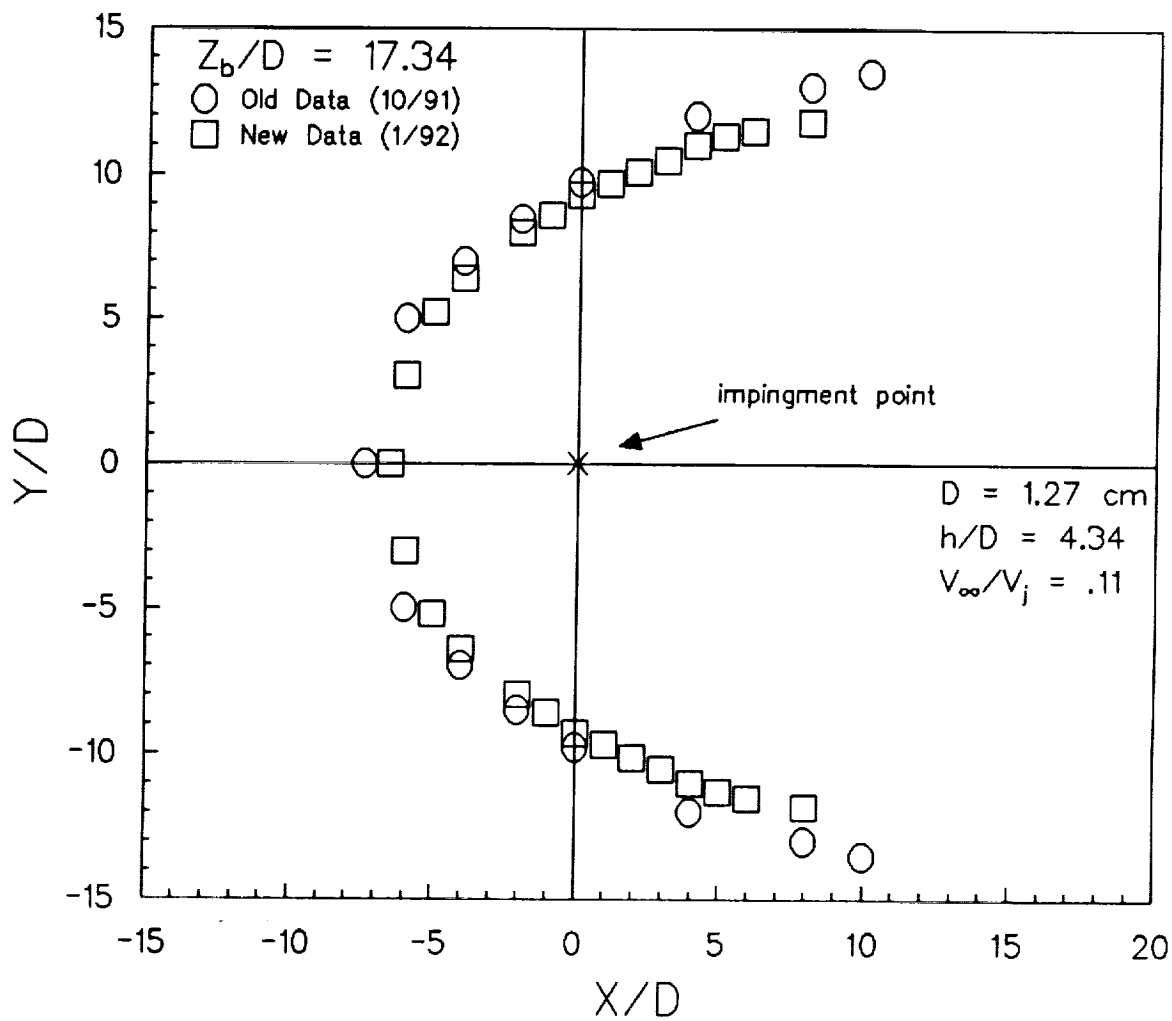


Figure 5.35: Plot of repeated data for the 1.27 cm jet nozzle with jet exit spacing of 4.34 diameters; $V_\infty/V_j = .11$, $Z_b/D = 17.34$.

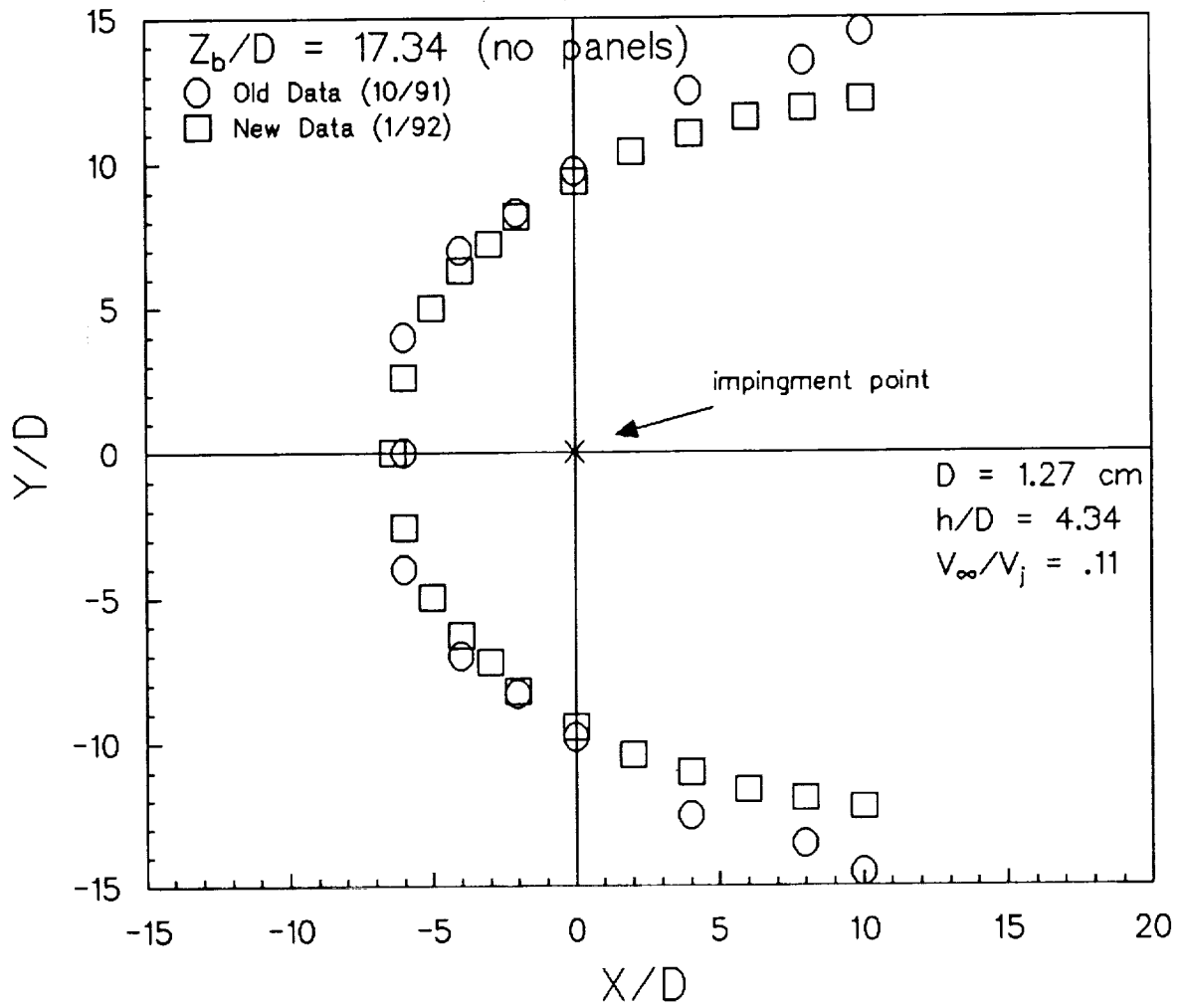


Figure 5.36: Plot of repeated data for the 1.27 cm jet nozzle with jet exit spacing of 4.34 diameters; $V_\infty/V_j = .11$, $Z_b/D = 17.34$ (panel removed).

Vector Scale — $1.000E+01$ m/s

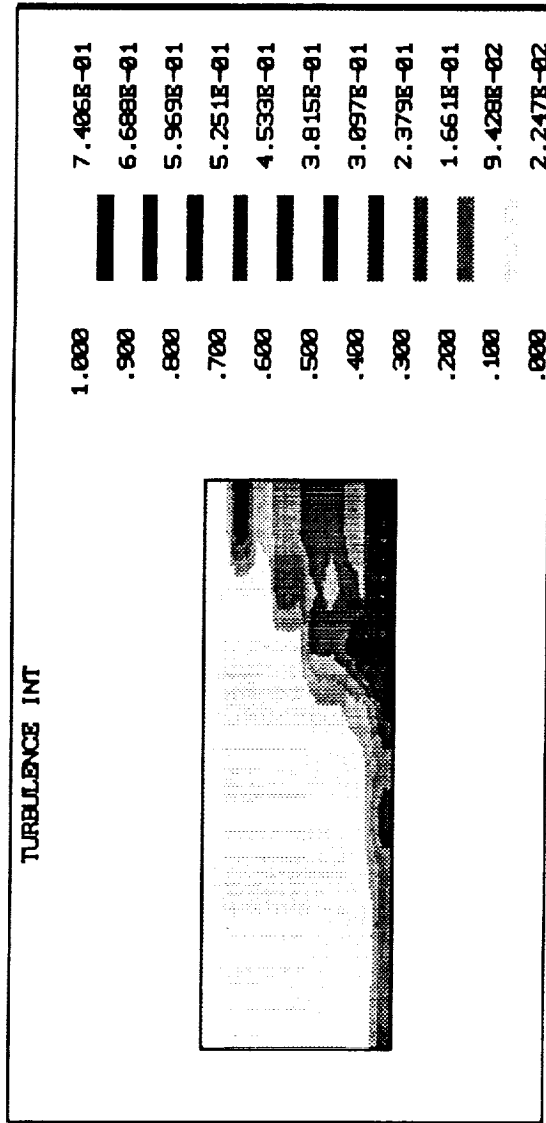
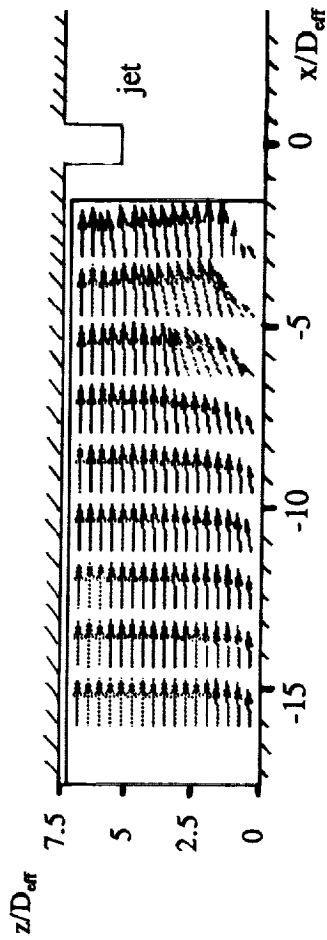


Figure 5.37: Vector plot of the LV measurements on the centerline of the ground vortex ($y/D_{eff} = 0$) for the case of $h/D_{eff} = 5.5$ and $V_{\infty}/V_j = 0.11$. x/D_{eff} ranges from 16.00 to 3.20 in increments of 1.6.

3D LDV - LEG OF GROUND VORTEX, X/D=8, STD NOZZLE, h/D=5.5

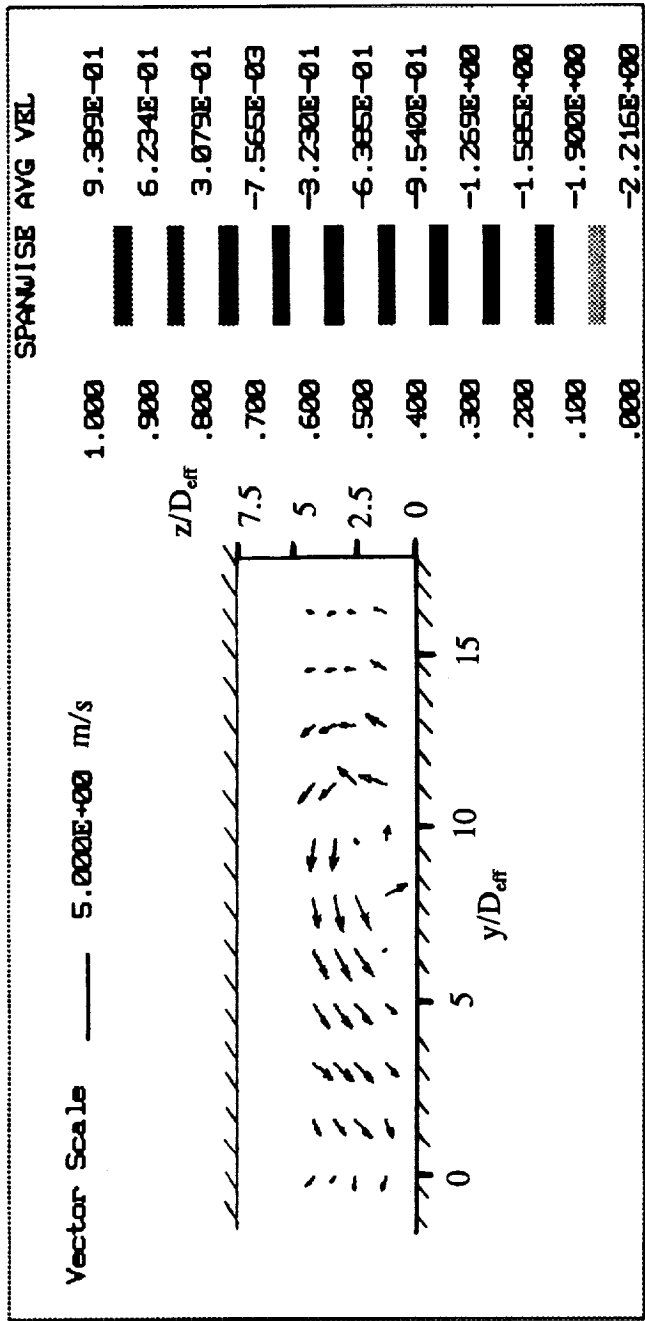
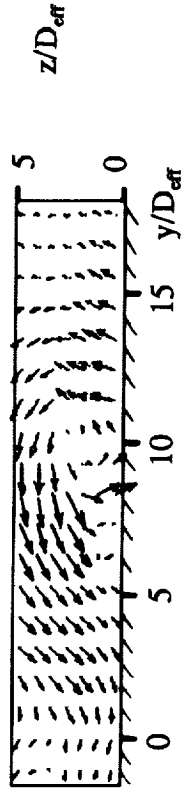


Figure 5.38: Vector plot of the LV measurements of the ground vortex leg at $x/D_{eff} = 8.00$ for the case of $h/D_{eff} = 5.5$ and $V_{\infty}/V_j = 0.11$. y/D_{eff} ranges from 0.0 to 16.00 in increments of 1.6.

Vector Scale ——— 5.0000E+00 m/s



3D LDV - LEG OF GROUND VORTEX, X/D=8, STD NOZZLE, h/D=5.5

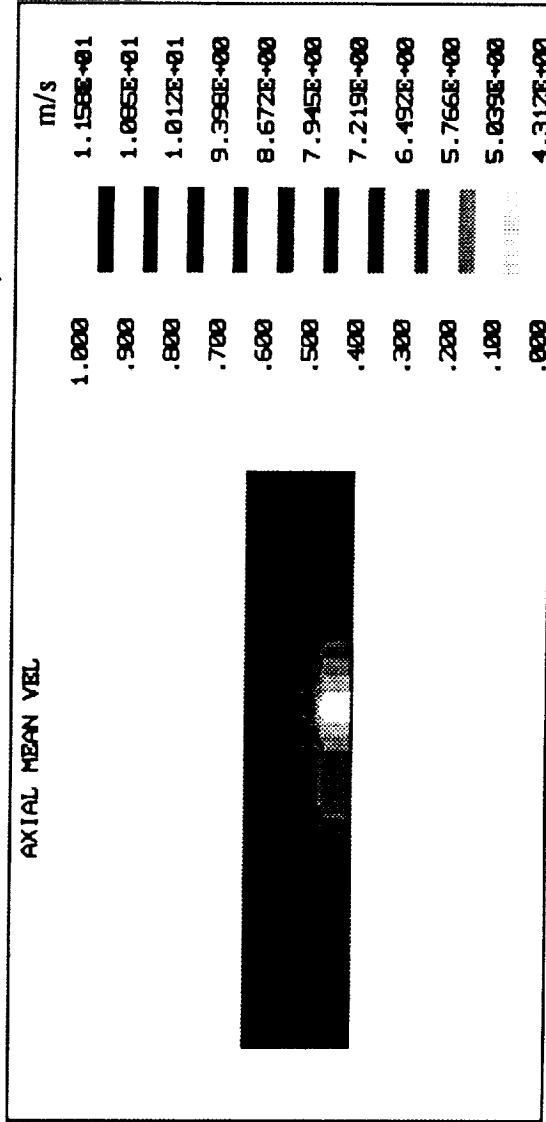
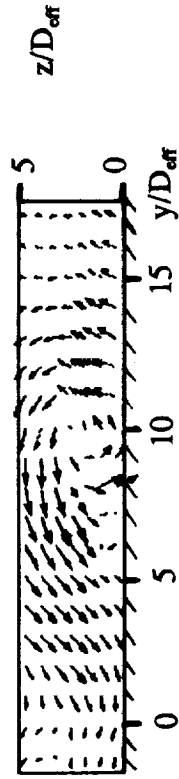


Figure 5.39: Interpolated vector plot of the LV measurements of the groundvortex leg at $x/D_{eff} = 8.00$ for the case of $h/D_{eff} = 5.5$ and $V_w/V_j = 0.11$. y/D_{eff} ranges from 0.0 to 16.00 in increments of 1.6.

Vector Scale ——— 5.000E+00 m/s



3D LDV - LEG OF GROUND VORTEX, X/D=8, STD NOZZLE, h/D=5.5

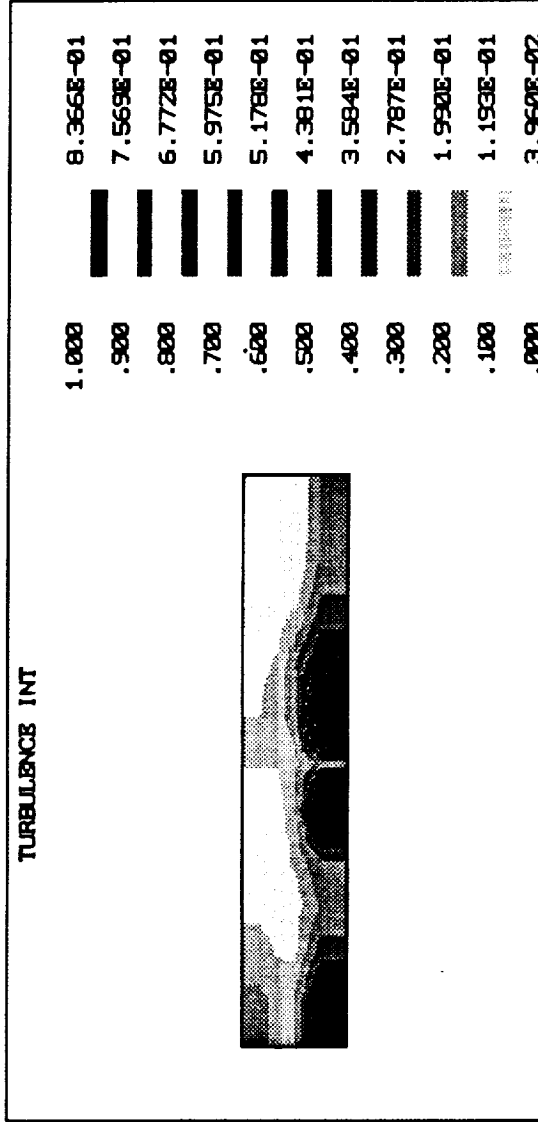


Figure 5.40: Interpolated vector plot of the LV measurements of the groundvortex leg at $x/D_{eff} = 8.00$ for the case of $h/D_{eff} = 5.5$ and $V_{\infty}/V_j = 0.11$. y/D_{eff} ranges from 0.0 to 16.00 in increments of 1.6.

CHAPTER 6: CONCLUSIONS AND RECOMMENDATIONS

6.1 Conclusions

A jet-ground interaction facility has been designed to perform experiments on the unsteady ground vortex formed by a single impinging jet angled 90 degrees from a cross flow. The jet-plenum assembly provided for highly uniform jet exit velocity profiles for the uniform jets studied, with jet exit average velocities within 2% of maximum velocities. An annular nozzle with a non-uniform velocity profile and low velocity central core has also been used to study ground vortex formation with an annular jet.

The present formation of a ground vortex had good nondimensional agreement in the parameter space examined. The effect of the jet board spacing on the ground vortex was minimal for a jet board spacing at least two nozzle diameters greater than the jet exit spacing, an observation which is consistent with previous work. The variation of maximum upstream separation distance along the centerline of the ground vortex versus velocity ratio also agreed well when compared with previous work. The effect of tunnel blockage was found to be minimal for the 1.27 cm jet nozzle at a V_∞/V_j greater than but not equal to 0.1, with V_∞/V_j equal to 0.125 having essentially no tunnel blockage effect. Attempts to analytically describe the shape and size of the ground vortex for uniform jets at different velocity ratios were fairly successful, but had significant scatter ($\pm 10\%$) illustrating the need for more advanced numerical and analytical methods to describe the size and shape of the ground vortex. The turbulence intensity at the jet exit did not change the size and shape of the ground vortex significantly. However, an annular nozzle with a non-uniform exit

velocity profile had a considerably smaller ground vortex, when nondimensionalized with effective diameter and velocity to make a consistent comparison, with maximum penetration being over 50% smaller for the annular jet. Changing the jet exit velocity profile allows for a significant change in jet near field behavior. This could provide for a significantly smaller ground vortex which would not have the strength to allow for jet exhaust ingestion into the jet engine.

LV measurements have been made in the ground vortex flow field for the uniform jet for the configuration of h/D_{eff} equal to 5.5 and V_{∞}/V_j equal to 0.11. The leading edge of the ground vortex along the centerline was measured to be approximately 8 diameters upstream, which agrees well with flow visualization. Along the centerline, the ground vortex has an elliptical shape and flow appears to recirculate in the entire region between the leading edge of the ground vortex and the jet exit plane. Turbulence intensities in the ground vortex were as high as 80% with a freestream turbulence intensity of less than 2%. The ground vortex leg was more round and had a more vortex-like structure, with circulatory mean velocities which were only about one fourth as large as the cross flow velocity. The half width of the ground vortex at x/D_{eff} equal to 8.00 was approximately equal to 13 diameters, which agrees well with flow visualization results. Turbulence intensities in the vortex leg were again as high as 80%.

6.2 Recommendations

Future studies of ground vortex formation should include measurement of the ground vortex shape and size for different h/D at selected velocity ratios in order to develop a

nondimensional collapse of the data for varying spacing, as has been performed for the different velocity ratio data (ie figures 5.21 through 5.26). A more detailed analysis should be made of the annular nozzle studied in the present work, as well as other types of annular nozzles, to determine their characteristics more completely. For example, experiments should be performed at several velocity ratios to determine the variation of maximum upstream penetration and separation along the centerline for the annular jet nozzle, as has been performed for the regular nozzle (figures 5.18 and 5.19).

More detailed LV work is also recommended in order to more completely determine the behavior of the ground vortex and to develop an understanding of the unsteadiness of the flow field. A finer measurement grid at the vortex location would give a more defined vortex and will allow more insight into the ground vortex flow field. More detailed measurements at the jet impingement point and also in the wall jet region are also needed. These measurements will require a successful seeding technique in the jet. LV measurements should also be made of the annular jet in a cross flow, for the same jet exit spacing and velocity ratio studied in the present work, allowing for a comparison with the present results. These measurements will also require successful seeding of the jet. In addition, it would be very interesting to compare LV measurements in the ground vortex with seeding of the jet only, with the present results where only the cross flow has been seeded. This would allow determination of the magnitude of bias between the two different seeding techniques.

In an attempt to understand the difference in the dynamic moving model data with respect to static wind tunnel tests, a study similar to the one performed in the present work should be made with a moving model facility to allow for direct comparison of the data

obtained in the present study. Some study of unsteadiness should be performed in this dynamic facility, and compared with the unsteadiness observed in the present study.

REFERENCES

- Abbott, W. A., "Studies of Flow Fields Created by Vertical and Inclined Jets when Stationary or Moving over a Horizontal Surface," British ARC C. P. No. 911, 1967.
- Billet, M. L. and Cimbala, J. M., "Summary of an Experimental Investigation on the Ground Vortex," Proceedings of 1987 Ground Vortex Workshop, NASA Conf. Pub. 10008, February 1988, pp. 39-60.
- Blake, W. B. and Laughrey, J. A., "F-15 SMTD Hot Gas Ingestion Wind Tunnel Test Results," AIAA paper 87-1922, presented at AIAA/SAE/ASME/ASEE Joint Propulsion Conference, San Diego, California, June 29-July 2, 1987.
- Buchave, P., "Three Component LDA Measurements," DISA Information, DISA Elektronik A/S, Skovlunde, Denmark, 1983, pp. 3-9.
- Cimbala, J. M., Stinebring, D. R., Treaster, A. L., Billet, M. L. and Walters, M. M., "Experimental Investigations of a Jet Impinging on a Ground Plane in the Presence of a Cross Flow," SAE Paper 872326, Presented at SAE Int'l. Powered Lift Conference, Santa Clara, CA, December 7-10, 1987.
- Cimbala, J. M., Billet, M. L. and Gaublumme, D. P., "Experiments on the Unsteady Ground Vortex," NASA CR-177566, August 1990.
- Chassaing, P., George, J., Claria, A., and Sananes, F., "Physical Characteristics of Subsonic Jets in a Cross-Stream," JFM, vol 62, part 1, 1974, pp. 41-64.
- Colin, P. E. and Olivari, D., "The Impingement of a Circular Jet Normal to a Flat Surface with and without a Cross Flow," Von Karmen Institute Final Technical Report, January 1969. Available through U.S. Defense Technical Information Center, AD 688953.
- Durst, F., Melling, A., and Whitelaw, J., H., Principles and Practices of Laser-Doppler Anemometry. Academic Press, NY, 1981.
- Edwards, R. V., Adrian, R., Boutier, A., Dybbs, A., Eaton, J., George, W., Meyers, J., Stevenson, W., and Yanta, W., "Report of the Special Panel on Statistical Particle Bias Problems in Laser Anemometry," ASME Journal of Fluids Engineering, Vol. 109, pp. 89-93, June 1987.
- Fearn, R. and Weston, R. P., "Vorticity Associated with a Jet in a Cross Flow," AIAA Journal, Vol. 12., no. 12, December 1974, pp. 1666-1671.

Hussein, H. J., George, W. K., and Capp, S. P., "Comparison Between Hot-Wire and Burst-Mode LDA Velocity Measurements in a Fully-Developed Turbulent Jet," AIAA paper 88-0424, presented at AIAA Aerospace Sciences Meeting, January 11-14, 1988, Reno, Nevada.

Kamotoni, Y., and Greber, I., "Measurements on a Turbulent Jet in a Crossflow," AIAA Journal, Vol. 10, no. 11, November 1972.

Katsikadelis, J. T. and Armenakas, A. E., "Analysis of Clamped Plates on Elastic Foundation by the Boundary Integral Equation Method," ASME Journal, Vol. 51, September, 1984, pp. 574-580.

Keffer J. F. and Baines, W. D., "The Round Turbulent Jet in a Cross-wind", JFM, Vol. 15, pp. 481-496.

Kemmerly, G. T. and Paulson, J. W. Jr., "Investigation of a Moving Model Technique for Measuring Ground Effects," NASA TM 4080, January 1989.

Ko, N. W. M. and Lam, K. M., "Flow Structures of a Basic Annular Jet," AIAA Journal, Vol. 23, no. 8, August 1985, pp. 1185-1190.

Kuhlman, J. M., "Variation of Entrainment in Annular Jets," AIAA Journal, Vol. 25, No. 3, March 1987, pp. 373-379.

Kuhlman, J. M. and Cavage, W. M., "Ground Vortex Formation for Uniform and Nonuniform Jets Impinging on a Ground Plane," Paper AIAA-92-4251, presented at AIAA Aircraft Design Systems Meeting, Aug. 24-26, 1992, Hilton Head, SC.

Kuhlman J. M. and Gross, R. W., "Three Component Velocity Measurements in an Axisymmetric Jet Using LDA," AIAA paper 90-1635, presented at AIAA Fluid Dynamics, Plasma Dynamics, and Lasers Conference, June 18-20, 1990, Seattle WA.

Kuhlman, J. M. and Warcup, R. W., "Effects of Jet Decay Rate on Jet-Induced Loads on a Flat Plate," J. of Aircraft, Vol. 15, No. 5, May 1978, pp. 293-297.

Kuhlman, J. M. and Warcup, R. W., "Experimental Investigations of Jet-Induced Loads on a Flat Plate in Hover out of Ground Effect," NASA CR-159004, February, 1979.

Kuhn, R. E., Del Frate, J. H., and Eshleman, J. E., "Ground Vortex Flow Field Investigation," Proceedings of 1987 Ground Vortex Workshop, NASA Conf. Pub. 10008, February 1988, pp. 121-146.

Margason, R. J., "The Path of a Jet Directed at Large Angles to a Subsonic Free Stream," NASA TN D-4919, November 1968.

Meyers, J. F., "The Elusive Third Component," Proceedings of Int'l Symposium on Laser Anemometry, ASME FED-Vol. 33, A. Dybbs & P. A. Pfund, editors, 1985, pp. 247-254.

Meyers, J. F., "Laser Velocimeter Data Acquisition and Real Time Processing using a Microcomputer," presented at 4th Int'l. Symposium on Applications of Laser Anemometry to Fluid Mechanics, Lisbon, Portugal, 1988.

Padmanabham, G. and Gowda, B. H. L., "Mean and Turbulence Characteristics of a Class of Three Dimensional Wall Jets - Part 1: Mean Flow Characteristics," ASME Journal of Fluids Engineering, Vol. 113, December 1991a, pp. 620-628.

Padmanabham, G. and Gowda, B. H. L., "Mean and Turbulence Characteristics of a Class of Three Dimensional Wall Jets - Part 2: Turbulence Characteristics," ASME Journal of Fluids Engineering, Vol. 113, December 1991b, pp. 629-634.

Paulson J. W., Jr. and Kemmerly, G. T., "An Assessment of Ground Effects Determined by Static and Dynamic Testing Techniques," Proceedings of 1987 Ground Vortex Workshop, NASA Conf. Pub. 10008, February 1988, pp. 121-146.

Rajaratnam, N., Turbulent Jets, Vol. 5, Developments in Water Science, Elsevier Publishing Co., NY, 1976.

Spreemann, K. P. and Sherman, I. R., "Effects of Ground Proximity on the Thrust of a Simple Downward-Directed Jet Beneath a Flat Surface," NACA Technical Note 4407, September, 1958.

Stewart, V. R., "The Characteristics of the Ground Vortex and its Effect on the Aerodynamics of the STOL Configuration," Proceedings of 1987 Ground Vortex Workshop, NASA Conference Publication 10008, February 1988, pp. 1-38.

Stewart, V. R., "An Experimental Investigation of the Ground Vortex Created by a Moving Jet," NASA Contractor Report 181841, July 1989.

Tennekes, H. and Lumley, J. L., Introduction to Turbulence, MIT press, Cambridge Ma., 1972.

Wright, S. J., "Mean Behavior of Buoyant Jets in a Crossflow," ASCE Journal of Hydraulics, Vol. 103, No. HY5, May, 1977, pp. 499-513.

Wynanski, I. and Fiedler, H., "Some Measurements in the Self-Preserving Jet", JFM, Vol. 38, part 3, 1969, pp. 577-612.

Yanta, W. J. and Smith, R. A., "Measurement of Turbulence-Transport Properties with a Laser Doppler Velocimeter," Paper AIAA-73-169, presented at AIAA 11th Aerospace Sciences Meeting, 1973, Washington, DC.

Ziegler, H., and Wooler, P. T., "Analysis of Stratified and Closely Spaced Jets Exhausting into a Cross Flow," NASA CR-132297, November 1973.

APPENDIX A: Calculation of Critical Distances for Nozzle Geometries

The axisymmetric jet plenum and nozzle assembly has been designed with a smooth, continuous contour for jet flow contraction. This was provided by two circular arcs of opposite curvature; this design was chosen because of ease of manufacture and low cost. The first larger circular arc in the plenum provided the majority of the flow contraction, with the second smaller arc of reverse curvature meeting at a tangency point and turning the flow back to be parallel to the jet axis. For the three different jet nozzle diameters, it was necessary to calculate the location of the tangency point and the radius of the smaller arc needed to continue a given 5 inch radius initial contraction. Consider the nozzle cross section formed by two circular arcs with two similar inscribed triangles in the YZ plane, as shown in figure A.1.

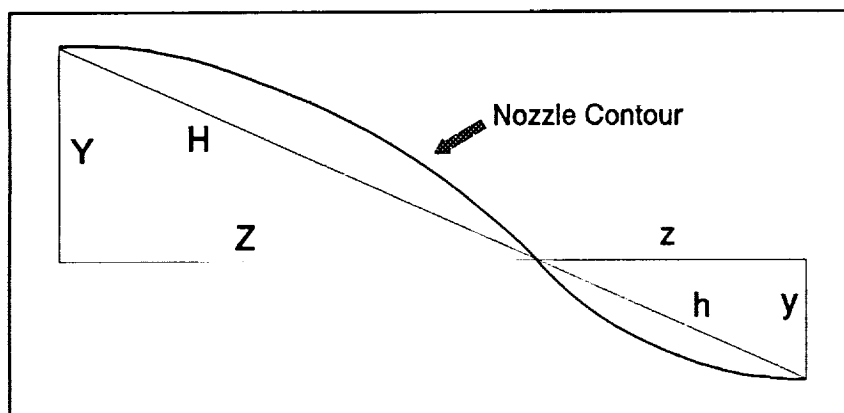


Figure A.1: Two similar triangles inscribed inside the radial arcs.

By similar triangles, equation 1 below is obtained.

$$\frac{Y}{y} = \frac{Z}{z} \quad (1)$$

The nozzle has a fixed length of 4.5 inches. With

all dimensions in inches, then the following equation holds:

$$Z + z = 4.5 \quad (2)$$

Since the plenum inlet has a given diameter of 4 inches, for the case of the half inch

diameter nozzle, the following equation for the y coordinate can be obtained.

$$Y + y = 1.75 \quad (3)$$

Solving (2) and (3) for z and y respectively and substituting into (1) a relation between Y and Z can be developed.

$$\frac{Y}{1.75 - Y} = \frac{Z}{4.5 - Z} \quad (4)$$

$$\frac{Y}{Z} = .3888 \quad (5)$$

Figure A.2 defines two secant lines inscribed in the two radial arcs that form the nozzle contour as the bases of 2 similar isosceles triangles, with the radii forming the two equal sides. From geometry it is easy to solve for θ and α .

$$\theta = \tan^{-1}\left(\frac{Y}{Z}\right) \quad (6)$$

$$\theta = 21.25 \text{ degrees}$$

$$\alpha = 180 - (\theta - 90)$$

$$\alpha = 68.75 \text{ degrees}$$

With R_1 selected as 5 (arbitrary) and H being the base of the larger isosceles triangle, the law of sines gives an expression for H.

$$\frac{H}{\sin(\beta)} = \frac{5}{\sin(\alpha)} \quad (7)$$

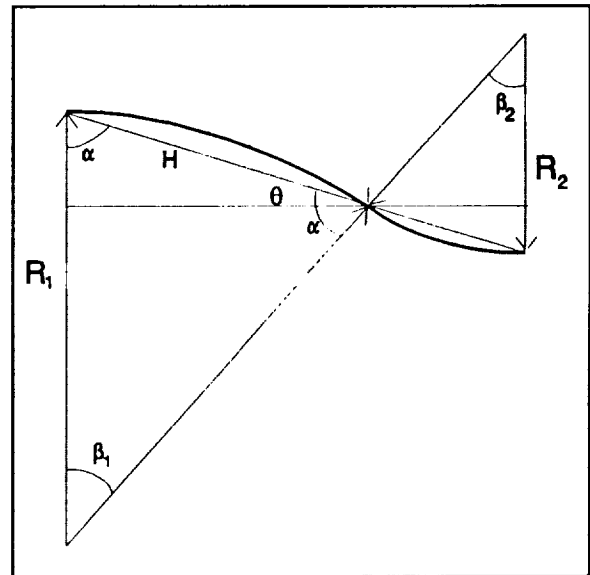


Figure A.2: The radial arcs and radii and their respective isosceles triangles.

Realizing that β_1 is equal to β_2 by similar angles, and calling that angle β , the following value was calculated.

$$\beta = 180 - 2(68.75) \Rightarrow \beta = 42.5 \text{ degrees}$$

Let l_1 be the cosine component of H (Z in figure A.1), which represents the distance of the initial contraction along the axis of symmetry from the start of the contraction. Let l_2 be defined as the distance needed to complete the contraction. So by equation (7), numerical values for H and consequently l_1 can be obtained.

$$H = \frac{\sin(47.26)(5)}{\sin(68.75)} \Rightarrow H = 3.6245 \text{ inches} \quad (8)$$

$$l_1 = H \cos(\theta) \Rightarrow l_1 = 3.378 \text{ inches} \quad (9)$$

Since the assembly length is 4.5 inches long the following relation gives l_2 .

$$l_2 = 4.5 - l_1 \Rightarrow l_2 = 1.1210 \text{ inches} \quad (10)$$

To determine the radius of the smaller arc, the slope at the tangency point was first calculated knowing the radius of the larger arc, and then was used to determine the smaller radius. A circle in the YZ plane with radius R can be described by the following equation.

$$Y^2 + Z^2 = R^2 \quad (11)$$

or

$$Y = \sqrt{R^2 - Z^2} \quad (12)$$

The derivative of (12) gives the following equation:

$$\frac{dY}{dZ} = -\frac{Z}{\sqrt{R^2 - Z^2}} \quad (13)$$

Consider the tangency point of the two arcs. First, for the larger arc (larger triangle) with a radius of 5 inches, at Z equal to 3.378 inches, the following slope can be obtained.

$$\frac{dY}{dZ} = -\frac{3.378}{\sqrt{5^2 - 3.378^2}} \rightarrow \frac{dY}{dZ} = -.9164$$

For the smaller arc (smaller triangle) Z is -1.1210 inches, noting that the center of the arc is directly above the end of the nozzle contraction. Using (13) and solving for R, the following value of R is obtained.

$$R^2 = \left(\frac{Z}{dY/dZ}\right)^2 + Z^2 \quad (14)$$

$$R = \sqrt{\left(\frac{1.1210}{-.9164}\right)^2 + 1.1210^2} \rightarrow R = 1.6607 \text{ inches}$$

Figure A.3 illustrates the significant dimensions needed to machine the three nozzle sizes of diameter equal to 1.0, 0.5, and 0.375 inches (2.54, 1.27, and 0.91 cm respectively). Table A.1 gives the dimensions as calculated by the above procedure. Even though the present nozzles have not followed the usual practice of using higher order polynomial contours (3rd and 4th order), the measured exit velocity profiles presented in chapter 5 have showed the jet exit velocity profiles to be quite uniform.

Table A.1: Table of significant dimensions of the 3 different diameter nozzles

d (inches)	l_1 (inches)	l_2 (inches)	R_2 (inches)	t_1 (inches)	t_2 (inches)
1	3	1.5	2.5	0	1.0
0.5	3.3780	1.1210	1.6607	.3780	.6863
.375	3.4655	1.0344	1.4925	.4655	.6041

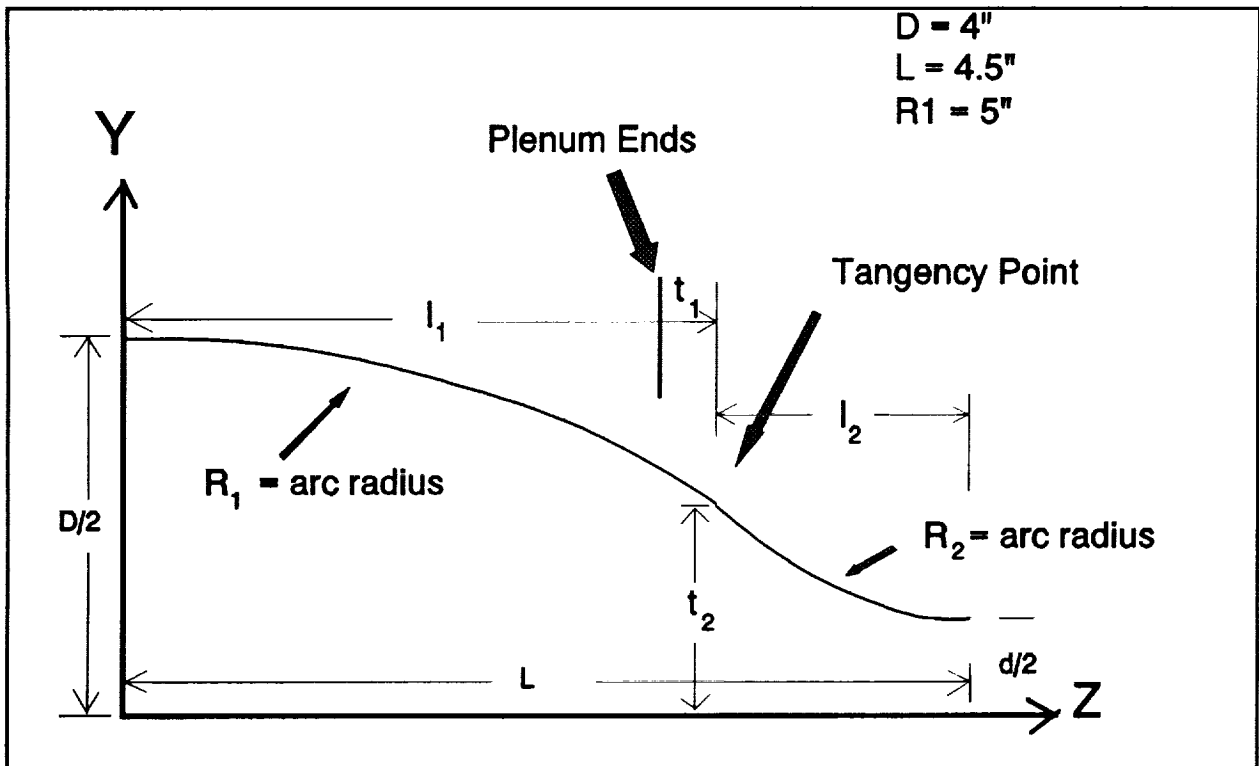


Figure A.3: Schematic of significant dimensions for machining the nozzles

APPENDIX B: LV Theory and Methods

Laser Doppler Velocimetry (LV) is a non-intrusive method of measuring fluid velocity using the interference characteristics of coherent light. The dual beam fringe method is the most common method of LV, as well as the method employed for the present work. With this method, a laser beam is split into two beams of equal intensity, and then these beams are crossed with a converging lens. Due to the interference characteristics of light, interference fringes are created at the crossing point of the two laser beams, which is known as the probe volume (see figure B.1). A particle traveling through the probe volume will scatter light at a frequency proportional to the velocity of the particle. These Doppler frequencies can be determined by a photomultiplier tube focused on the probe volume and processed for statistical time record of velocity making LV ideal for turbulent flow measurements. An LV requires no calibration since the Doppler frequency (f_d) is a function of the wave length of the coherent light λ , the beam crossing half angle θ , and the velocity of the scattering particle as seen in the below equation (Durst et. al., 1981).

$$f_d = \frac{2u}{\lambda} \sin\left(\frac{\theta}{2}\right)$$

Unfortunately, the above equation is not valid for velocities in either direction through the probe volume. Thus a Bragg cell must be utilized to shift the initial frequency of zero to some greater frequency which is then noted as velocity zero. Negative velocities can then be measured as those frequencies less than the Bragg shift, up to a negative velocity equal to that corresponding to the Bragg shift.

The probe volume or measuring volume has an elliptical shape, and the crossing of several probe volumes (several components) gives the probe volume roughly the shape of a football. To determine the size of the probe volume, the following two equations are used for d_x and d_y which represent the major and minor axis of the probe volume as measured to e^{-2} intensity.

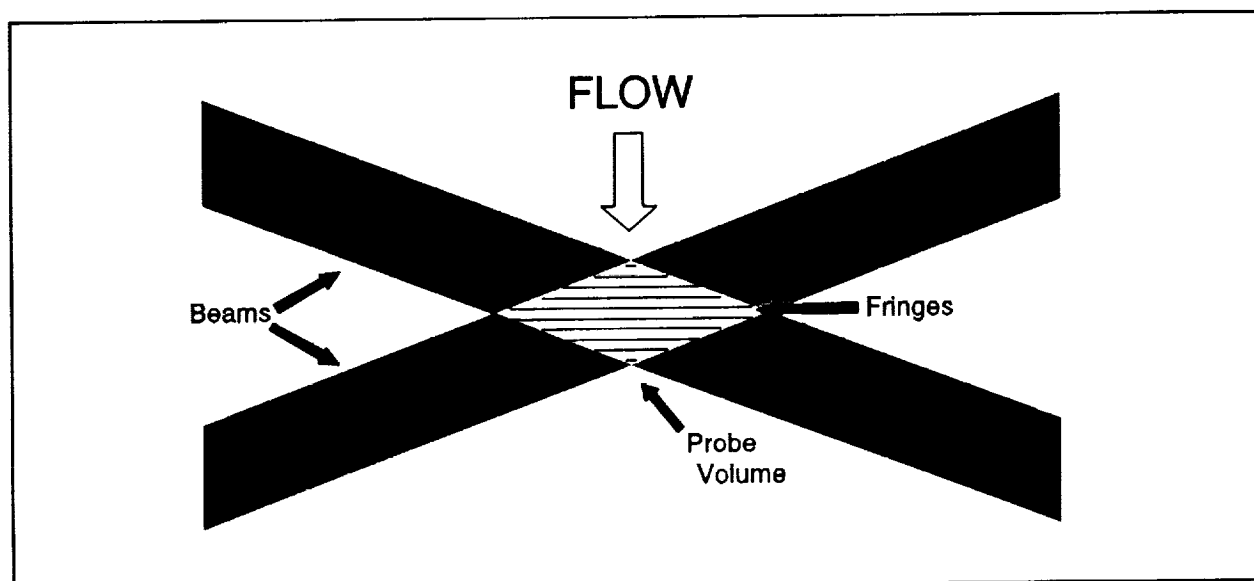


Figure B.1: Schematic of fringes created in the probe volume.

$$d_x = \frac{d_f}{\cos(\theta/2)}$$

$$d_y = \frac{d_f}{\sin(\theta/2)}$$

In the above equation d_f is the diameter of the focused beam which is given below.

$$d_f = \frac{4f_1\lambda}{\pi E d_b}$$

where f_1 is the focal length of the transmitting lens, d_b is the diameter of the beam as

measured to e^{-2} intensity, and E is the beam expansion factor. The number of fringes in the probe volume is calculated using the following equation in which D is the beam spacing.

$$N_f = \frac{4D}{\pi d_b}$$

Figure B.2 is a detailed schematic of a single channel LV illustrating the required optics and electronics. Note that the three component LV used in the present study is considerably more complex in nature.

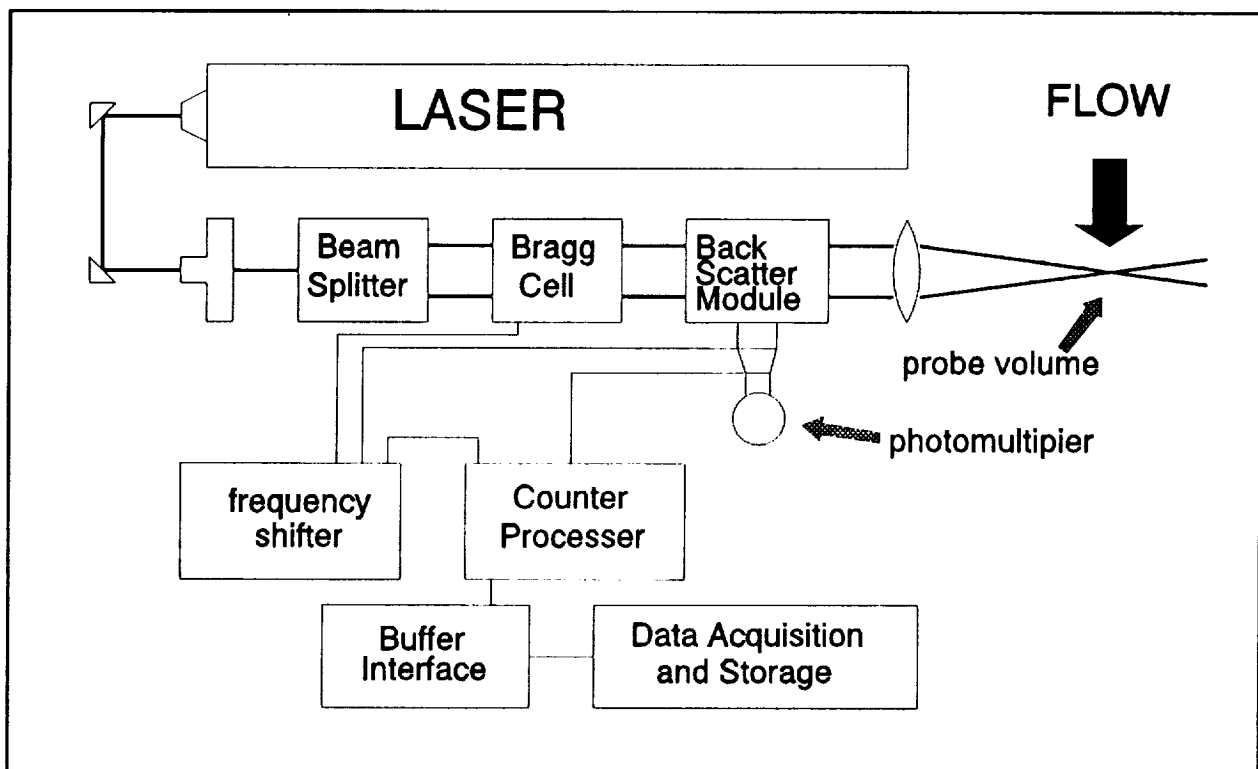


Figure B.2: Schematic of simple single channel LV system operated in backscatter.

APPENDIX C: Derivation of Effective Diameter and Velocity

The following derivation is similar to that of Ziegler and Wooler (1973). It assumes an equivalent isentropic nozzle with a uniform velocity with the same initial mass flow rate and integrated momentum flux as the actual nozzle having a non-uniform velocity. The integrated momentum flux often referred to as momentum flux (MF) of a jet of uniform velocity V and jet exit area A assuming subsonic flow is given by the following equation.

$$MF = \rho AV^2 \quad (1)$$

Dynamic pressure is given by the following equation in which ρ is the fluid density.

$$q = \frac{\rho V^2}{2} \quad (2)$$

Dividing (1) by 2 and substituting in (2), Equation (3) is obtained. This gives area in terms of MF assuming uniform velocity V .

$$A = \frac{MF}{2q} \quad (3)$$

Consider the equation for mass flow rate for an isentropic nozzle of exit area A .

$$\dot{m} = AP_o M \sqrt{\frac{\gamma}{RT_o} \left(1 + \frac{\gamma-1}{2} M^2\right)^{-\frac{\gamma+1}{2(\gamma-1)}}} \quad (4)$$

In this equation P_o is the total pressure, T_o is the total temperature, R is the ideal gas constant, and γ is the ratio of specific heats. From compressible flow, total pressure is related to static pressure (P) by the isentropic relation given below.

$$P_o = P \left(1 + \frac{\gamma-1}{2} M^2\right)^{\frac{\gamma}{\gamma-1}} \quad (5)$$

Substituting (5) into (4) gives the following result.

$$\dot{m} = A P M \sqrt{\frac{\gamma}{RT_o} \left(1 + \frac{(\gamma-1)}{2} M^2\right)^{1/2}} \quad (6)$$

Knowing that V is equal to Ma , where M is the Mach number and a is the speed of sound, and substituting into (2), equation (7) is obtained.

$$M^2 = \frac{2q}{\rho a^2} \quad (7)$$

Substituting (7) into (6) eliminates M , and simplifying gives an expression in terms of dynamic pressure.

$$\begin{aligned} \dot{m}^2 &= \frac{2A^2 P^2 q \gamma}{RT_o \rho a^2} \left(1 + \frac{(\gamma-1) q}{\rho a^2}\right) \\ \dot{m}^2 &= \frac{2A^2 P q}{RT_o} \left(\frac{P \gamma}{\rho a^2}\right) \left(1 + \frac{(\gamma-1) q}{\rho \gamma RT}\right) \\ \dot{m}^2 &= \frac{2A^2 q P}{RT_o} \left(1 + \frac{q(\gamma-1)}{\gamma \rho}\right) \end{aligned} \quad (8)$$

Eliminating A with equation (3), and simplifying, an expression relating an equivalent momentum flux to q can be obtained.

$$\dot{m}^2 = \frac{2MF^2 P q}{4q^2 RT_o} \left(1 + \frac{(\gamma-1) q}{\gamma P}\right)$$

$$\dot{m}^2 (2RT_o q) = MF^2 P \left(1 + \frac{(\gamma-1)q}{\gamma P}\right)$$

$$MF = \dot{m} \sqrt{\frac{2RT_o q}{P + \frac{(\gamma-1)}{\gamma} q}} \quad (9)$$

Using q_{\max} as the dynamic pressure to reference MF to, the result of (9) is used to obtain the effective area (A_{eff}) with (3), from which D_{eff} is obtained. Effective velocity (V_{eff}) is obtained using the relation for volume flow rate (Q). To summarize, the following procedure is used to determine D_{eff} and V_{eff} .

- 1.) Integrate for Q, measure q_{\max} , and calculate mass flow rate.
- 2.) Calculate equivalent momentum flux using equation (9).

$$MF = \dot{m} \sqrt{\frac{2RT_o q_{\max}}{P + \frac{(\gamma-1)}{\gamma} q_{\max}}}$$

- 3.) Calculate effective area, eg effective diameter.

$$A_{\text{eff}} = \frac{MF}{2q_{\max}} \quad \Rightarrow \quad D_{\text{eff}} = \sqrt{\frac{4A_{\text{eff}}}{\pi}}$$

- 4.) Calculate effective velocity.

$$V_{\text{eff}} = \frac{Q}{A_{\text{eff}}}$$

This procedure has been used previously by Kuhlman and Warcup (1979, 1980).


```

20  DEFINT I, K, N
    DEFSTR S
    PI = 3.14159
    RCNST = 1716
    GAMMA = 1.4

input initial data ; define nozzle type

CLS
PRINT : PRINT
INPUT " NAME OF INPUT FILE"; SNAM3$
PRINT
INPUT " NAME OF OUTPUT FILE"; SNAM1$
PRINT
INPUT " NAME OF RAW DATA FILE"; SNAM2$
PRINT
OPEN SNAM3$ FOR INPUT AS #3
INPUT #3, SIZE$, DIAM, PNOZ, TATM, PATM

determine density of air and manometer fluid

IF TATM > 72 THEN
    RHOW = 1.94
ELSE
    IF TATM < 78 THEN
        RHOW = 1.935
    ELSE
        RHOW = 1.93
    END IF
END IF
RHO = (PATM * 2116.2 / 29.92) / (RCNST * (TATM + 459))

open data file; write initial information

OPEN SNAM1$ FOR OUTPUT AS #1
OPEN SNAM2$ FOR OUTPUT AS #2
STIME$ = TIME$
WRITE #2, SNAM2$
WRITE #2, SIZE$, DATE$, STIME$
WRITE #2, DIAM, PATM, TATM
WRITE #2,
WRITE #1, SNAM1$
WRITE #1, SIZE$, DATE$, STIME$
WRITE #1,
CLS

read pressures

PRINT : PRINT
PRINT " THE PRESSURE STARTING AT THE FIRST POINT TO THE PRESSURE AT"
PRINT " THE LAST POINT ARE BEING READ TO THE PROGRAM NOW ALONG WITH "
PRINT " THE EQUIVALENT RADIAL INCREMENT. THE CENTER LINE OF YOUR "
PRINT " MEASUREMENTS WILL BE TAKEN AS R = ZERO. "
PRINT

INPUT #3, N
DIM DR(N), P(N)
GLNTH = 0
FOR I = 1 TO N
    INPUT #3, DR(I), P(I)
    GLNTH = GLNTH + DR(I)

```

```

NEXT I
CLOSE #3
:
: set new array dimensions
:
DIM R(N), V(N)
DIM RAD(N), PRES(N), RAD1(N), PRES1(N), RAD2(N), PRES2(N)
DIM VTLD(N), VPRM(N), VTLD1(N), VTLD2(N), VPRM1(N), VPRM2(N)
DIM VEL(N), VEL1(N), VEL2(N)
:
: calculation of raw velocity profile
:
V(0) = 0
LEG = 0
VMAX = 0
GRO = GLNTH / 2
FOR I = 1 TO N
  LEG = LEG + DR(I)
  R(I) = LEG - GRO
  V(I) = SQR((2 * 32.2 * RHOW * P(I)) / (12 * RHOF))
  IF V(I) > VMAX THEN
    VMAX = V(I)
    QMAX = P(I)
  END IF
  WRITE #2, R(I), V(I)
NEXT I
QVMX = VMAX * PI * (DIAM / 12) ^ 2 / 4 * 60
MFMX = RHOF * VMAX ^ 2 * (PI * (DIAM / 12) ^ 2) / 4
CLOSE #2
WRITE #1, PNOZ, QMAX, VMAX
WRITE #1,
:
: print raw velocity table
:
CLS
PRINT
PRINT "          TABLE OF VELOCITY PROFILE DATA"
PRINT
PRINT "          X          V(X)          "
PRINT "          ======"
FOR I = 1 TO N
  PRINT ,
  PRINT USING "####.####"; R(I); TAB(35); V(I)
  IF I = 20 OR I = 44 THEN
    INPUT " HIT ENTER TO CONTINUE"; DUMY
  END IF
NEXT I
PRINT : PRINT : PRINT
INPUT "HIT ENTER TO CONTINUE"; DUMY
:
: GRAPHICS
:
: window correct coordinate system
:
XW1 = -1.1 * GRO
XW2 = 1.1 * GRO
YW1 = -.2 * VMAX
YW2 = 1.2 * VMAX
SCREEN 2
WINDOW (XW1, YW1)-(XW2, YW2)
LINE (XW1, 0)-(XW2, 0)
LINE (0, YW1)-(0, YW2)

```

put in tick marks and values

```

GTOL = .05
XTIC = .01 * (XW2 - XW1)
YTIC = .01 * (YW2 - YW1)
GRAD = .01 * (XW2 - XW1)
COLO = INT((-XW1 / (XW2 - XW1)) * 80)
ROWO = INT((YW2 / (YW2 - YW1)) * 25) + 2
LOCATE ROWO, COLO
PRINT USING "#.#"; 0

XINC = INT(((XW2 - XW1) * 1000)) / 10000
J = (INT((-XW2 - XW1) * 1000 / 2)) / 1000 + XINC
CNT = 0
DO
  IF ABS(J - 0) > GTOL THEN
    LINE (J, 0)-(J, YTIC)
    COL = COLO + (80 * J) / (XW2 - XW1)
    ROW = ROWO
    LOCATE ROW, COL
    PRINT USING "##.##"; J
  END IF
  J = J + (2 * XINC)
LOOP WHILE J < GRO

YINC = INT(1.2 * VMAX / 100) * 10
IF YINC < 10 THEN
  YINC = 10
END IF
FOR J = YINC TO INT(1.2 * VMAX) STEP YINC
  LINE (0, J)-(XTIC, J)
  IF INT(CNT / 2) = CNT / 2 THEN
    COL = COLO + 2
    ROW = (ROWO - (25 * J / (YW2 - YW1))) - 1
    LOCATE ROW, COL
    PRINT USING "####"; J
  END IF
  CNT = CNT + 1
NEXT J
CNT = 0

```

plot points

```

FOR I = 1 TO N
  PSET (R(I), V(I))
  CIRCLE (R(I), V(I)), GRAD, 1
  IF I > 1 THEN
    LINE (R(I), V(I))-(R(I - 1), V(I - 1))
  END IF
NEXT I

```

label screen

```

LOCATE 1, 50
PRINT " VMAX = "; VMAX
LOCATE 25, 50
INPUT "HIT ENTER TO CONTINUE"; DUMY

```

INTEGRATION

eliminate redundant zero points

```

P(0) = 999
IF P(1) = 0 AND P(2) = 0 THEN
  IF P(N) = 0 AND P(N - 1) = 0 THEN
    FOR I = 1 TO N
      P(I) = P(I + 1)
      R(I) = R(I + 1)
    NEXT I
    N = N - 1
  ELSE
    FOR I = 1 TO N
      P(I) = P(I + 1)
      R(I) = R(I + 1)
    NEXT I
    N = N - 1
  END IF
ELSE
  IF P(N) = 0 AND P(N - 1) = 0 THEN
    N = N - 1
  END IF
END IF

```

subroutine to determine R0 from interpolation of half VMAX

```

RSWCH = 0
DRDL1 = 0
DRDL2 = 0
RPOS = 0
FOR I = 1 TO N
  RPOS = RPOS + DR(I)
  IF V(I) > .5 * VMAX AND V(I - 1) < .5 * VMAX THEN
    IF RSWCH = 0 THEN
      X1 = ((.5 * VMAX - V(I - 1)) * DR(I)) / (V(I) - V(I - 1))
      RVMX1 = DR(I) - X1
      RSWCH = 1
      DRDL1 = RPOS
    END IF
  END IF
  IF I < N THEN
    IF V(I) > .5 * VMAX AND V(I + 1) < .5 * VMAX THEN
      X2 = ((.5 * VMAX - V(I + 1)) * DR(I + 1)) / (V(I) - V(I + 1))
      RVMX2 = DR(I + 1) - X2
      DRDL2 = RPOS
    END IF
  END IF
NEXT I
IF DRDL2 = 0 THEN
  DRDL2 = RPOS
END IF
CLNTH = (DRDL2 - DRDL1) + RVMX1 + RVMX2
CENT = (DRDL1 - RVMX1) + (CLNTH / 2)

```

determine velocity profile in radial coordinates (both sides)

```

TOL = .0001
RPOS = 0
RSWCH = 0
CNT1 = 1
CNT2 = 0
FOR I = 1 TO N
  RPOS = RPOS + DR(I)
  IF RPOS > CENT AND ABS(RPOS - CENT) > .0005 THEN

```

```

IF RSWCH = 0 THEN
  IF CENT - (RPOS - DR(I)) <= TOL THEN
    RAD1(1) = 0
    PRES1(1) = P(I - 1)
    RAD(I) = 0
    PRES(I - 1) = P(I - 1)
  ELSE
    RAD1(1) = 0
    PRES1(1) = (P(I) + P(I - 1)) / 2
    RAD(I) = 0
    PRES(I) = PRES1(1)
    CNT2 = I
  END IF
  IOFST = I - 2
  RSWCH = 1
END IF
RAD1(I - IOFST) = RPOS - CENT
PRES1(I - IOFST) = P(I)
CNT1 = CNT1 + 1
ELSE
  RAD(I) = CENT - RPOS
  PRES(I) = P(I)
  CNT2 = CNT2 + 1
END IF
NEXT I

```

get both profiles in same order

```

FOR I = 1 TO CNT2
  RAD2(I) = RAD(CNT2 + 1 - I)
  PRES2(I) = PRES(CNT2 + 1 - I)
  IF I = 1 THEN
    RAD2(I) = 0
  END IF
NEXT I

```

truncate profiles for points greater then the radius

```

I = 1
DO
  IF ABS((DIAM / 2) - RAD1(I)) <= .0005 OR DIAM / 2 <= RAD1(I) THEN
    PRES1(I) = 0
    RAD1(I) = DIAM / 2
    N1 = I
    I = CNT1
  END IF
  I = I + 1
LOOP WHILE I <= CNT1

```

```

I = 1
DO
  IF ABS((DIAM / 2) - RAD2(I)) <= .0005 OR DIAM / 2 <= RAD2(I) THEN
    PRES2(I) = 0
    RAD2(I) = DIAM / 2
    N2 = I
    I = CNT2
  END IF
  I = I + 1
LOOP WHILE I <= CNT2

```

make an odd number of points if there is not

```

IF INT(N1 / 2) = N / 2 THEN
  FOR I = N1 + 1 TO 3 STEP -1
    RAD1(I) = RAD1(I - 1)
    PRES1(I) = PRES1(I - 1)
  NEXT I
  RAD1(2) = RAD1(2) / 2
  PRES1(2) = (PRES1(1) + PRES1(2)) / 2
  N1 = N1 + 1
END IF

IF INT(N2 / 2) = N2 / 2 THEN
  FOR I = N2 + 1 TO 3 STEP -1
    RAD2(I) = RAD2(I - 1)
    PRES2(I) = PRES2(I - 1)
  NEXT I
  RAD2(2) = RAD2(2) / 2
  PRES2(2) = (PRES2(1) + PRES2(2)) / 2
  N2 = N2 + 1
END IF

calculate velocities and integrands

FOR I = 1 TO N1
  VEL1(I) = SQR((2 * 32.2 * RHOW * PRES1(I)) / (12 * RHOF))
  VTLD1(I) = VEL1(I) * RAD1(I) / 12
  VPRM1(I) = VEL1(I) * VEL1(I) * RAD1(I) / 12
NEXT I
FOR I = 1 TO N2
  VEL2(I) = SQR((2 * 32.2 * RHOW * PRES2(I)) / (12 * RHOF))
  VTLD2(I) = VEL2(I) * RAD2(I) / 12
  VPRM2(I) = VEL2(I) * VEL2(I) * RAD2(I) / 12
NEXT I

print the velocity profiles if needed

CLS
PRINT : PRINT
INPUT " WOULD YOU LIKE TO PRINT THE PROFILES? <Y> OR <N>"; SPNC$
IF SPNC$ = "N" THEN
  GOTO 70
END IF

LPRINT : LPRINT
LPRINT " "; SIZE$
LPRINT
LPRINT "      VELOCITY PROFILE                INTEGRATION PROFILE"
LPRINT "      R(in)      V(ft/s)                R(in)      V(ft/s)"
LPRINT " ====="
I = 1
DO
  IF I > N1 + N2 + 1 THEN
    LPRINT "      ";
    LPRINT USING "#.####"; R(I);
    LPRINT "      ";
    LPRINT USING "###.##"; V(I)
  ELSE
    IF I <= N2 THEN
      LPRINT "      ";
      LPRINT USING "#.####"; R(I);
      LPRINT "      ";
      LPRINT USING "###.##"; V(I);
      LPRINT "      ";
    END IF
  END IF
  I = I + 1

```

```

LPRINT USING "#.####"; RAD2(N2 - I + 1);
LPRINT "      ";
LPRINT USING "###.##"; VEL2(N2 - I + 1)
ELSE
  IF I = N2 + 1 THEN
    LPRINT "      ";
    LPRINT USING "#.####"; R(I);
    LPRINT "      ";
    LPRINT USING "###.##"; V(I)
  ELSE
    K = I - N2 - 1
    LPRINT "      ";
    LPRINT USING "#.####"; R(I);
    LPRINT "      ";
    LPRINT USING "###.##"; V(I);
    LPRINT "      ";
    LPRINT USING "#.####"; RAD1(K);
    LPRINT "      ";
    LPRINT USING "###.##"; VEL1(K)
  END IF
END IF
END IF
I = I + 1
LOOP WHILE I <= N
70 PRINT : PRINT
PRINT " WOULD YOU LIKE TO PRINT THE INTEGRATION DATA"
INPUT " AS IT IS MADE AVAILABLE? <Y> OR <N>"; SWCH$
; assign sides to variables for integation
;
RSWCH = 0
QAVE = 0: TOT1 = 0
MFAVE = 0: TOT2 = 0
RAT1A = 0: TOT3 = 0
RAT2A = 0: TOT4 = 0
DE1AV = 0: TOT5 = 0
DE2AV = 0: TOT6 = 0
DE3AV = 0: TOT7 = 0
VE1AV = 0: TOT8 = 0
VE2AV = 0: TOT9 = 0
VE3AV = 0: TOT10 = 0
TATM = TATM + 459
PATM = PATM * 2116.2 / 29.92
;
10 IF RSWCH = 0 THEN
  FOR I = 1 TO N1
    RAD(I) = RAD1(I)
    VEL(I) = VEL1(I)
    VPRM(I) = VPRM1(I)
    VTLD(I) = VTLD1(I)
    WRITE #1, RAD(I), VEL(I)
  NEXT I
  N = N1
  DSID = 1
ELSE
  FOR I = 1 TO N2
    RAD(I) = RAD2(I)
    VEL(I) = VEL2(I)
    VPRM(I) = VPRM2(I)
    VTLD(I) = VTLD2(I)
    WRITE #1, RAD(I), VEL(I)
  NEXT I

```



```

      N = N2
      DSID = 2
    END IF

```

```

integrate for Q and mom flux with Simpson's Rule (modified)

```

```

GRND1 = 0
GRND2 = 0
FOR I = 1 TO N - 2 STEP 2
  DS1 = (RAD(I + 1) - RAD(I)) / 12
  DS2 = (RAD(I + 2) - RAD(I + 1)) / 12
  PRT11 = (VTLD(I + 1) - VTLD(I)) * DS2 ^ 3
  PRT12 = (VTLD(I + 1) - VTLD(I + 2)) * DS1 ^ 3
  PRT13 = (2 * VTLD(I) + 3 * VTLD(I + 1) + VTLD(I + 2)) * DS1 ^ 2 * DS2
  PRT14 = (VTLD(I) + 3 * VTLD(I + 1) + 2 * VTLD(I + 2)) * DS1 * DS2 ^ 2
  GRND1 = GRND1 + (PRT11 + PRT12 + PRT13 + PRT14) / (6 * DS1 * DS2)
  PRT21 = (VPRM(I + 1) - VPRM(I)) * DS2 ^ 3
  PRT22 = (VPRM(I + 1) - VPRM(I + 2)) * DS1 ^ 3
  PRT23 = (2 * VPRM(I) + 3 * VPRM(I + 1) + VPRM(I + 2)) * DS1 ^ 2 * DS2
  PRT24 = (VPRM(I) + 3 * VPRM(I + 1) + 2 * VPRM(I + 2)) * DS1 * DS2 ^ 2
  GRND2 = GRND2 + (PRT21 + PRT22 + PRT23 + PRT24) / (6 * DS1 * DS2)
NEXT I
CLS
PRINT : PRINT
PRINT " RESULTS OF SIMPSONS RULE INTEGRATION TECHNIQUE"
PRINT "      SIDE "; DSID
GOSUB 30
INPUT "HIT ENTER TO CONTINUE"; DUMY

```

```

integrate for Q and mom flux with trapizodial rule

```

```

GRND1 = 0
GRND2 = 0
FOR I = 1 TO N - 1
  PRT1 = ((VTLD(I + 1) + VTLD(I)) / 2)
  GRND1 = GRND1 + ((RAD(I + 1) - RAD(I)) / 12) * PRT1
  PRT2 = ((VPRM(I + 1) + VPRM(I)) / 2)
  GRND2 = GRND2 + ((RAD(I + 1) - RAD(I)) / 12) * PRT2
NEXT I
CLS
PRINT : PRINT
PRINT " RESULTS OF TRAPIZODIAL INTEGRATION TECHNIQUE"
PRINT "      SIDE "; DSID
GOSUB 30
INPUT "HIT ENTER TO CONTINUE"; DUMY

```

```

print results if so requested earlier

```

```

IF SWCH$ = "Y" THEN
  LPRINT
  LPRINT "      SIDE "; DSID
  LPRINT " RESULTS OF SIMPSON'S RULE          RESULTS OF TRAPAZODIAL RULE"
  LPRINT " "; QAVE - QNOZ - TOT1; MFAVE - MFNOZ - TOT2;
  LPRINT " "; QNOZ; MFNOZ
  LPRINT " "; RAT1A - RAT1 - TOT9; RAT2A - RAT2 - TOT10;
  LPRINT " "; RAT1; RAT2
  LPRINT " "; (DE1AV - DEFF1 - TOT3) * 12; VE1AV - VEFF1 - TOT4;
  LPRINT " "; DEFF1 * 12; VEFF1
  LPRINT " "; (DE2AV - DEFF2 - TOT5) * 12; VE2AV - VEFF2 - TOT6;
  LPRINT " "; DEFF2 * 12; VEFF2
  LPRINT " "; (DE3AV - DEFF3 - TOT7) * 12; VE3AV - VEFF3 - TOT8;
  LPRINT " "; DEFF3 * 12; VEFF3

```

```

TOT1 = QAVE
TOT2 = MFAVE
TOT9 = RAT1A
TOT10 = RAT2A
TOT3 = DE1AV
TOT4 = VE1AV
TOT5 = DE2AV
TOT6 = VE2AV
TOT7 = DE3AV
TOT8 = VE3AV
END IF
IF RSWCH = 1 AND SPNC$ = "Y" THEN
  LPRINT CHR$(12)
END IF

```

```

switch to do routine twice; once for each half

```

```

IF RSWCH = 0 THEN
  WRITE #1,
  RSWCH = 1
  GOTO 10
END IF

```

```

calculate averages and write to data file

```

```

QAVE = QAVE / 4
VAVE = QAVE / (60 * PI * (DIAM / 12) ^ 2 / 4)
MFAVE = MFAVE / 4
RAT1A = RAT1A / 4
RAT2A = RAT2A / 4
DE1AV = DE1AV / 4
DE2AV = DE2AV / 4
DE3AV = DE3AV / 4
VE1AV = VE1AV / 4
VE2AV = VE2AV / 4
VE3AV = VE3AV / 4
RAT3 = SQR(QMAX / PNOZ)
WRITE #1,
WRITE #1, QAVE, MFAVE, VAVE
WRITE #1, RAT1A, RAT2A, RAT3
WRITE #1, DE2AV * 12, VE2AV
WRITE #1, DE3AV * 12, VE3AV

```

```

end or rerun program

```

```

CLOSE #1
SCREEN 0
5 CLS
PRINT : PRINT
PRINT : PRINT
PRINT " MAKE A SELECTION:"
PRINT " 1. CALIBRATE ANOTHER NOZZLE"
PRINT " 2. REVIEW RESULTS"
PRINT " 3. END PROGRAM"
PRINT : PRINT
INPUT " CHOOSE FROM <1>, <2>, <3>"; CHOS
IF CHOS = 1 THEN
  RESET
  RUN 20
ELSE
  IF CHOS = 3 THEN

```

```

        GOTO 40
    ELSE
        GOSUB 50
    END IF
END IF
GOTO 5
40 END
,
30
,
SUBROUTINE
,
calculate the values with integrands
,
QNOZ = 2 * PI * GRND1 * 60
MFNOZ = 2 * PI * RHOF * GRND2
RAT1 = QNOZ / QVMX
RAT2 = MFNOZ / MFMX
,
calculate effective diameter
,
MDOT = QNOZ * RHOF / 60
QMAXP = RHOW * 32.2 * QMAX / 12
AEFF1 = MFNOZ / (2 * QMAXP)
DEFF1 = SQR(4 * AEFF1 / PI)
VEFF1 = QNOZ / (AEFF1 * 60)
PRT1 = 2 * RCNST * TATM * QMAXP
PRT2 = PATM + ((GAMMA - 1) / GAMMA) * QMAXP
MF2 = MDOT * SQR(PRT1 / PRT2)
AEFF2 = MF2 / (2 * QMAXP)
DEFF2 = SQR(4 * AEFF2 / PI)
VEFF2 = QNOZ / (AEFF2 * 60)
PRT3 = (MFNOZ / (RHOF * (QNOZ / 60))) ^ 2
PRT4 = PATM * PRT3
PRT5 = (2 * RCNST * TATM) - ((GAMMA - 1) / GAMMA) * PRT3
QEFF3 = PRT4 / PRT5
AEFF3 = MFNOZ / (2 * QEFF3)
DEFF3 = SQR(4 * AEFF3 / PI)
VEFF3 = QNOZ / (AEFF3 * 60)
,
calculate totals for averages
,
QAVE = QAVE + QNOZ
MFAVE = MFAVE + MFNOZ
RAT1A = RAT1A + RAT1
RAT2A = RAT2A + RAT2
DE1AV = DE1AV + DEFF1
DE2AV = DE2AV + DEFF2
DE3AV = DE3AV + DEFF3
VE1AV = VE1AV + VEFF1
VE2AV = VE2AV + VEFF2
VE3AV = VE3AV + VEFF3
,
print results to screen and printer; write data files
,
PRINT : PRINT
PRINT "    VOLUME FLOW = "; QNOZ; " CFM"
PRINT
PRINT "  MOMENTUM FLUX = "; MFNOZ; " LBF"
PRINT
PRINT "    Q MAX RATIO   = "; RAT1
PRINT

```

```

PRINT " MF MAX RATIO = "; RAT2
PRINT : PRINT
WRITE #1,
WRITE #1, QNOZ, MFNOZ
WRITE #1, RAT1, RAT2
WRITE #1, DEFF1 * 12, VEFF1
WRITE #1, DEFF2 * 12, VEFF2
WRITE #1, DEFF3 * 12, VEFF3
80 RETURN
50
SUBROUTINE
print averages to screen and printer

DE2AV = DE2AV * 12
DE3AV = DE3AV * 12
CLS
PRINT : PRINT
PRINT " RESULTS: "; SIZE$
PRINT
PRINT " NOZZLE PRESSURE = "; PNOZ
PRINT " MAXIMUM q READING = "; QMAX
PRINT " MAXIMUM VELOCITY = "; VMAX
PRINT
PRINT " THE AVERAGE VOLUME FLOW CALCULATED = "; QAVE
PRINT " THE AVERAGE MOMENTUM FLUX CALCULATED = "; MFAVE
PRINT " THE AVERAGE VELOCITY OF THE NOZZLE = "; VAVE
PRINT
PRINT "
METHOD 1          METHOD 2"
PRINT "
=====          ====="
PRINT " AVERAGE EFFECTIVE VELOCITY = "; VE2AV; "      "; VE3AV
PRINT " AVERAGE EFFECTIVE DIAMETER = "; DE2AV; "      "; DE3AV
PRINT
PRINT " QNOZ / QVMAX = "; RAT1A
PRINT " MFNOZ / MFVMAX = "; RAT2A
PRINT : PRINT
INPUT " HIT ENTER TO CONTINUE"; DUMY
CLS
PRINT : PRINT
INPUT " WOULD YOU LIKE THESE RESULTS PRINTED? <Y> OR <N>"; SPNC$
IF SPNC$ = "N" THEN
GOTO 60
END IF
LPRINT : LPRINT
LPRINT " RESULTS: "; SIZE$
LPRINT
LPRINT " NOZZLE PRESSURE = "; PNOZ
LPRINT " MAXIMUM q READING = "; QMAX
LPRINT " MAXIMUM VELOCITY = "; VMAX
LPRINT
LPRINT " THE AVERAGE VOLUME FLOW CALCULATED = "; QAVE
LPRINT " THE AVERAGE MOMENTUM FLUX CALCULATED = "; MFAVE
LPRINT " THE AVERAGE VELOCITY OF THE NOZZLE = "; VAVE
LPRINT
LPRINT "
METHOD 1          METHOD 2"
LPRINT "
=====          ====="
LPRINT " AVERAGE EFFECTIVE VELOCITY = "; VE2AV; "      "; VE3AV
LPRINT " AVERAGE EFFECTIVE DIAMETER = "; DE2AV; "      "; DE3AV
LPRINT

```

```
LPRINT " QNOZ / QVMAX = "; RAT1A
LPRINT " MFNOZ / MFVMAX = "; RAT2A
LPRINT : LPRINT
LPRINT CHR$(12)
60 RETURN
```

Sample Input File

HALF INCH STANDARD; 2D NOZ, 0.5, 20.33, 81, 29.21

25	
0	0
0.005	0.6
0.005	5.38
0.005	12.29
0.005	16.82
0.005	18.66
0.005	19.31
0.005	19.43
0.005	19.41
0.05	19.31
0.05	19.39
0.05	19.44
0.05	19.47
0.025	19.47
0.025	19.39
0.05	19.41
0.05	19.32
0.05	19.2
0.05	19.29
0.015	18.75
0.005	17.25
0.005	12.8
0.005	5.17
0.005	0.7
0.005	0

Sample Output: Velocity Profiles and Results of Integration

HALF INCH STANDARD; 2D NOZ

VELOCITY PROFILE		INTEGRATION PROFILE	
R(in)	V(ft/s)	R(in)	V(ft/s)
-.2650	0.00	0.2500	0.00
-.2600	52.93	0.2449	280.26
-.2550	158.50	0.2399	295.19
-.2500	239.56	0.2349	300.29
-.2450	280.26	0.2299	301.22
-.2400	295.19	0.2249	301.06
-.2350	300.29	0.1749	300.29
-.2300	301.22	0.1249	300.91
-.2250	301.06	0.0749	301.30
-.1750	300.29	0.0249	301.53
-.1250	300.91	0.0000	301.53
-.0750	301.30		
-.0250	301.53	0.0000	301.53
-.0000	301.53	0.0251	300.91
0.0250	300.91	0.0751	301.06
0.0750	301.06	0.1251	300.36
0.1250	300.36	0.1751	299.43
0.1750	299.43	0.2251	300.13
0.2250	300.13	0.2401	295.90
0.2400	295.90	0.2451	283.82
0.2450	283.82	0.2500	0.00
0.2500	244.48		
0.2550	155.38		
0.2600	57.17		
0.2650	0.00		

SIDE 1

RESULTS OF SIMPSON'S RULE

24.20133	.2695859
.9810534	.9753441
.4937975	303.2935
.4935203	303.6344
.4932355	303.9851

RESULTS OF TRAPAZODIAL RULE

23.99006	.2666984
.9724888	.9648974
.4911459	303.9008
.4913614	303.6344
.491583	303.3607

SIDE 2

RESULTS OF SIMPSON'S RULE

24.17197	.2691044
.9798635	.9736019
.4933563	303.4677
.493221	303.6344
.4930817	303.8058

RESULTS OF TRAPAZODIAL RULE

24.02717	.267686
.9739935	.9684703
.4920544	303.2481
.4917414	303.6344
.4914197	304.032

Sample Output: Results and Averages

RESULTS: HALF INCH STANDARD; 2D NOZ

NOZZLE PRESSURE = 20.33
 MAXIMUM q READING = 19.47
 MAXIMUM VELOCITY = 301.5285

THE AVERAGE VOLUME FLOW CALCULATED = 24.09763
 THE AVERAGE MOMENTUM FLUX CALCULATED = .2682687
 THE AVERAGE VELOCITY OF THE NOZZLE = 294.548

	METHOD 1	METHOD 2
	-----	-----
AVERAGE EFFECTIVE VELOCITY =	303.6344	303.7959
AVERAGE EFFECTIVE DIAMETER =	.492461	.49233
QNOZ / QVMAX =	.9768498	
MFNOZ / MFVMAX =	.9705784	

APPENDIX E: LV Data Plotted in Linear Coordinates

This appendix contains all of the mean velocity component data plotted in linear coordinates. The mean velocity data presented in figure 5.37 in vector grid form have been plotted in conventional graphs of velocity component versus z/D_{eff} at different x/D_{eff} . The mean velocity data presented in figure 5.38 in vector grid form have been plotted in conventional graphs of velocity component versus y/D_{eff} at different z/D_{eff} .

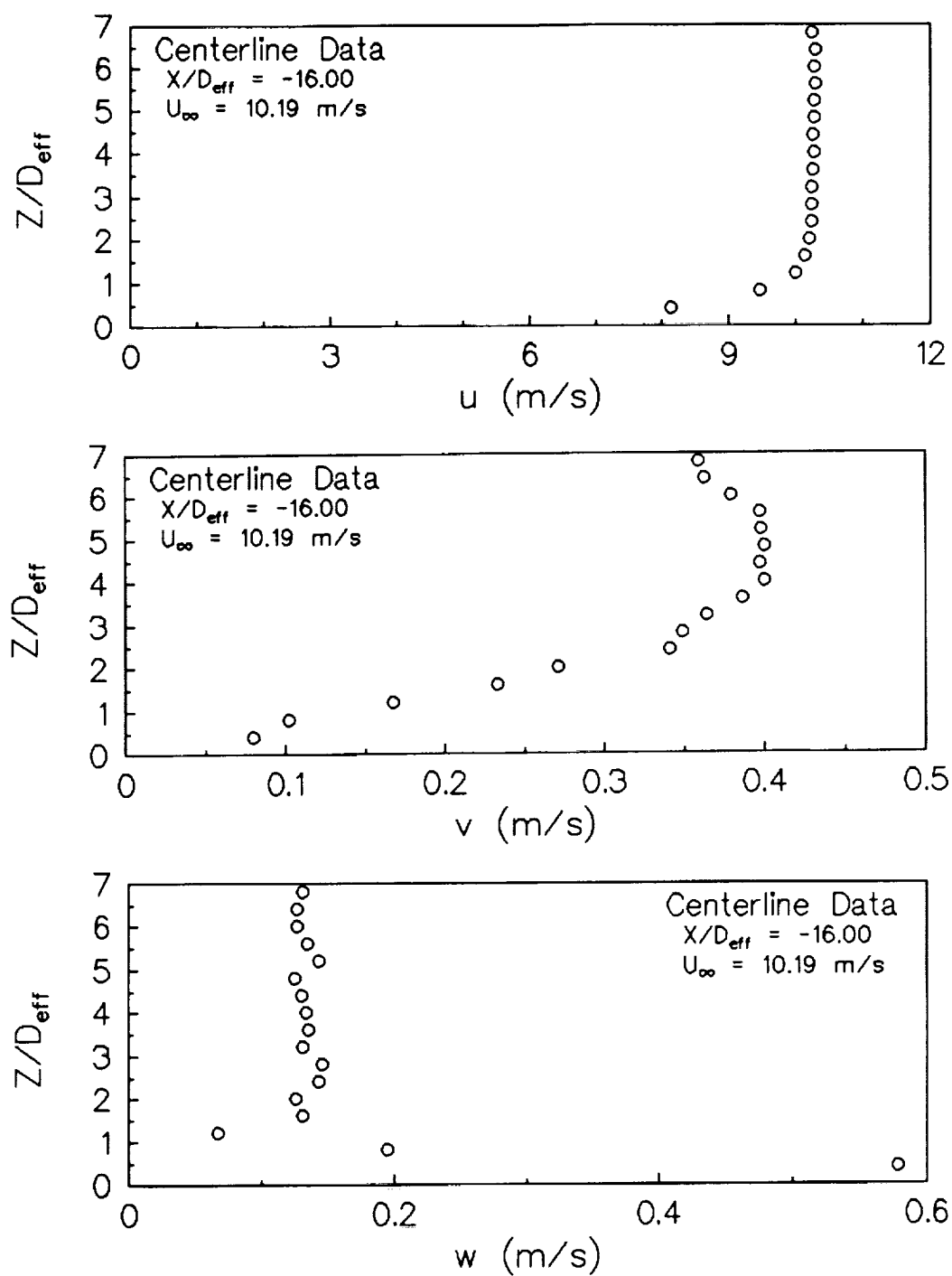


Figure E.1: Three mean velocity components from the LV data for the vertical traverse of the ground vortex centerline; $y/D_{eff} = 0$, $x/D_{eff} = -16.00$

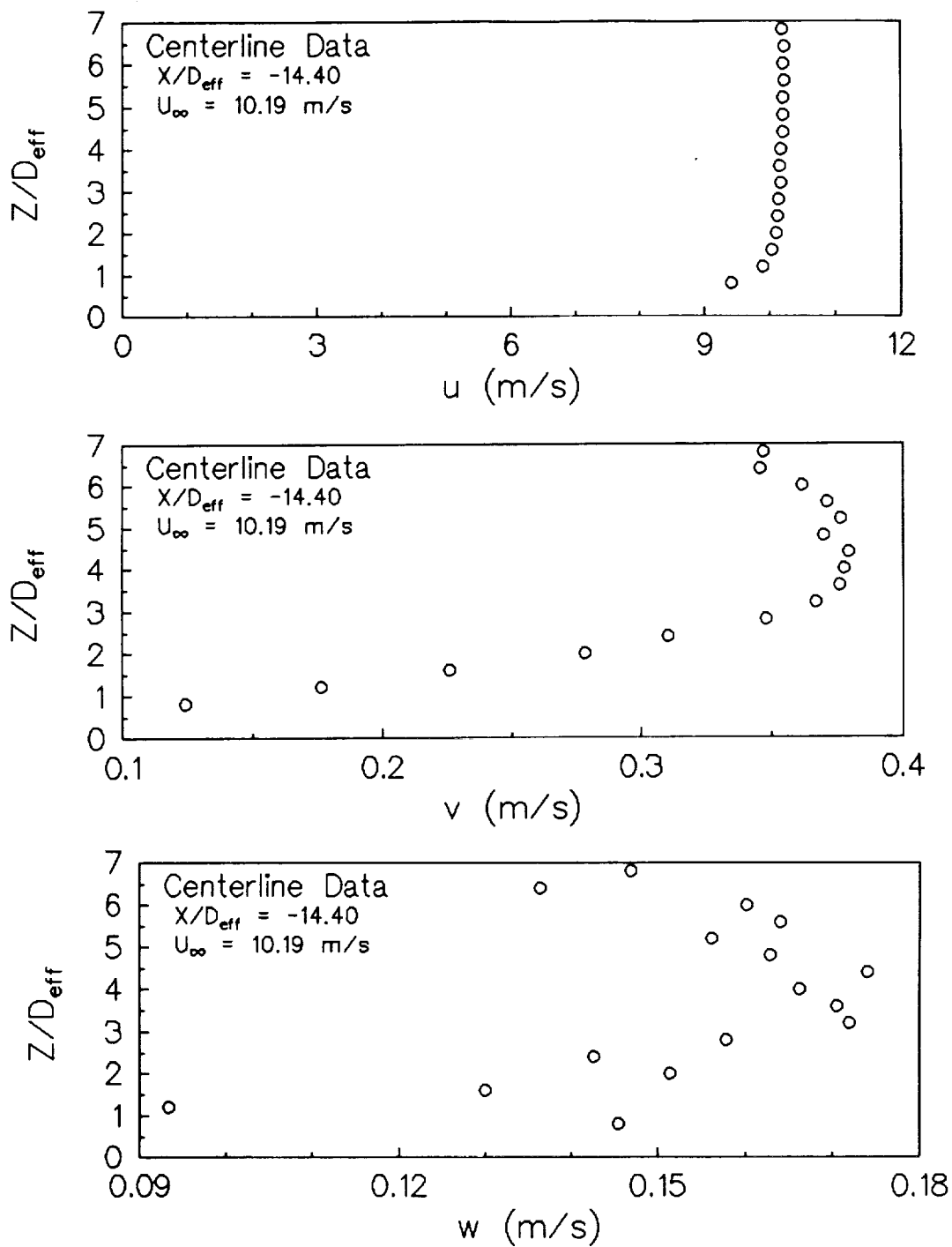


Figure E.2: Three mean velocity components from the LV data for the vertical traverse of the ground vortex centerline; $y/D_{\text{eff}} = 0$, $x/D_{\text{eff}} = -14.40$

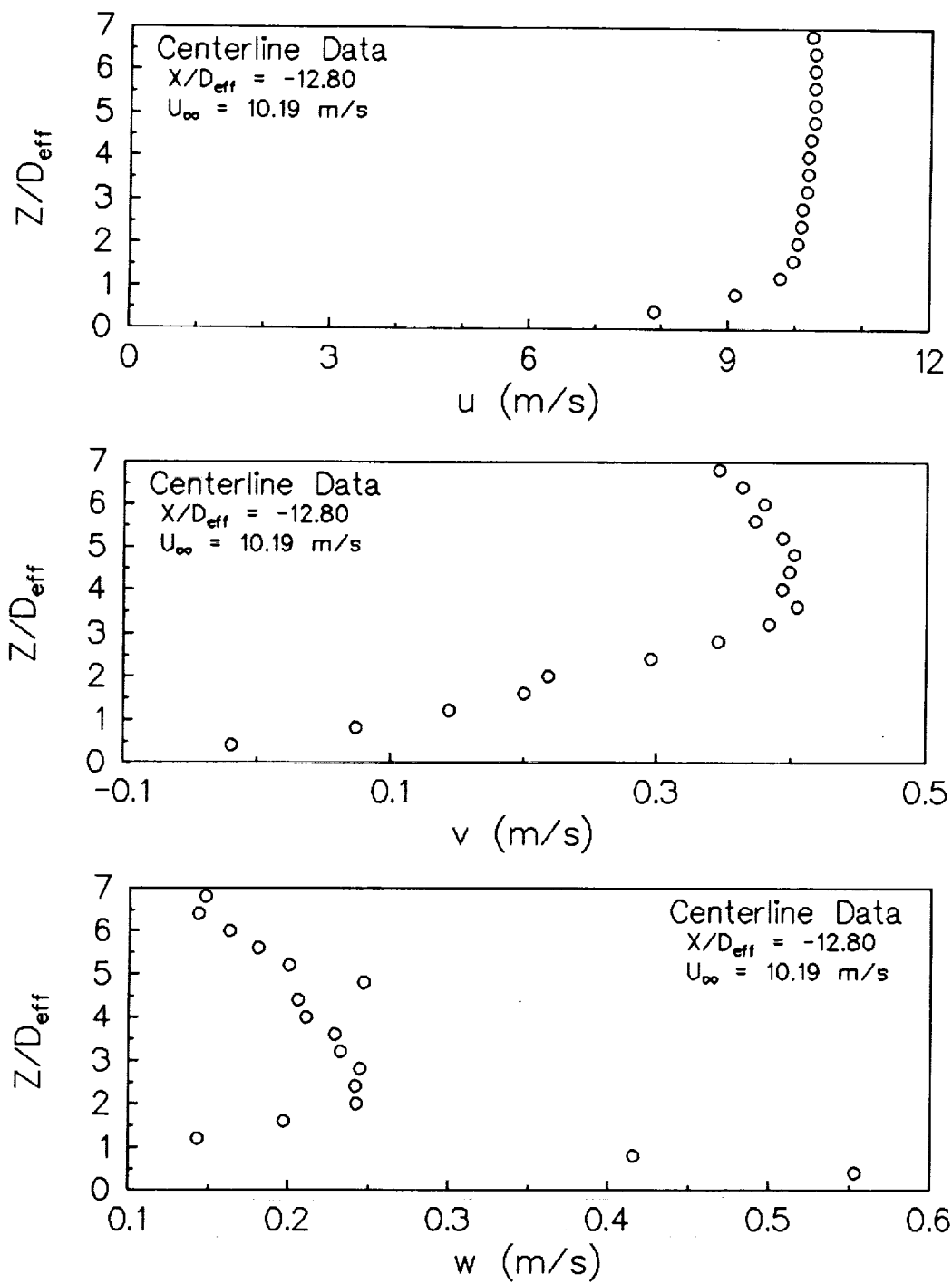


Figure E.3: Three mean velocity components from the LV data for the vertical traverse of the ground vortex centerline; $y/D_{\text{eff}} = 0$, $x/D_{\text{eff}} = -12.80$

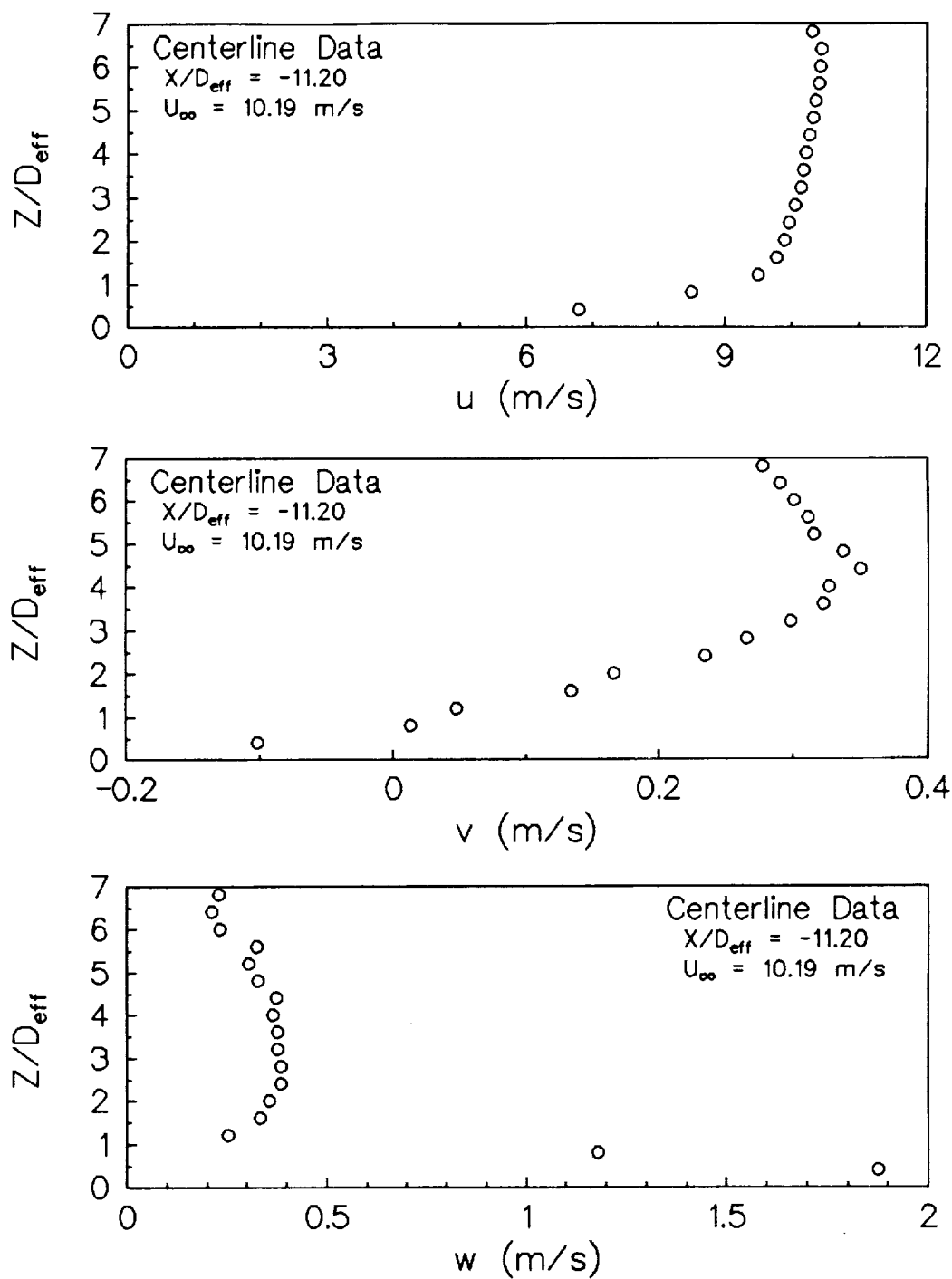


Figure E.4: Three mean velocity components from the LV data for the vertical traverse of the ground vortex centerline; $y/D_{eff} = 0$, $x/D_{eff} = -11.20$

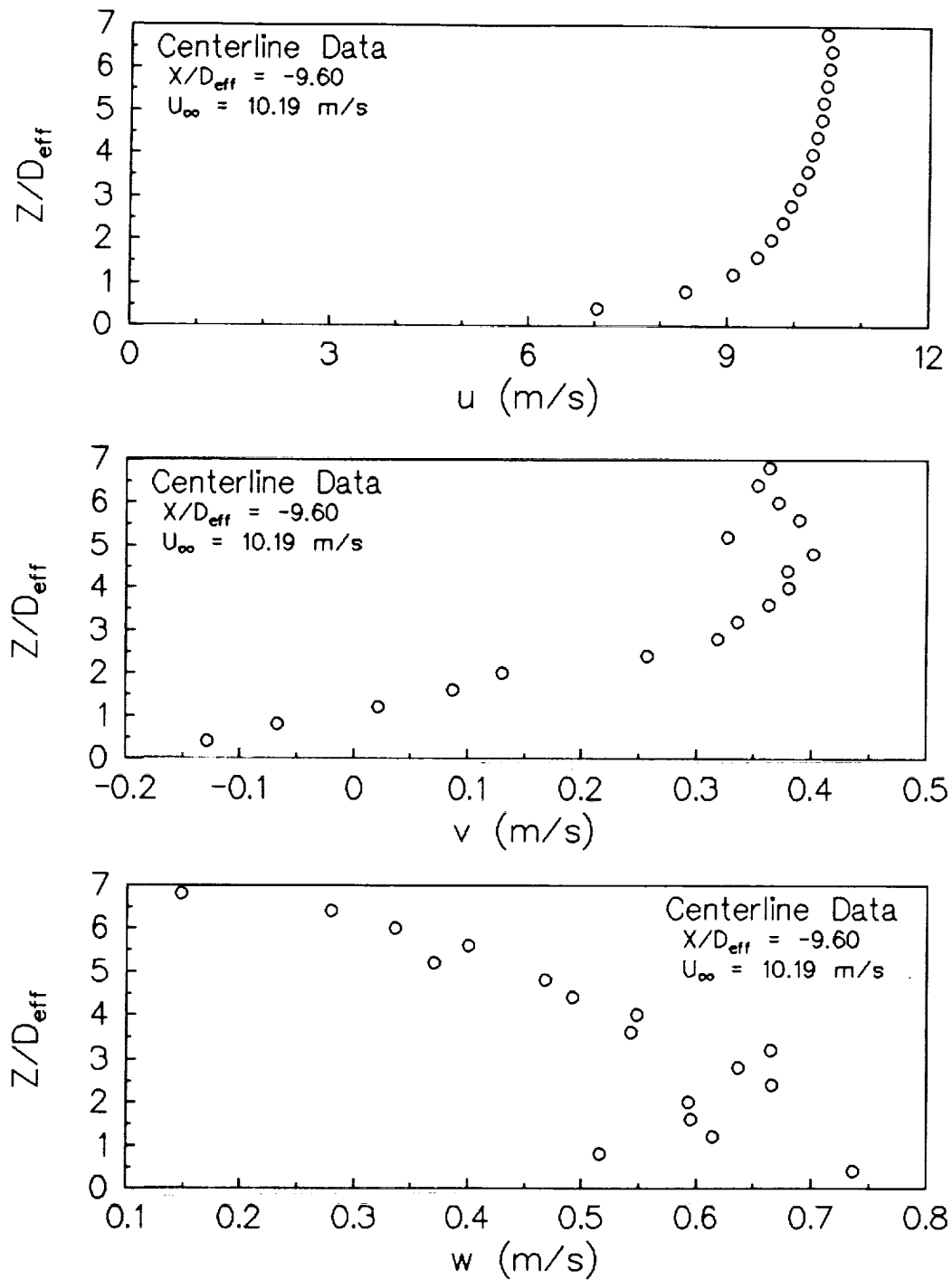


Figure E.5: Three mean velocity components from the LV data for the vertical traverse of the ground vortex centerline; $y/D_{\text{eff}} = 0$, $x/D_{\text{eff}} = -9.60$

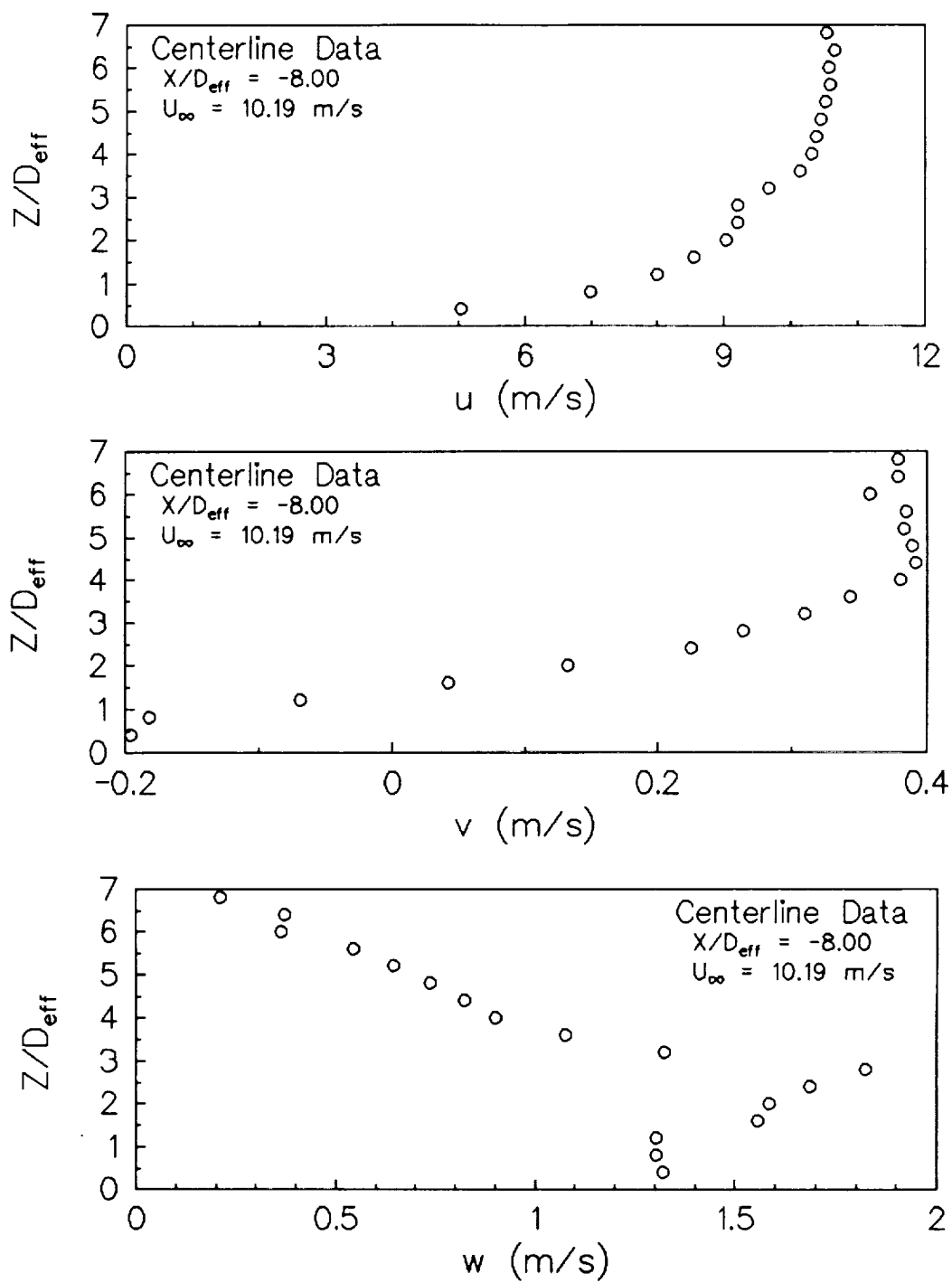
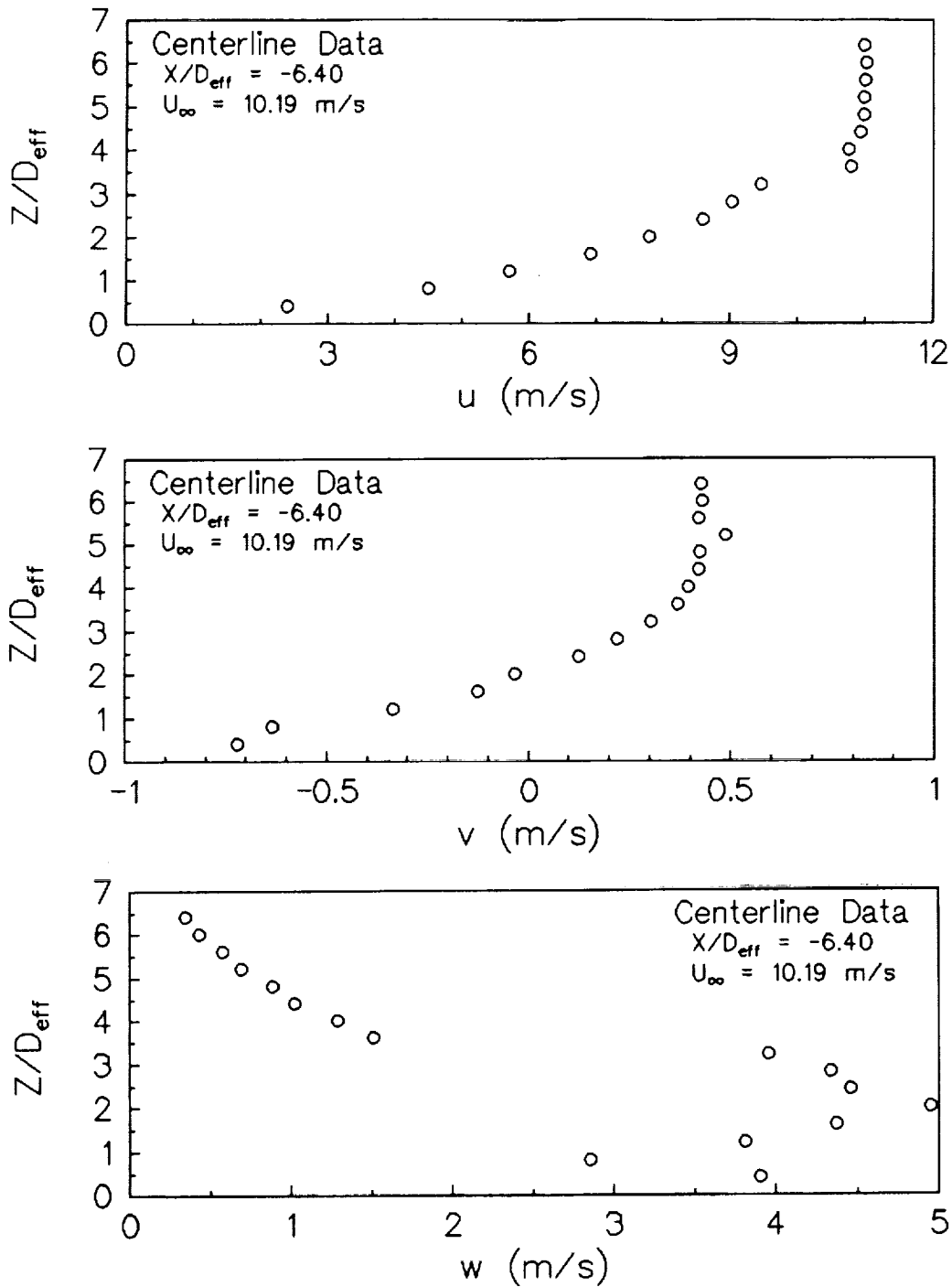


Figure E.6: Three mean velocity components from the LV data for the vertical traverse of the ground vortex centerline; $y/D_{\text{eff}} = 0$, $x/D_{\text{eff}} = -8.00$



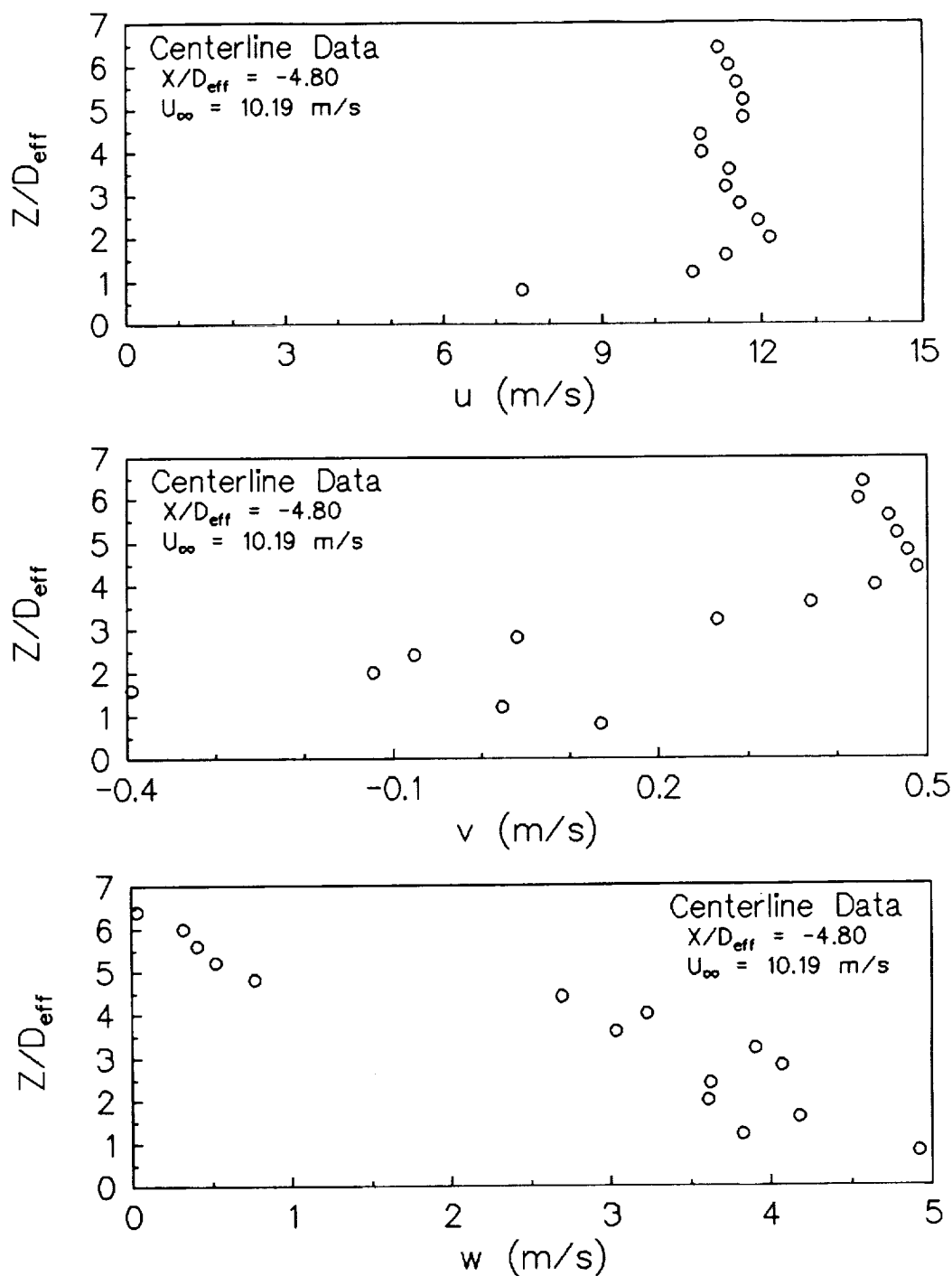
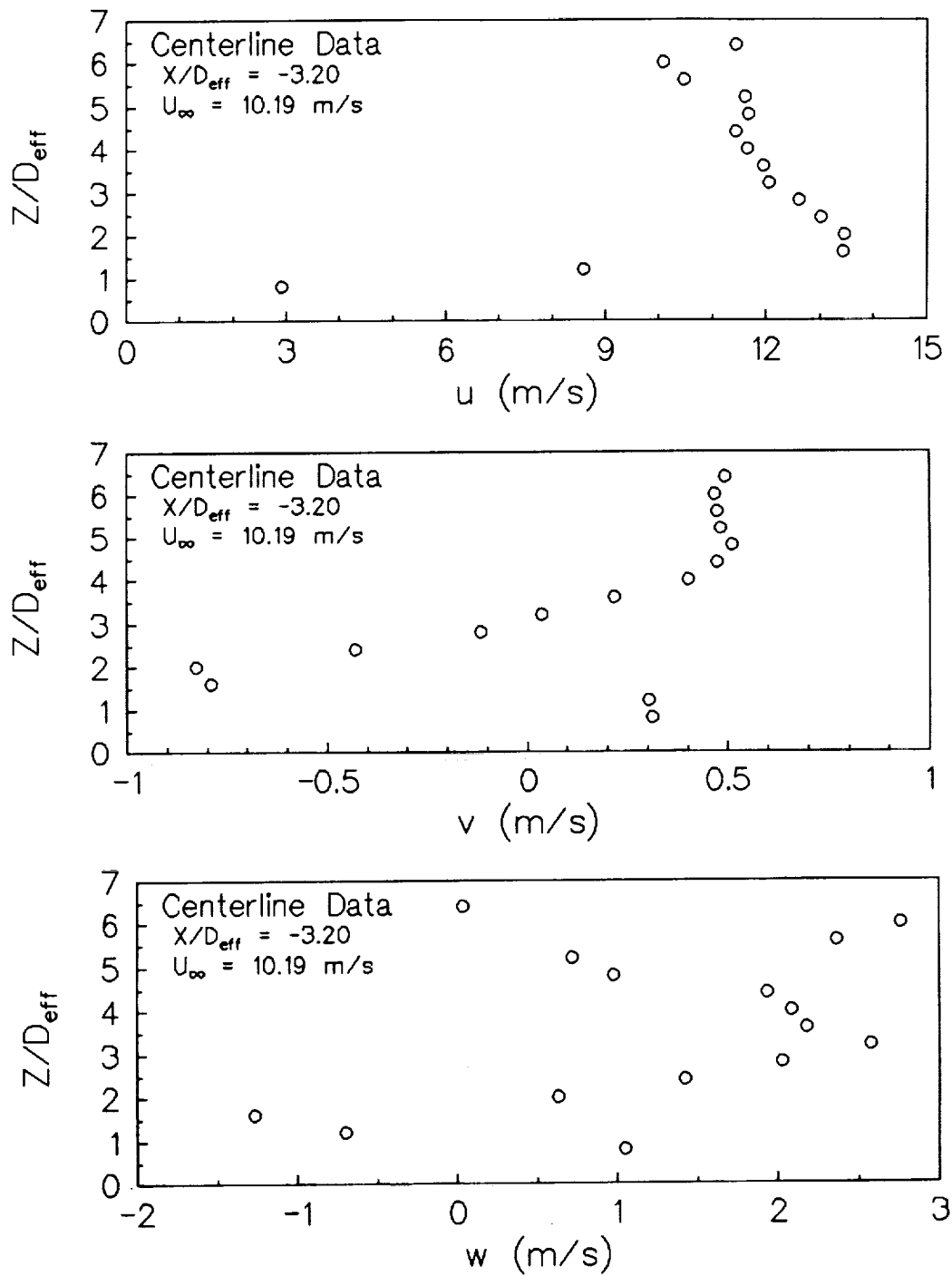


Figure E.8: Three mean velocity components from the LV data for the vertical traverse of the ground vortex centerline; $y/D_{eff} = 0$, $x/D_{eff} = -4.80$



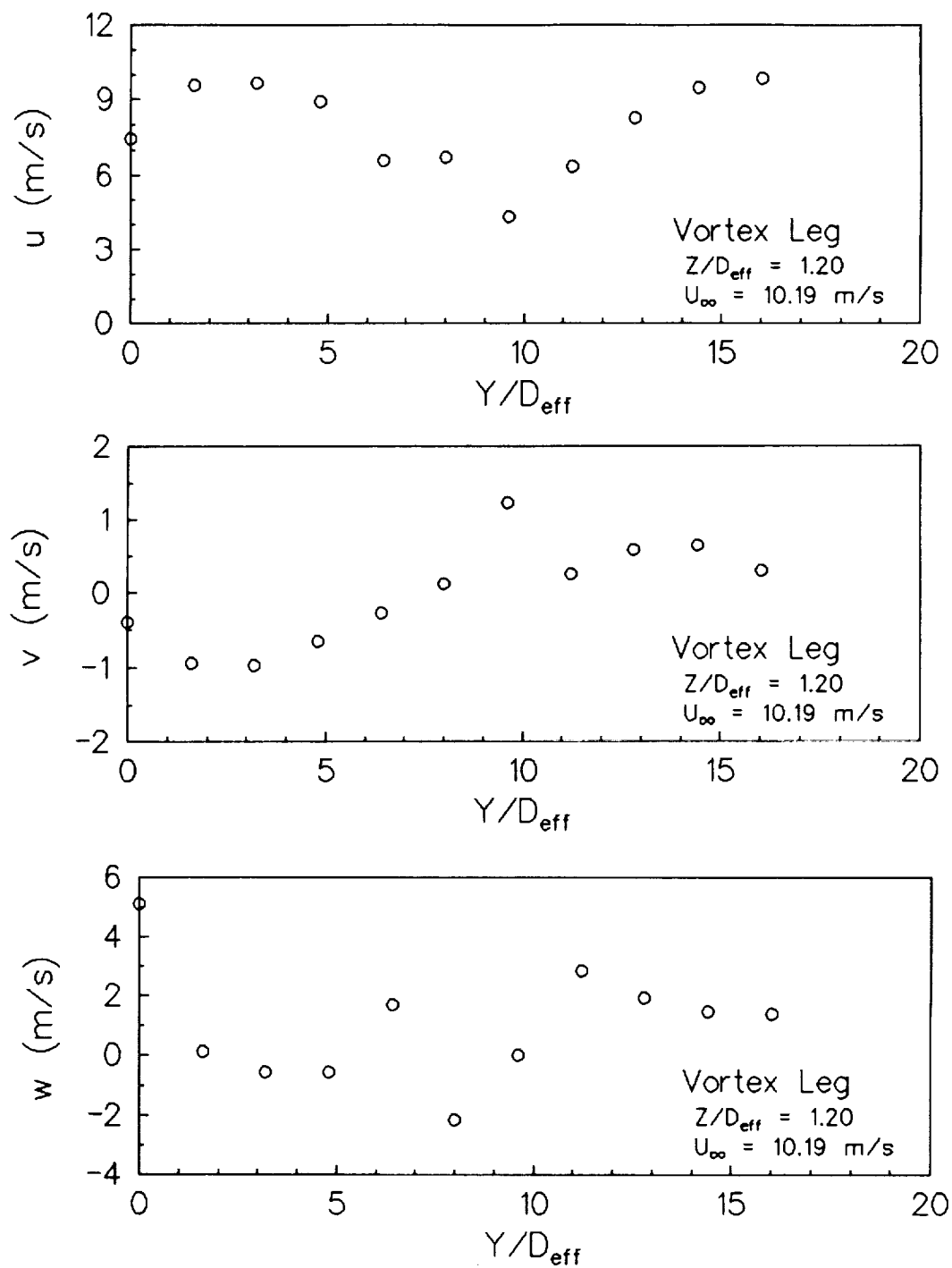


Figure E.10: Three mean velocity components from the LV data for the lateral traverse of the ground vortex leg; $x/D_{eff} = 8.00$, $z/D_{eff} = 1.20$.

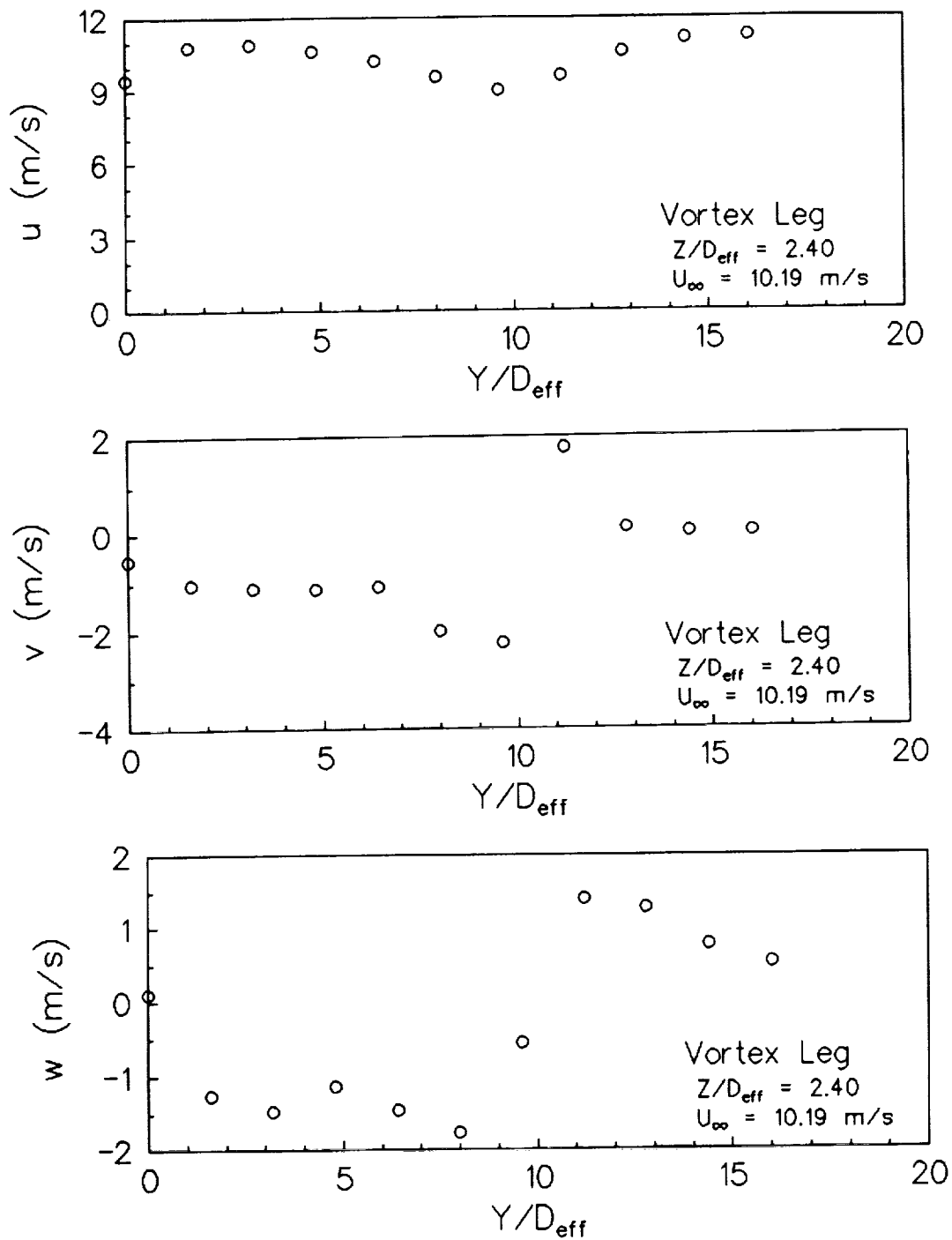


Figure E.11: Three mean velocity components from the LV data for the lateral traverse of the ground vortex leg; $x/D_{eff} = 8.00$, $z/D_{eff} = 2.40$.

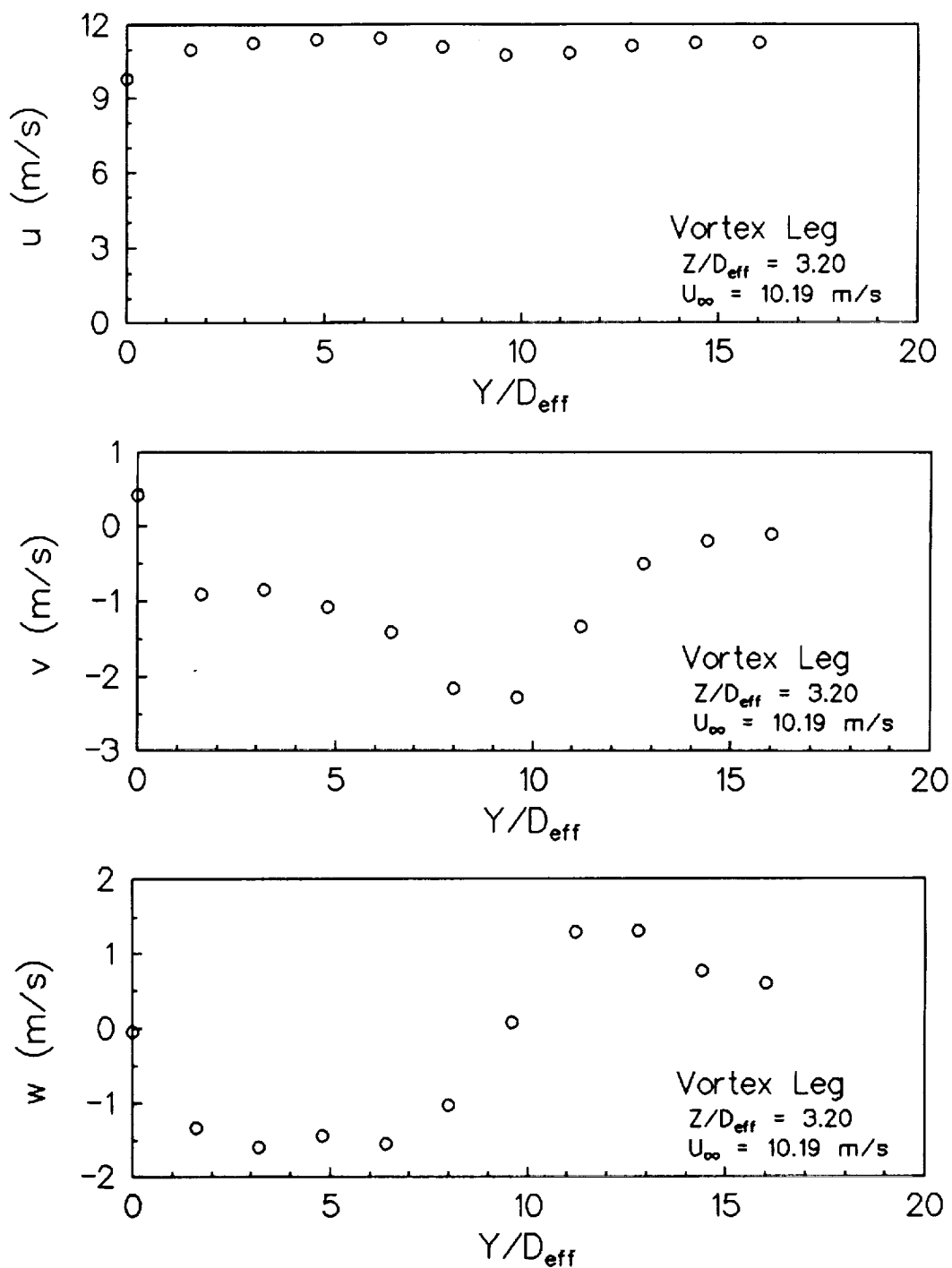


Figure E.12: Three mean velocity components from the LV data for the lateral traverse of the ground vortex leg; $x/D_{eff} = 8.00$, $z/D_{eff} = 3.20$.

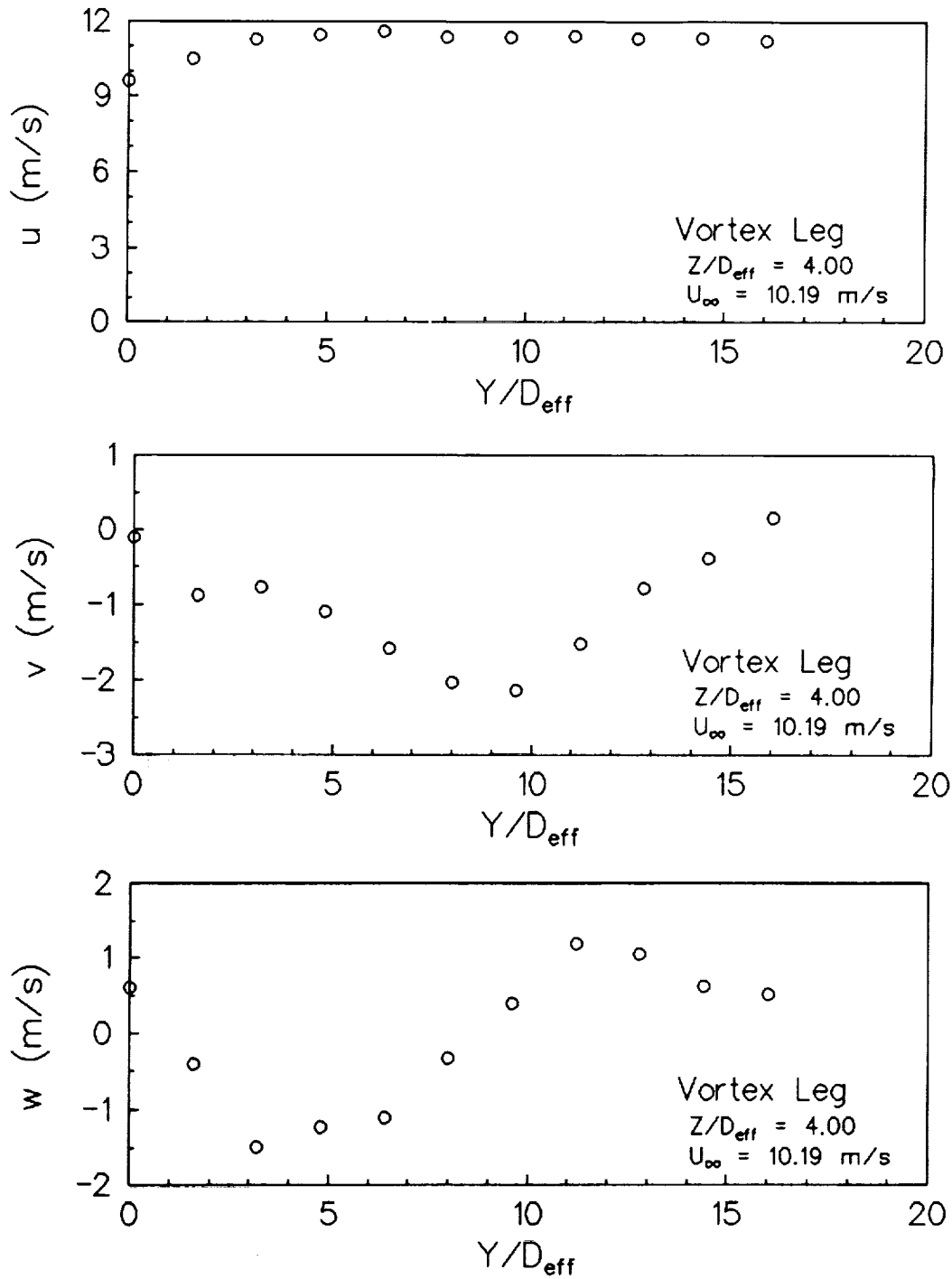
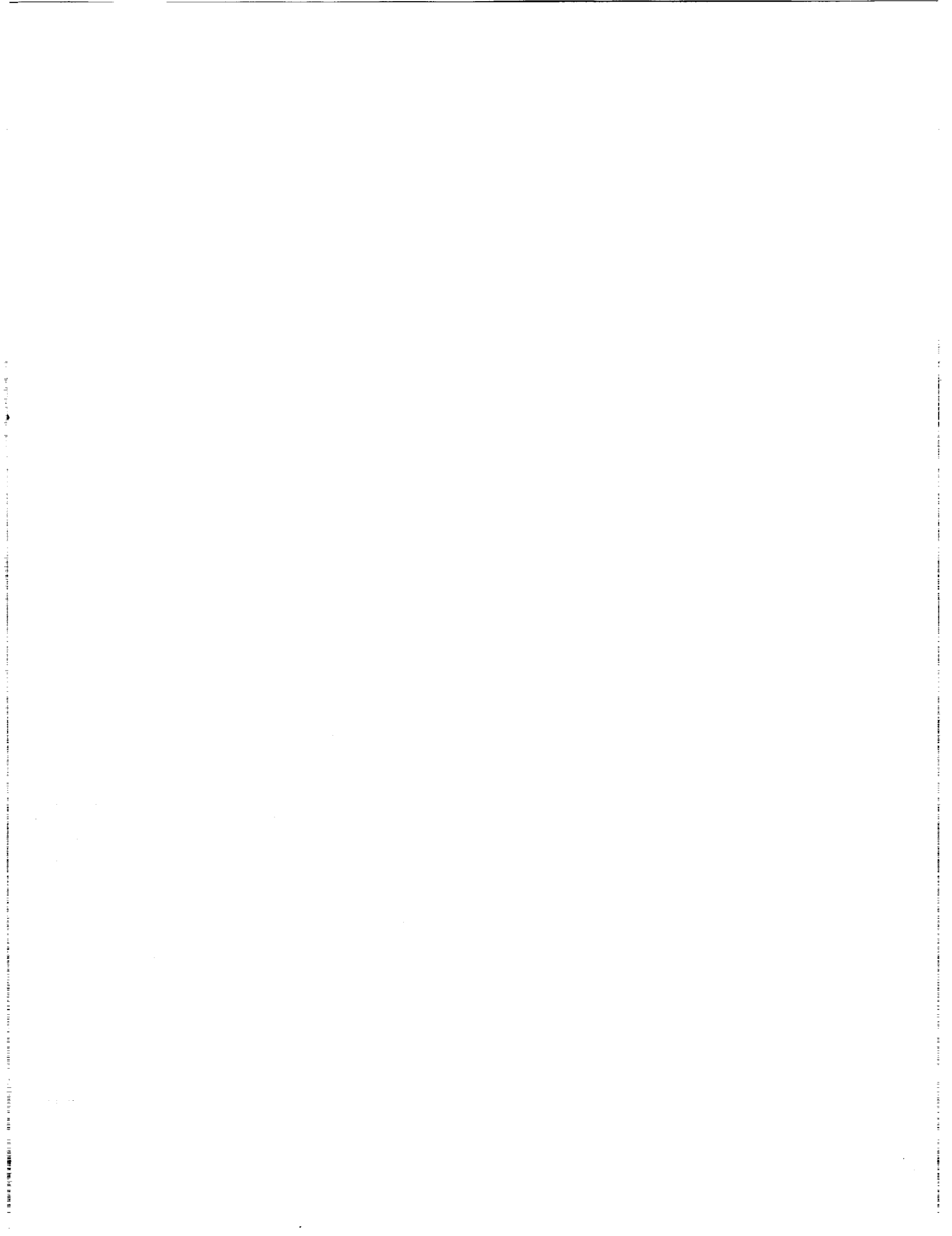


Figure E.13: Three mean velocity components from the LV data for the lateral traverse of the ground vortex leg; $x/D_{eff} = 8.00$, $z/D_{eff} = 4.00$.



...the ... of ...
...the ... of ...
...the ... of ...

REPORT DOCUMENTATION PAGE			Form Approved OMB No. 0704-0188	
Public reporting burden for this collection of information is estimated to average 1 hour per response, including the time for reviewing instructions, searching existing data sources, gathering and maintaining the data needed, and completing and reviewing the collection of information. Send comments regarding this burden estimate or any other aspect of this collection of information, including suggestions for reducing this burden, to Washington Headquarters Services, Directorate for Information Operations and Reports, 1215 Jefferson Davis Highway, Suite 1204, Arlington, VA 22202-4302, and to the Office of Management and Budget, Paperwork Reduction Project (0704-0188), Washington, DC 20503.				
1. AGENCY USE ONLY (Leave blank)	2. REPORT DATE May 1993	3. REPORT TYPE AND DATES COVERED Contractor Report		
4. TITLE AND SUBTITLE The Ground Vortex Flow Field Associated With a Jet in a Cross Flow Impinging on a Ground Plane for Uniform and Annular Turbulent Axisymmetric Jets		5. FUNDING NUMBERS G NAG1-1245 WU 505-59-30-02		
6. AUTHOR(S) William M. Cavage and John M. Kuhlman		8. PERFORMING ORGANIZATION REPORT NUMBER		
7. PERFORMING ORGANIZATION NAME(S) AND ADDRESS(ES) West Virginia University Department of Mechanical and Aerospace Engineering Morgantown, WV 26506-6101		10. SPONSORING / MONITORING AGENCY REPORT NUMBER NASA CR-4513		
9. SPONSORING / MONITORING AGENCY NAME(S) AND ADDRESS(ES) National Aeronautics and Space Administration Langley Research Center Hampton, VA 23681-0001		11. SUPPLEMENTARY NOTES Langley Technical Monitors: Guy T. Kemmerly and John W. Paulson, Jr.		
12a. DISTRIBUTION / AVAILABILITY STATEMENT Unclassified - Unlimited Subject Category 02		12b. DISTRIBUTION CODE		
13. ABSTRACT (Maximum 200 words) An experimental study has been conducted of the impingement of a single circular jet on a ground plane in a cross flow. The geometry is a simplified model of the interaction of propulsive jet exhaust from a V/STOL aircraft with the ground in forward flight. Jets have been oriented normal to the cross flow and ground plane. Jet size, cross flow-to-jet velocity ratio, ground plane-to-jet board spacing, and jet exit turbulence level and mean velocity profile shape have all been varied to determine their effects on the size of the ground vortex interaction region which forms on the ground plane, using smoke injection into the jet. Variation of observed ground vortex size with cross flow-to-jet velocity ratio was consistent with previous studies. Observed effects of jet size and ground plane-to-jet board spacing were relatively small. Jet exit turbulence level effects were also small. However, an annular jet with a low velocity central core was found to have a significantly smaller ground vortex than an equivalent uniform jet at the same values of cross flow-to-jet velocity ratio and jet exit-to-ground plane spacing. This may suggest a means of altering ground vortex behavior somewhat, and point out the importance of proper simulation of jet exit velocity conditions. LV data indicated unsteady turbulence levels in the ground vortex in excess of 70 percent				
14. SUBJECT TERMS Ground Vortex Formation V/STOL Aerodynamics Uniform and Annular Impinging Jets Laser Velocimetry (LV)		15. NUMBER OF PAGES 164		16. PRICE CODE A08
17. SECURITY CLASSIFICATION OF REPORT Unclassified	18. SECURITY CLASSIFICATION OF THIS PAGE Unclassified	19. SECURITY CLASSIFICATION OF ABSTRACT		20. LIMITATION OF ABSTRACT